

AD-A033 229

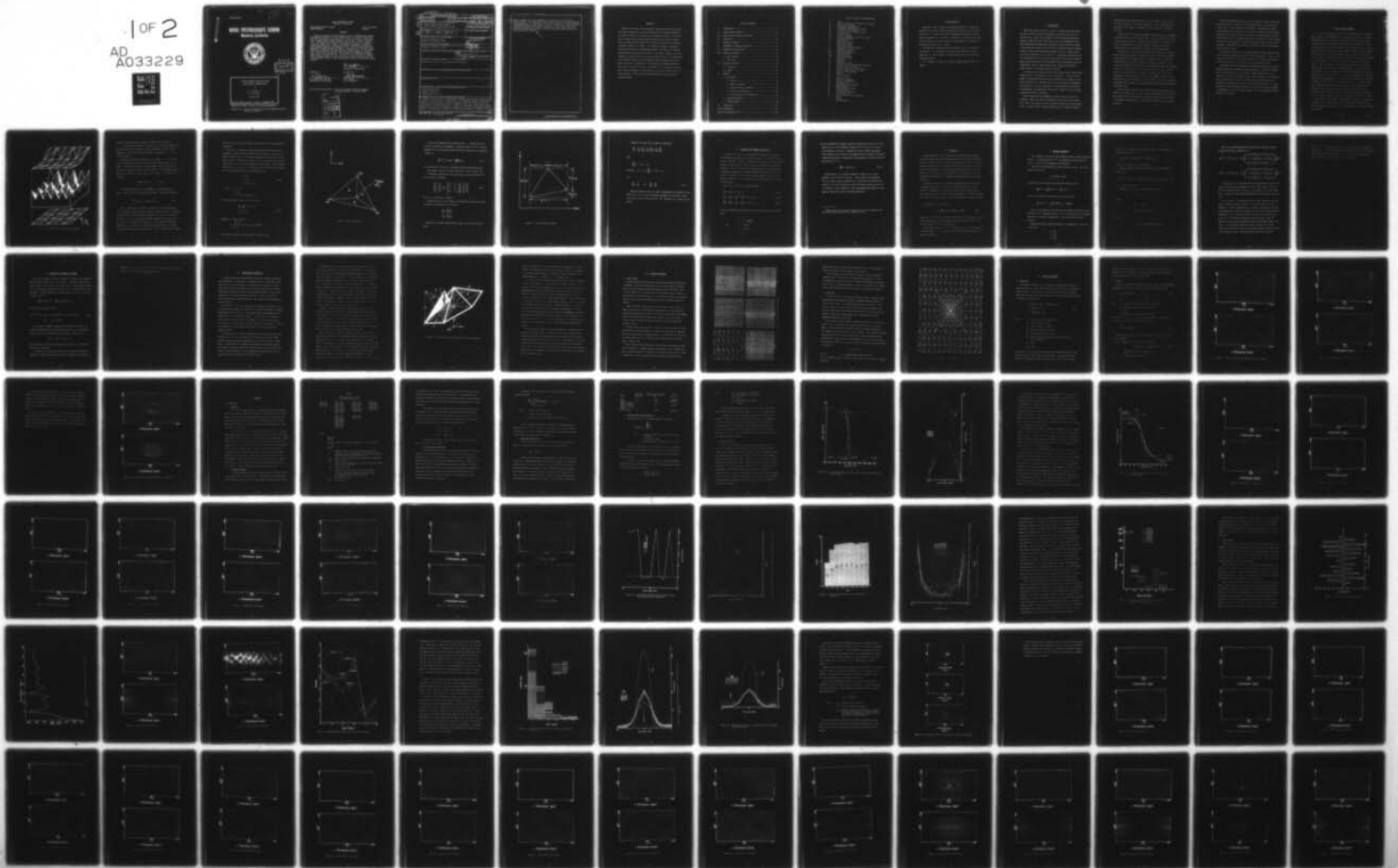
NAVAL POSTGRADUATE SCHOOL MONTEREY CALIF  
A FINITE ELEMENT PREDICTION MODEL WITH VARIABLE ELEMENT SIZES.(U)  
OCT 76 R G KELLEY, R T WILLIAMS  
NPS-63WU76101

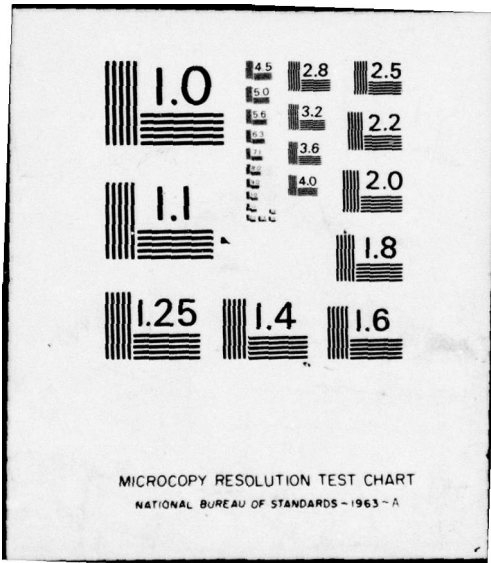
F/G 4/2

UNCLASSIFIED

NL

1 of 2  
AD  
A033229





MICROCOPY RESOLUTION TEST CHART  
NATIONAL BUREAU OF STANDARDS - 1963 - A

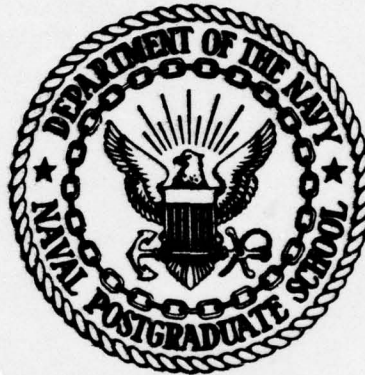
ADA 033229

NPS-63Wu76101

1 (3) J2

# NAVAL POSTGRADUATE SCHOOL

## Monterey, California



DDC  
RECEIVED  
DEC 14 1976  
A

A FINITE ELEMENT PREDICTION MODEL  
WITH VARIABLE ELEMENT SIZES

by

R. G. Kelley, Jr.

R. T. Williams

October 1976

Technical Report Period: January - September 1976

Approved for public release; distribution unlimited.

Prepared for: Naval Environmental Prediction Research Facility,  
Monterey, California

NAVAL POSTGRADUATE SCHOOL  
Monterey, California

Rear Admiral Isham W. Linder  
Superintendent

Jack R. Borsting  
Provost

ABSTRACT

There are a variety of meteorological forecast problems which require high spatial resolution in only a limited area. An important example of this type of problem is the prediction of tropical cyclones. This study tests a simple finite element prediction model with a variable element size. The shallow water equations are used and the motion is confined in a periodic channel on a  $f$ -plane. The Galerkin technique is applied to linear basis functions on triangular elements. The model uses leapfrog time differencing and periodic restarts. The model is tested with a wave imbedded in a mean flow and also with an isolated vortex. The experiments with a uniform element size show excellent phase propagation, but some small scale noise is generated. The introduction of momentum diffusion terms helps to control the noise. The model is also tested with elements which decrease abruptly in scale along a line and with elements which decrease smoothly. Both of these cases generate more noise than with uniform elements.

R. T. Williams

R. T. Williams  
Professor of Meteorology

Approved by:

G. J. Haltiner

G. J. Haltiner, Chairman  
Department of Meteorology

Released by:

M. R. Fossum

R. R. Fossum  
Dean of Research

This task was supported by: Naval Environmental Prediction Research  
Facility, Monterey, California 93940

ACQUISITION NO.	
DTIC	Write Section <input checked="" type="checkbox"/>
DDC	Self Section <input type="checkbox"/>
UNANNOUNCED	<input type="checkbox"/>
JUSTIFICATION	
BY	
DISTRIBUTION/AVAILABILITY CODES	
Dist.	AVAIL. and/or SPECIAL
A	

UNCLASSIFIED

SECURITY CLASSIFICATION OF THIS PAGE (When Data Entered)

REPORT DOCUMENTATION PAGE		READ INSTRUCTIONS BEFORE COMPLETING FORM
1. REPORT NUMBER NPS-63Wu76101	2. GOVT ACCESSION NO.	3. RECIPIENT'S CATALOG NUMBER
4. TITLE (and Subtitle) A Finite Element Prediction Model with Variable Element Sizes.	5. TYPE OF REPORT & PERIOD COVERED Technical Report Period January 1976-September 1976	
7. AUTHOR(s) R. G. Kelley Jr. and R. T. Williams	6. PERFORMING ORG. REPORT NUMBER	
9. PERFORMING ORGANIZATION NAME AND ADDRESS Naval Postgraduate School Monterey, California 93940	8. CONTRACT OR GRANT NUMBER(s)	
11. CONTROLLING OFFICE NAME AND ADDRESS Naval Environmental Prediction Research Facility Monterey, California 93940	10. PROGRAM ELEMENT, PROJECT, TASK AREA & WORK UNIT NUMBERS N6685678WR00008	
14. MONITORING AGENCY NAME & ADDRESS (if different from Controlling Office)	12. 104p.	11. REPORT DATE October 1976
		13. NUMBER OF PAGES 109
		15. SECURITY CLASS. (of this report) Unclassified
		15a. DECLASSIFICATION/DOWNGRADING SCHEDULE
16. DISTRIBUTION STATEMENT (of this Report) Approved for public release; distribution unlimited.		
17. DISTRIBUTION STATEMENT (of the abstract entered in Block 20, if different from Report)		
18. SUPPLEMENTARY NOTES		
19. KEY WORDS (Continue on reverse side if necessary and identify by block number) Finite element model Variable element sizes Tropical cyclone Shallow water equations		
20. ABSTRACT (Continue on reverse side if necessary and identify by block number) There are a variety of meteorological forecast problems which require high spatial resolution in only a limited area. An important example of this type of problem is the prediction of tropical cyclones. This study tests a simple finite element prediction model with a variable element size. The shallow water equations are used and the motion is confined in a periodic channel on a f-plane. The Galerkin technique is applied to linear basis functions on triangular elements. The model uses leapfrog time differencing and periodic restarts. The		

DD FORM 1473 1 JAN 73

EDITION OF 1 NOV 65 IS OBSOLETE  
S/N 0102-014-6601

UNCLASSIFIED

SECURITY CLASSIFICATION OF THIS PAGE (When Data Entered)

251450

next page

JB

model is tested with a wave imbedded in a mean flow and also with an isolated vortex. The experiments with a uniform element size show excellent phase propagation, but some small scale noise is generated. The introduction of momentum diffusion terms helps to control the noise. The model is also tested with elements which decrease abruptly in scale along a line with elements which decrease smoothly. Both of these cases generate more noise than with uniform elements.

#### ABSTRACT

There are a variety of meteorological forecast problems which require high spatial resolution in only a limited area. An important example of this type of problem is the prediction of tropical cyclones. This study tests a simple finite element prediction model with a variable element size. The shallow water equations are used and the motion is confined in a periodic channel on a  $f$ -plane. The Galerkin technique is applied to linear basis functions on triangular elements. The model uses leapfrog time differencing and periodic restarts. The model is tested with a wave imbedded in a mean flow and also with an isolated vortex. The experiments with a uniform element size show excellent phase propagation, but some small scale noise is generated. The introduction of momentum diffusion terms helps to control the noise. The model is also tested with elements which decrease abruptly in scale along a line and with elements which decrease smoothly. Both of these cases generate more noise than with uniform elements.

TABLE OF CONTENTS

I. INTRODUCTION - - - - - 8

II. FINITE LINEAR ELEMENTS - - - - - 11

III. EQUATIONS AND BOUNDARY CONDITIONS - - - - - 19

IV. DIFFUSION - - - - - 21

V. EQUATION FORMATION - - - - - 22

VI. TREATMENT OF BOUNDARY CONDITIONS - - - - - 26

VII. COMPUTATIONAL TECHNIQUES - - - - - 28

VIII. DOMAINS CONSIDERED - - - - - 32

    A. BASIC MESHES - - - - - 32

    B. FINAL MESH - - - - - 34

IX. INITIAL CONDITIONS - - - - - 36

    A. SINUSOIDAL - - - - - 36

    B. VORTEX - - - - - 37

X. RESULTS - - - - - 42

    A. DISCUSSION - - - - - 42

        1. Notation - - - - - 42

        2. Harmonic Analysis - - - - - 42

        3. Matrix Inversion Technique - - - - - 44

        4. Diffusion Coefficients - - - - - 45

        5. Data Reduction and Presentation - - - - - 46

    B. SINUSOIDAL RESULTS - - - - - 47

    C. VORTEX RESULTS - - - - - 66

XI. CONCLUSIONS - - - - - 99

LIST OF REFERENCES - - - - - -102

INITIAL DISTRIBUTION LIST - - - - - -103

LIST OF SYMBOLS AND ABBREVIATIONS

A	area
a	radius of earth or an elementary coordinate
$\alpha$	zonal wind component
$\beta$	meridional wind component
b	elementary coordinate or a vector
d	a length along a diagonal
$d_0$	a constant length along a diagonal
e	element index
f	Coriolis parameter
$f_0$	Coriolis parameter at central latitude
$\phi$	geopotential height
g	test function
$\gamma$	geopotential height
i	nodal point index
j	nodal point index
K	an arbitrary diagonal factor
$K_h$	diffusion coefficient
k	nodal point index
$\mathcal{L} \{ \}$	differential operator
L	area coordinate
LFM	limited fine mesh
l	nodal point index
$\lambda$	longitude
mb	millibar
N	length of an array
n	a time level or a Gauss-Seidel iteration
$\Omega$	angular velocity of earth
r	radial distance from vortex center
$r_0$	maximum radial extent of vortex
t	time or a test function
$\theta$	latitude
$\theta_0$	central latitude
$\bar{U}$	mean zonal wind
u	zonal wind component
V	basis or test function
$V_T$	tangential wind
v	meridional wind component
W	channel width
x	longitudinal coordinate
$x_L$	channel length
y	latitudinal coordinate
z	a field variable
< >	inner product (area integration)
[ ]	matrix
{ }	vector
^	an approximation

#### ACKNOWLEDGEMENTS

The authors wish to thank Lt. D. Hinsman and Prof. D. Salinas who assisted in the finite element formulations and with the code structure, and Prof. G. J. Haltiner who read the manuscript and who made several useful comments on it. Professors C. Comstock, F. Faulkner and R. Haney were also helpful in various aspects of the research. The manuscript was carefully typed by Ms. M. Marks.

The numerical computations were performed by the W. R. Church Computer Center. At the Computer Center, Ms. Chris Butler, Ms. Duffy Tegtmeier, Mr. 'Andy' Anderson, and particularly Mr. Ed Donnellan were especially helpful.

R. G. Kelley, Jr. wishes to thank his family, Matthew, Chris and Helen.

## I. INTRODUCTION

Operational numerical models, because of computational limitations, are able to depict and predict atmospheric processes only down to a limited scale. Until the introduction of the National Meteorological Center's limited fine mesh (LFM) model, which is superimposed on the coarse mesh Northern Hemisphere stereographic grid, grids were uniform on any given map projection and the advent of LFM has brought increased accuracy in wave phase and amplitude prediction due to smaller truncation errors [Houghton and Irvine (1976)]. Nevertheless, problems arise at the boundaries of the fine mesh grid because of the abrupt change in grid size and the need to furnish boundary values interpolated from the coarse mesh. Hence it seems logical that a scheme which permits a gradual change in resolution would be desirable.

A relatively new technique, known as the finite element method (FEM), seemed suited to the problem of a non-uniform grid. In theory the dependent variable may be predicted by this method at any number of locations chosen at will. The main thrust of this particular investigation was therefore to test this hypothesis. Secondary emphasis was placed on determining the computational limitations, computer time and storage requirements of such a procedure.

Only recently have the atmospheric sciences seen the use of the technique. Among the notable contributions are those of Cullen (1973, 1974, 1976); Lee, Gresho, and Sani (personal communication); and Hinsman (1975). Since the finite element method (FEM) is an implicit scheme in

space, physically reasonable solutions involve solving a large system of linear equations. This implies substantial memory requirements and, depending on the technique of matrix inversion, possibly considerable CPU time.

Specifically, the technique of Galerkin (1915) was used to transform the equation set into an integrable form. Galerkin's method has recently been proven invaluable in engineering disciplines. For example, the field of indeterminate structural analysis, pressure vessel and air frame design, and continuum mechanics have all greatly benefited.

The equation set used was the "shallow water", barotropic equations which approximately describe atmospheric motion. These equations model a simple, physically reasonable form of atmospheric motion. Additional simplification was gained by assuming the coriolous parameter,  $f$ , was constant and equal to its value at the mid-channel latitude. This assumption does not degrade model performance significantly since the actual value of  $f$  varies slowly over the domain studied. The value of this approximation lies principally in reducing the number of terms in the equations by two and eliminating the "Beta effect". With no  $f$  variation, sinusoidal waves can move in an east-west direction without any resultant latitudinal tilt.

Two basic types of domains and initial conditions were tested. Both domains were square with a channel length of approximately 3500 kilometers. The channel width was equivalent to a region extending from the equator to 30 degrees north latitude. The channel was periodic in the east-west direction.

Simple experiments were carried out for sinusoidal initial conditions which consisted of a single wave in the longitudinal or x-direction and a half wave in the latitudinal or y-direction. A geopotential surface tilt was added in the y-direction to allow for any mean zonal flow imposed. Numerous tests were performed with these initial conditions using various domain subdivisions. All domain subdivisions were done in a regular manner by varying the grid spacing in either or both the x and y directions over the domain. Additional tests were also conducted on some of these meshes with an analytic vortex.

Final and more complex tests involved a domain on which the grid resolution decreased regularly toward the center of the domain. Initial conditions used consisted of those mentioned above and a localized disturbance or vortex which spanned the central region of varying resolution.

The simpler tests were undertaken to determine the effects of various smooth and abrupt grid changes on model performance. The final, complex model was evaluated with an eye towards ultimate implementation as an operational tool for forecasting tropical cyclone movement. It was hoped that the flexibility of choosing a varying grid resolution would be a significant improvement over current finite difference models. It seems desirable to have a scheme by which one can vary grid resolution smoothly to accommodate the scale of motion changes that occur proceeding radially inward into a typhoon.

## II. FINITE LINEAR ELEMENTS

As is true with the spectral method, the FEM assumes that the dependent variable can be represented by a known function of space. The two techniques differ since spectral approximations are continuous and are infinitely differentiable while FEM functions are defined very locally (over an element), vanishing elsewhere, with limited continuity. Generally, FEM functions are low order polynomials, defined as planar surfaces locally in the case of linear elements. That is, for a given variable,  $\phi$ , one assumes that over each element the basis or local support function  $V_j$  has the form:  $V_j = a + bx + cy$  where  $a$ ,  $b$ , and  $c$  are constants. Figure 1 shows an exploded, three dimensional view of a small domain which has been subdivided into triangular elements. Above this domain lies the group of linear basis functions which are pyramids rising to an approximation of  $\phi$  over a nodal point. Above these pyramids is the segmented, planar approximation of  $\phi$  with dashed cross-sections of the exact  $\phi$  surface at evenly spaced  $\Delta x$  values. Note that  $\phi$  is shown varying only in one direction in this case and that the  $\phi$  approximations,  $\hat{\phi}$ , are shown to be exact at the nodal points. The latter fact is, of course, not true in general. What is required for piecewise continuity in  $\phi_j$  is that no nodal point may be located on the side of a triangle.

Once a form for the unknown as been assumed, Galerkin's technique may be applied. In its basic form, this method assumes an unknown has the following approximate form locally over a nodal point,  $j$  and its surrounding elements:

$$\phi_j = \gamma_j V_j \quad (\text{II-1})$$

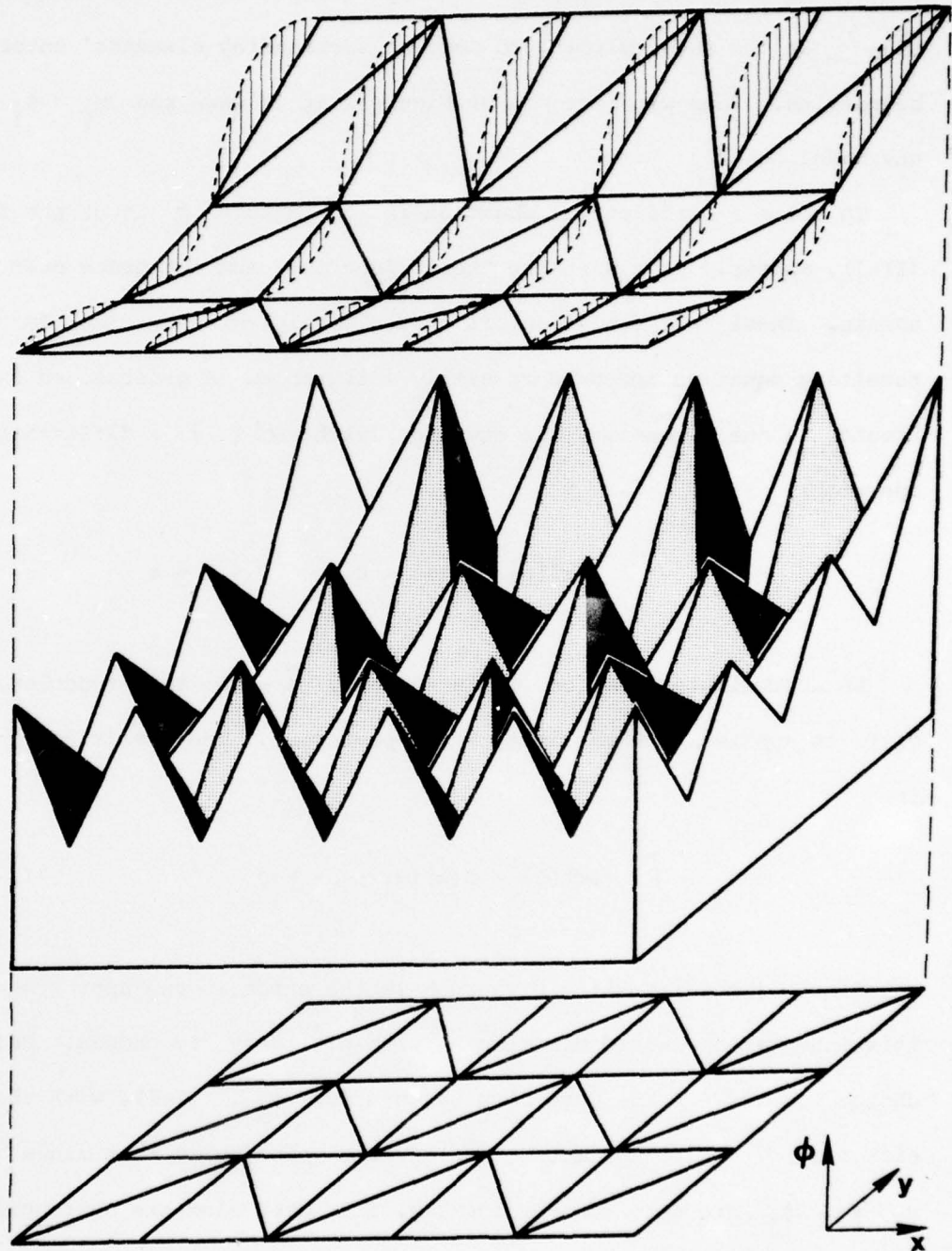


Figure 1. Linear finite element approximation.

(with the repeated subscript implying a sum over that subscript)

$V_j$  is defined as the basis or support function and has maximum value of unity at the node, sloping to zero at surrounding elements' outer boundaries. Thus with the aid of Figure 1 it is seen the  $\gamma_j = \phi_j$  at any nodal point  $j$ .

To solve a differential equation in  $\phi$ , assume  $\phi$  is of the form (II-1), multiply by a suitable "test" function, and integrate over the domain. These test functions, if chosen wisely, greatly simplify the resulting equation and make it easily integrable. A generalized example treats, in one dimension, the equation (with  $\mathcal{L}\{ \}$  a differential operator):

$$\mathcal{L}\{\phi\} - f(x) = 0 \quad 0 \leq x \leq a$$

An approximate form for  $\phi$  is assumed,  $\hat{\phi}$ ; the test function,  $g(x)$ , is applied, and the integration performed. The resulting equation is:

$$\int_c^a [\mathcal{L}\{\hat{\phi}\} - f(x)]g(x) dx = 0 \quad (\text{II-2})$$

Since  $[\mathcal{L}\{\hat{\phi}\} - f(x)] = R$  where  $R$  is the error in the approximation, this integration should minimize  $R$ , with  $g(x)$  properly chosen. Galerkin's choice for  $g(x)$  is the same form as that for  $\phi_j$ , (II-1), with the coefficient  $\gamma_j \equiv 1$ . The attraction of this approach is that since both  $g_j$  and  $\hat{\phi}_j$  are defined only locally, i.e. over elements surrounding nodal point  $j$ , the result is a linear matrix equation which is banded. This results from a partial integration of (II-2). Another useful feature

is that linear elements have domain integrations which are analytically obtainable.

This direct integration is made straightforward through the use of a natural or area coordinate scheme for each element as explained in Desai and Abel (1972). In two space dimensions the location of a point  $P(x,y)$  inside an element (see Figure 2) can be defined by describing the three areas:  $A_1$ ,  $A_2$ , and  $A_3$ , subtended by lines from  $P$  to the triangle's vertices  $(x_j, y_j, j=1, 2, 3)$ . Zienkiewicz (1971) shows how the location of  $P$  can be transformed into area coordinates via:

$$\begin{aligned}x &= L_j x_j \\y &= L_j y_j \\1 &= L_1 + L_2 + L_3\end{aligned}\tag{II-3}$$

with:  $j = 1, 2, 3$

$$L_j = A_j/A$$

$A$  = total elementary area

If the differential equation to be solved is:

$$\begin{aligned}\frac{\partial \phi}{\partial x} + \frac{\partial \phi}{\partial y} + \phi(x,y) &= 0 \\x_1 \leq x \leq x_2 \\y_1 \leq y \leq y_2\end{aligned}\tag{II-4}$$

Galerkin's technique yields:

$$\gamma_i \int_{y_1}^{y_2} \int_{x_1}^{x_2} (v_{ix} + v_{iy} + v_i) v_j dx dy = 0$$

with variable subscript implying partial differentiation.

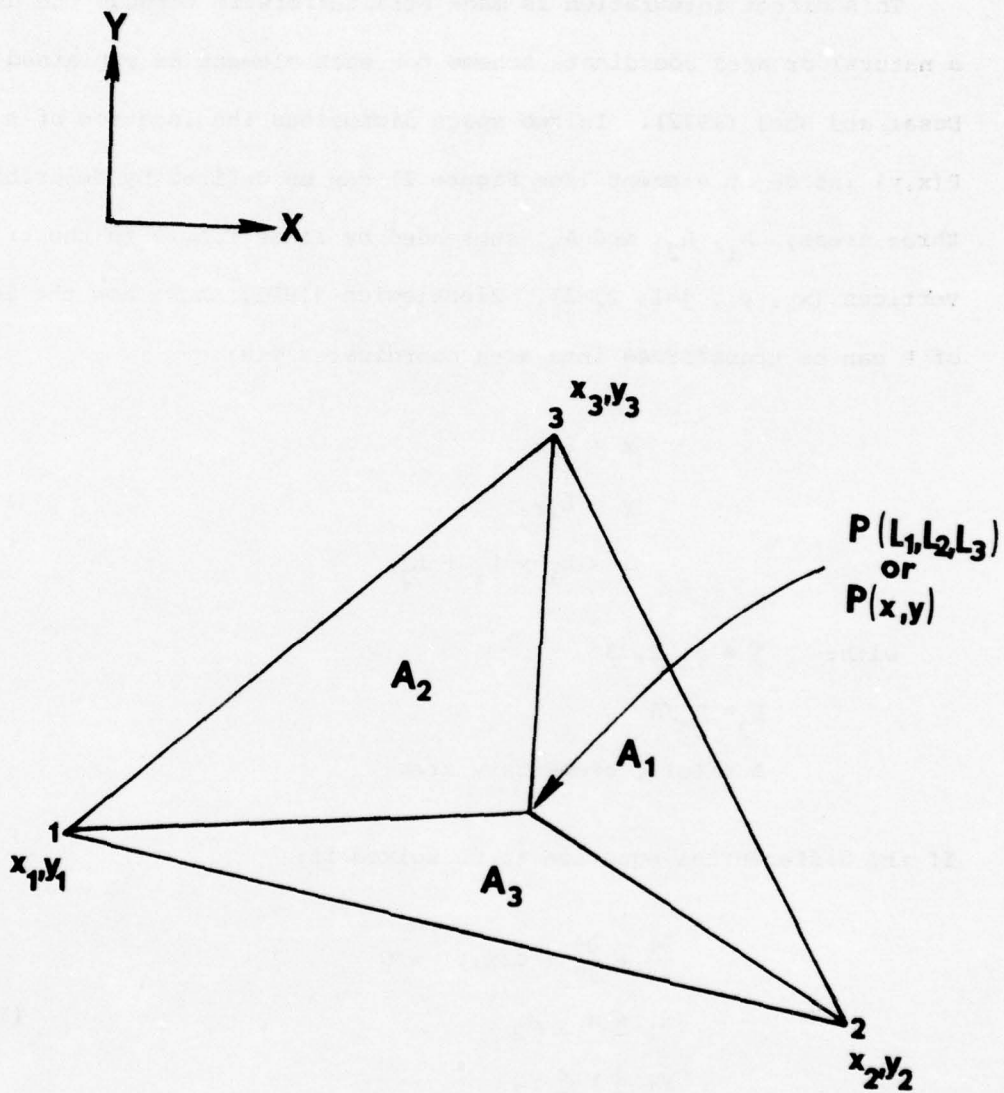


Figure 2. Area coordinates.

This matrix equation may be solved for the  $\gamma_i$  coefficients once the area integration is performed. Zienkiewicz show that for triangular elements with linear basis and test functions a general area integration formula is:

$$\iint L_1^m L_2^n dx dy = \frac{m!n!}{(m+n+2)!} 2A \quad (\text{II-5})$$

It is noted that, for  $m, n > 1$ , non-linear terms are being formulated.

For example, with  $m=1$  and  $n=2$ , the value of (II-5) becomes  $\frac{A}{30}$ .

Transforming equation set (II-3) into matrix form and solving for the L vector one obtains:

$$\begin{Bmatrix} L_1 \\ L_2 \\ L_3 \end{Bmatrix} = \frac{1}{2A} \begin{bmatrix} 2A & b_1 & a_1 \\ 2A & b_2 & a_2 \\ 2A & b_3 & a_3 \end{bmatrix} \begin{Bmatrix} 1 \\ x \\ y \end{Bmatrix} \quad (\text{II-6})$$

with  $a_i, b_i$  as defined in Figure 3.

Differentiation of (II-6) shows the differential operations desired to complete the integration of (4) are:

$$\frac{\partial}{\partial x} = \frac{b_i}{2A} \frac{\partial}{\partial L_i}$$

$$\frac{\partial}{\partial y} = \frac{a_i}{2A} \frac{\partial}{\partial L_i}$$

(Henceforth a repeated subscript will imply a sum from one through three.)

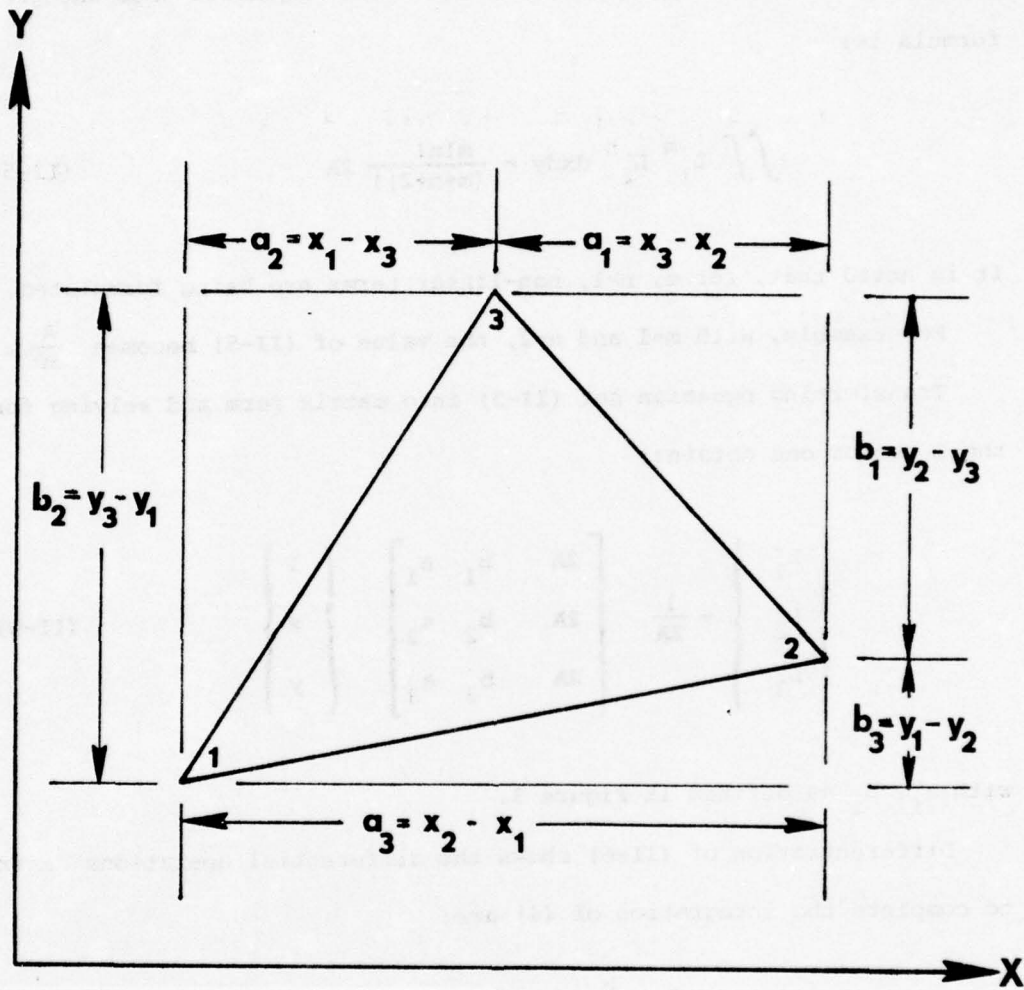


Figure 3. Local coordinate system.

Applying the chain rule in natural coordinates:

$$\frac{\partial v_i}{\partial x} = \frac{b_1}{2A} \frac{\partial v_i}{\partial L_1} + \frac{b_2}{2A} \frac{\partial v_i}{\partial L_2} + \frac{b_3}{2A} \frac{\partial v_i}{\partial L_3}$$

but

$$\frac{\partial v_i}{\partial L_k} = 0 \quad \text{for } i \neq k$$

and since  $v_i = L_i$ ;  $\frac{\partial v_i}{\partial L_k} = 1$  for  $i = k$

so

$$\frac{\partial v_i}{\partial x} = \frac{b_i}{2A} \quad \text{and} \quad \frac{\partial v_i}{\partial y} = \frac{a_i}{2A} \quad (\text{II-7})$$

Therefore equation (II-4) is easily integrated on an elementary level. These results can then be distributed throughout the resultant coefficient matrix and the solution vector  $\{\hat{\phi}\}$  obtained via a linear equation solver.

### III. EQUATIONS AND BOUNDARY CONDITIONS

A form of the barotropic, shallow water, primitive equations was selected which was developed by Phillips (1959). The original intent of this study was to develop a complete, barotropic model for a tropical channel. Time limitations forced the use of a model which was purely cartesian. That is, although the original equation set was designed in mercator coordinates, a constant map factor of unity was used. In theory, and based on other work done by this author, extension of the Galerkin formulation of the equation set to include complete sphericity is easily done.

The set in cartesian coordinates becomes

$$\frac{\partial \phi}{\partial t} = -\left[\frac{\partial}{\partial x} (u\phi) + \frac{\partial}{\partial y} (v\phi)\right] \quad (\text{III-1})$$

$$\frac{\partial u}{\partial t} = -\left[\frac{\partial \phi}{\partial x} + u \frac{\partial u}{\partial x} + v \frac{\partial u}{\partial y}\right] + 2\Omega v \sin \theta_0 \quad (\text{III-2})$$

$$\frac{\partial v}{\partial t} = -\left[\frac{\partial \phi}{\partial y} + u \frac{\partial v}{\partial x} + v \frac{\partial v}{\partial y}\right] - 2\Omega u \sin \theta_0 \quad (\text{III-3})$$

with the transform from spherical to the cartesian system accomplished using:

$$x = a\lambda$$

$$y = a \ln \frac{\cos \theta}{1 - \sin \theta}$$

and

$$\theta = \text{latitude}$$

$$\lambda = \text{longitude}$$

$$\theta_0 = 15^\circ$$

The only mathematical boundary conditions imposed were those of no cross channel flow at the latitudinal boundaries and of cyclic continuity in the longitudinal direction. Through the course of model development other conditions were tried at the boundaries due to physical constraints. A geostrophic balance at channel walls was imposed in the mass continuity equation(III-1)<sup>1</sup>, i.e.:

$$\frac{\partial \phi}{\partial y} = - 2\Omega u \sin \theta_0 \quad (\text{III-4})$$

Additionally it was thought necessary to impose a zero normal gradient of zonal wind at the walls. During some early experiments with an abruptly varying element size, it was found that imposing this condition on the zonal equation of motion yielded instability after six to 12 hours of time integration. Later experimentation showed the zonal equation required no explicit boundary conditions.

---

<sup>1</sup>This condition is consistent with that of no cross boundary flow and follows from inserting  $V=0$  in equation (III-3).

#### IV. DIFFUSION

Early experiments with a coarse mesh indicated that some type of filtering would be required since short waves of twice the coarse grid size were readily generated. These short waves were evident in the disturbance patterns of the geopotential and zonal wind fields. Since experience and knowledge of atmospheric FEM applications is still in its infancy it is not known if this phenomenon is an artifact of the time stepping scheme employed, the boundary conditions imposed, or the basic technique.

A simplistic, second order diffusive damping term was included in the equations of motion. To keep the Galerkin formulation of the diffusion consistent with first order terms, an area integration was performed and Gauss' divergence theorem was applied. Consider the diffusion term in the zonal equation (III-2) with Galerkin's technique applied:

$$\begin{aligned} K_H \int_A \nabla^2 u v_j dA &= K_H \int_A \nabla \cdot \nabla u v_j dA \\ &= K_H \left\{ \oint v_j \nabla u \cdot \hat{n} dr - \int_A \nabla v_j \cdot \nabla u dA \right\} \end{aligned} \quad (IV-1)$$

where  $dr$  is differential distance along the path of integration on the outer boundary,  $K_H$  is the horizontal viscosity coefficient and  $\hat{n}$  is the unit normal to the area or domain,  $A$ .

The contour integral in (IV-1) vanishes due to cyclic continuity and an implied  $\frac{\partial u}{\partial y} = 0$ . The diffusion term in the meridional equation is advanced similarly.

## V. EQUATION FORMATION

As an example of the use of the Galerkin technique consider equation (III-1). A consistent form for  $\hat{\phi}$  was assumed and substituted into (III-1). Then an area integration was performed.

Defining the inner product of a basis function  $g(x,y)$  and a test function,  $V(x,y)$  as:

$$\int_Y \int_X gV \, dx dy \equiv \langle g, V \rangle$$

An application of the FEM to the continuity equation gives:

$$\langle \frac{\partial \phi}{\partial t}, V \rangle = - \langle \frac{\partial}{\partial x} (u\phi), V \rangle - \langle \frac{\partial}{\partial y} (v\phi), V \rangle$$

A partial integration of the x-derivative term yields:

$$\langle \frac{\partial}{\partial x} (u\phi), V \rangle = \int_A \frac{\partial}{\partial x} (u\phi V) \, dA - \int_A u\phi \frac{\partial V}{\partial x} \, dA$$

But the first term on the right hand side vanishes because of cyclic continuity in x. Similarly, since  $v = 0$  on the boundary, the corresponding term in the partial integration of the y-derivative term also vanishes.

Applying Galerkin's linear technique it is assumed  $\phi$ ,  $u$ , and  $v$  are of the form

$$\phi = \gamma_j V_j$$

$$u = \alpha_j V_j$$

$$v = \beta_j V_j$$

which, with a concurrent test function assumption, transforms the continuity equation to:

$$\dot{\gamma}_j \langle v_j, v_i \rangle = \gamma_j [\langle \alpha_k v_k v_j, v_{ix} \rangle + \langle \beta_k v_k v_j, v_{ij} \rangle]$$

where the dot denotes a time derivative.

Using a centered finite time difference the final form of the equation is:

$$(\gamma_j^{n+1} - \gamma_j^{n-1}) \langle v_j, v_i \rangle = 2\Delta t \gamma_j^n [\langle \alpha_k^n v_k v_j, v_{ix} \rangle + \langle \beta_k^n v_k v_j, v_{ij} \rangle] \quad (V-1)$$

with n being a time level.

Equation (V-1) is a matrix equation of the form

$$[A] \{x\} = \{b\}$$

where:

$$[A] = \langle v_j, v_i \rangle$$

$$\{x\} = (\gamma_j^{n+1} - \gamma_j^{n-1})$$

and

\{b\} the right-hand side of (V-1).

The u and v momentum equations were similarly advanced including diffusion and become, respectively:

$$(\alpha_j^{n+1} - \alpha_j^{n-1}) \langle v_j, v_i \rangle = 2\Delta t \begin{pmatrix} -\alpha_j^n [\langle \alpha_k^n v_{k jx}, v_i \rangle + \langle \beta_k^n v_{k jy}, v_i \rangle] \\ + 2\Omega \langle \sin\theta \beta_k^n v_{k, v_i} \rangle - \langle \gamma_k^n v_{kx}, v_i \rangle \\ -K_H [\langle \alpha_k^n v_{kx}, v_{ix} \rangle + \langle \alpha_k^n v_{ky}, v_{iy} \rangle] \end{pmatrix} \quad (v-2)$$

$$(\beta_j^{n+1} - \beta_j^{n-1}) \langle v_j, v_i \rangle = 2\Delta t \begin{pmatrix} \beta_j^n [\langle \alpha_k^n v_{k jx}, v_i \rangle + \langle \beta_k^n v_{k jy}, v_i \rangle] \\ + 2\Omega \langle \sin\theta \alpha_k^n v_{k, v_i} \rangle + \langle \gamma_k^n v_{ky}, v_i \rangle \\ -K_H [\langle \beta_k^n v_{kx}, v_{ix} \rangle + \langle \beta_k^n v_{ky}, v_{iy} \rangle] \end{pmatrix} \quad (v-3)$$

At this point it is noted that all the inner products are functions only of space and need be computed but once. Also useful is the fact that the coefficient matrix,  $\langle v_j, v_i \rangle$ , is identical in all three equations. Finally, at this stage all equations are uncoupled at any time step.

As is apparent, the time discretization scheme chosen was the leap-frog or centered difference method. It was chosen primarily for its simplicity. Obvious drawbacks are its inherent computational mode and the somewhat more restrictive maximum time step than some semi-implicit schemes may allow. The latter factor was expected to and did play a major role in the amount of computational time involved since the smallest grid resolution essentially limits the maximum allowable time step. It was expected, based on the work of Cullen (1973) using simple linear advection, that the time step criterion would be slightly more restrictive than a finite difference scheme with equivalent

resolution. The leapfrog scheme used a half-forward, half leapfrog time step to start. Also, early experiments showed strong solution separation. This tendency was kept in check with a periodic restart, identical to the initial start, being applied every 12 time steps.

## VI. TREATMENT OF BOUNDARY CONDITIONS

The cyclic boundary condition is naturally included in the system by defining how the nodal points are connected. Remaining conditions are those imposed at the northern and southern walls. The geostrophic condition is essentially independent of time, so, to fit this condition into the model, boundary equations at distinct times,  $n+1$  and  $n-1$ , were subtracted. That is:

$$\left(\frac{\partial\phi}{\partial y} - 2\Omega\sin\theta_o u\right)^{n+1} - \left(\frac{\partial\phi}{\partial y} - 2\Omega\sin\theta_o u\right)^{n-1} = 0$$

The Galerkin formulation gives:

$$(\gamma_j^{n+1} - \gamma_j^{n-1}) \langle v_{jy}, v_i \rangle = -f_o [\langle \alpha_j^{n+1} v_j, v_i \rangle - \langle \alpha_j^{n-1} v_j, v_i \rangle] \quad (\text{VI-1})$$

$$\text{with } f_o = 2\Omega\sin\theta_o$$

The rigid wall boundary formulation merely required setting the Galerkin approximation for meridional wind to zero at the  $i$  boundary points initially, and requiring no time change in these values:

$$(\beta_j^{n+1} - \beta_j^{n-1}) \langle v_j, v_i \rangle = 0$$

These boundary conditions were applied at all points,  $i$ , on northern and southern boundaries.

It should be realized that the geostrophic boundary formulations imply that a different coefficient matrix is formed than that shown in

equations (V-1, V-2, V-2). The only terms in these matrices which are different are those in the boundary equations.

## VII. COMPUTATIONAL TECHNIQUES

A primary operational disadvantage of any finite element technique is the requirement of large amounts of computer storage. This results from the system of linear equations. The problem is not as bad as it first seems since in any one equation of an  $N \times N$  system a majority of coefficient matrix elements are zero. The problem then reduces to inverting a system with a very sparse coefficient matrix. If one can utilize an equation solver which takes advantage of this property, core requirements can be minimized.

Specifically, for the  $i$ th nodal point, the number of non-zero entries in the coefficient matrix for equation  $i$  is one plus the number of elements surrounding that nodal point. Some storage schemes take advantage of the banded nature of the coefficient matrix. The band width is determined by the largest different between the number,  $i$ , of the  $i$ th equation and the numbers of the nodal points locally connected to nodal point  $i$ . Minimal bandwidth is thereby gained by choosing an efficient nodal point numbering scheme.

It was decided not to minimize bandwidth structure for any cases under consideration since the time involved in selecting an efficient number scheme for differing domains possessing cyclic continuity could be better spent. A disadvantage of a banded matrix scheme is the storage of some zero values; a possible problem when large systems are to be solved. This author's unbanded approach has the disadvantage of forcing the use of an iterative solution technique for the linear system.

To fully compact the coefficient matrix a novel technique was used which was developed by Salinas (private communication). Essentially, only non-zero coefficient matrix entries are retained. The coefficient matrix is stored as a linear vector. Three vectors herein called NUM, ISTART, and NAME, are required to use the method. NUM contains for each  $j$  nodal point the number of points interacting with  $j$  including itself. NAME gives the information of which nodal points interact with  $j$  including  $j$ . ISTART tells where, in NAME, the numbers of the points interacting with  $j$  begin. NUM and ISTART are both dimensioned  $N$  for a system with  $N$  unknowns. NAME is dimensioned to the length of non-zero entries in the coefficient matrix. That is, NAME's dimension is the sum of the number of nodal point interactions.

The matrix assemblage required is mathematically equivalent to multiplying each basis function on a nodal point by nodal point basis by the correct test functions, and then integrating over the portion of the domain spanned by these functions. Graphically, as shown in Figure 4, the basis function at  $j$  is shown outlined in heavy black over a group of elements around nodal point  $j$ . Portions of the test functions which interact with this basis function are also shown.

Since, in the case of linear elements, the domain integration is analytically obtained over an element, the matrix assemblage of an inner product, such as  $\langle v_j, v_i \rangle$ , is done most efficiently on an elementary level. To accomplish this, a local numbering scheme is required for each element. This table was stored in the two dimensional array, NPTS ( $N,3$ ). NPTS contains, for each element,  $e$ , a set of the three global nodal points which define  $e$ . For each element these numbers are stored sequentially according to number of the second dimension of NPTS. The

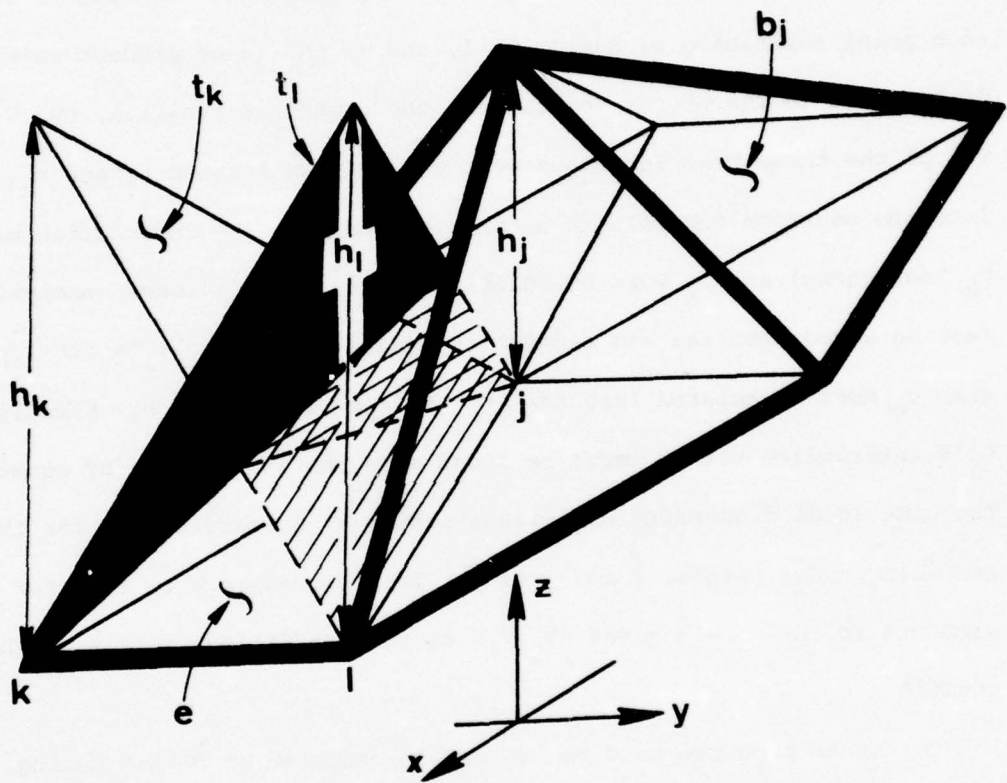


Figure 4. A basis function and portions of two test functions.

choice of the point,  $k$ , to start numbering  $e$  was arbitrary, but, once chosen, the remaining two points were numbered in sequence proceeding in a positive sense around  $e$ . For example in Figure 4 element  $e$  is labeled NPTS  $(e,1) = k$ , NPTS  $(e,2) = l$ , and NPTS  $(e,3) = j$ .

To illustrate matrix assembly using an element by element technique consider again Figure 4. The computational technique required is for each point describing  $e$ ; namely  $k$ ,  $l$ , and  $j$ ; the inner product value be distributed to its proper location in the coefficient matrix,  $\langle V_j, V_i \rangle$ . Two of the three test functions over  $e$  are drawn labeled  $t_l$  and  $t_k$ . Into the equation for point  $k$  a contribution from the interaction between  $b_k$  (not shown) and  $t_k$  must be added; that is,  $\langle b_k, t_k \rangle$  (known analytically) must be added into the  $k$ th element of equation  $k$ . Also  $t_l$ 's interaction with  $b_k$  must be entered into the  $l$ th element of equation  $k$ . Finally,  $t_j$ 's interaction with  $b_k$  must be added into the  $j$ th element of equation  $k$ . The same local dispensing of interactions must be carried out for the remaining nodal points,  $l$  and  $j$  of  $e$ . This procedure when done for all elements in the domain gives  $\langle V_j, V_i \rangle$  or the coefficient matrix of the equation.

The inner products used may either be computed as needed during the equations' time integration or computed prior to time integration and stored for all time. The latter method was followed since the original computer system used was in IBM 360/67 which is relatively slow by today's standards but was able to handle the core requirements of the problems tested. Also, since varying size elements would be used and the equations require numerous time steps for even a six hour forecast, an inner product storage is most efficient.

## VIII. DOMAINS CONSIDERED

### A. BASIC MESHES

To gain experience with the FEM, numerous grid meshing schemes were considered. The first problem chosen was one which required a minimal amount of central memory storage and execution time. This mesh is presented in Figure 5(a). Actual tests were conducted on grids similar to the remaining portions of Figure 5. In all cases the domain is a bounded channel, cyclic in the east-west direction with a width and height of 3503 km.

Higher resolution, regular grids were also used. One of these is shown in Figure 5(b). The domain was divided into 12 latitudinal and longitudinal subdivisions (12x12). A finer resolution used on this domain had twice the resolution as Figure 5(b), (24x24), and is not shown. A coarser scheme (not shown) had six latitudinal and longitudinal subdivisions, (6x6).

Irregular grids were also used. Figure 5(c) shows the first of these tested wherein a central region in the x-direction had half the external mesh size covering half the channel length. A similar grid was used with a varying resolution in y. These two were combined to give the grid shown in Figure 5(d).

Other irregular grids were used in which, rather than abruptly changing the resolution, a smooth gradation was employed. The x varying version is shown in Figure 5(e) along with the version which varies in x and y, Figure 5(f). This zonal and meridional variation was made with no

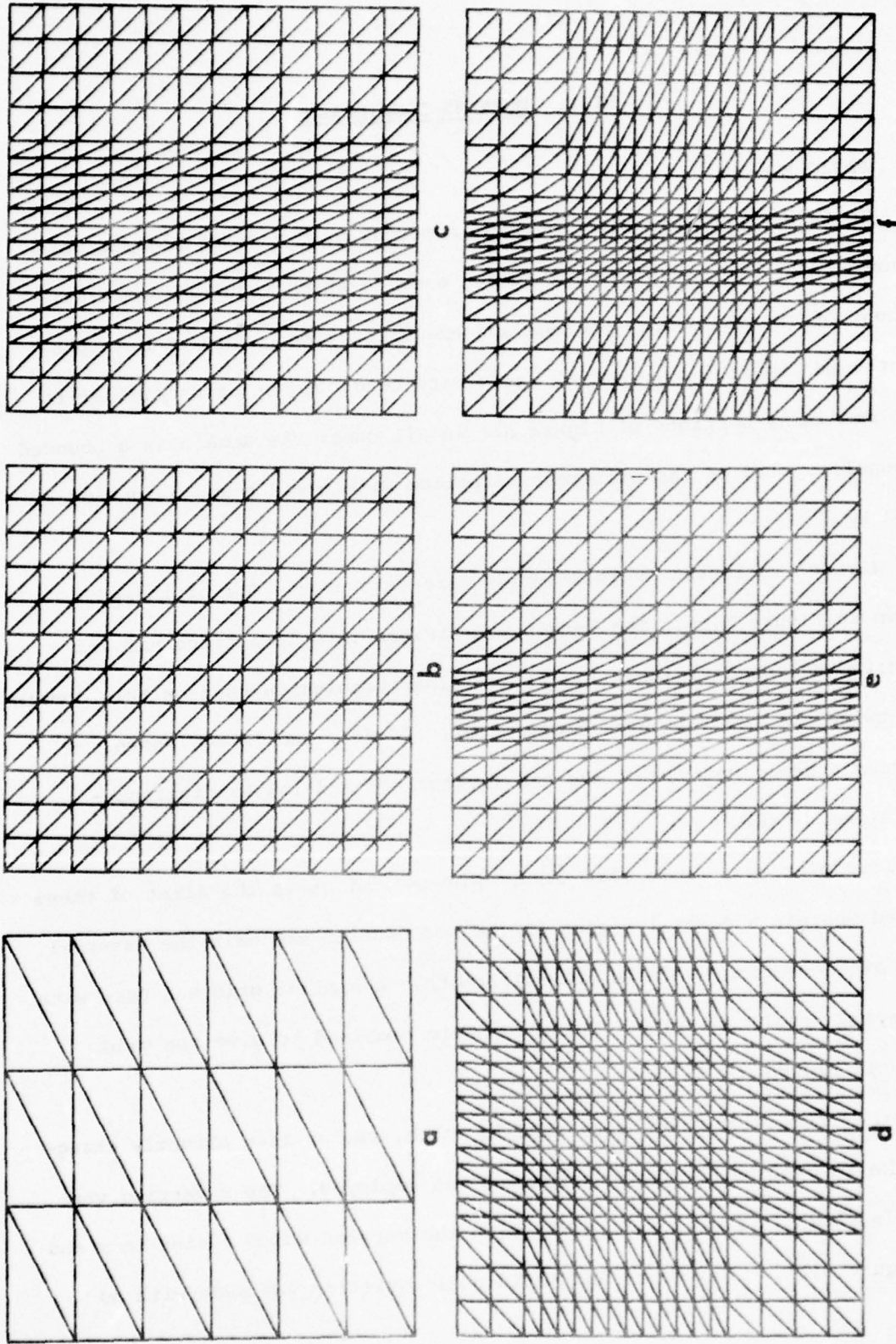


Figure 5. Regular and graded meshes.

particular plan other than a smooth transition to an inner region of half the external or near boundary element sizes.

All the grids so far mentioned were coded to allow a reversal in diagonal slant. Intuitively, from examination of Figure 5, it would be surprising if some bias was not introduced when domains are divided with a built in diagonal preference. These same grids were also tested with an alternating diagonal slant similar to that shown in Figure 6.

#### B. FINAL MESH

In order to study a relatively small-scale vortex, a meshing scheme was developed whose spatial resolution increased radially toward the center of the vortex. The grid developed is shown in Figure 6. The routine used to locate the nodal points was executed independently of the time integration and its results were read in prior to overall integration. Input data included nodal point locations and the local elementary numbering scheme, NPTS.

This program was made flexible in order to allow for a varying resolution over an even number of latitude/longitude blocks in the total domain. Also included was a scheme by which the radial resolution on the subdomain could be varied in a regular manner. This procedure involved decreasing the distance between nodal points along the diagonals which extend from the corner points of the subdomain by increasing even powers of an arbitrary factor,  $K$ . This is, for the five diagonal divisions shown of length  $d_j$ :

$$d_j = (K)^{2^j} d_0$$

with  $K < 1$

$d_0$  = ungraded domain diagonal length

In the ungraded region the diagonal slants were varied as shown to minimize any bias.

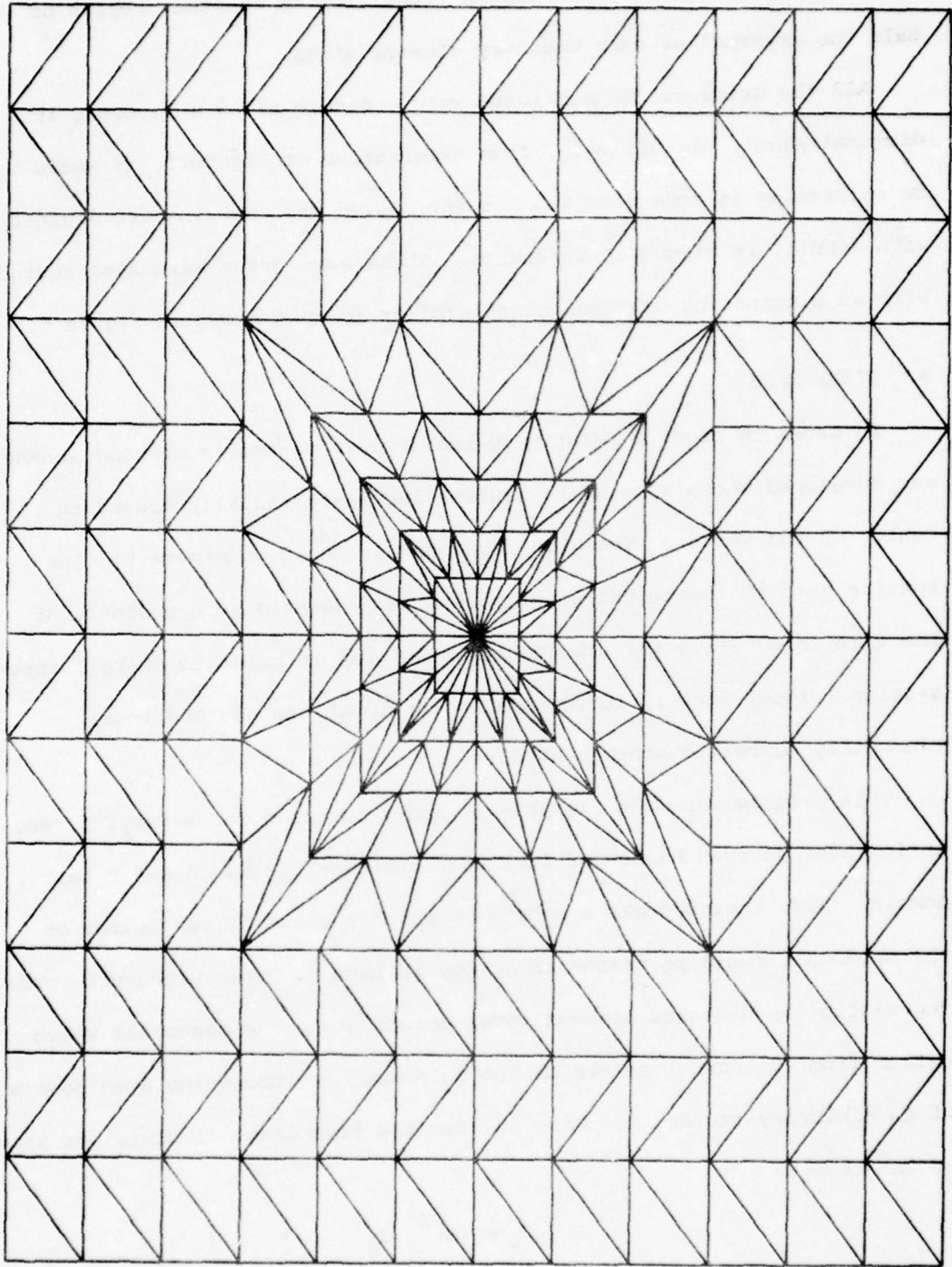


Figure 6. Final mesh.

## IX. INITIAL CONDITIONS

### A. SINUSOIDAL

For the basic testing on the rectangularly subdivided grids such as shown in Figure 5, simple initial conditions were used which consisted of a single wave in the x direction and one half wave in the y direction. Such initial conditions which satisfy the non-linear balance equation with f constant are given below:

$$\begin{aligned}\phi &= f_0 A \sin\alpha_1 \cos\alpha_2 - f_0 \bar{U}(y-y_m) + \phi_0 \\ u &= \bar{U} \frac{A\pi}{w} \cos\alpha_1 \cos\alpha_2 \\ v &= -\frac{2\pi A}{X_L} \sin\alpha_1 \sin\alpha_2\end{aligned}\tag{IX-1}$$

with

$$\begin{aligned}A &= \text{arbitrary perturbation amplitude} \\ W &= \text{channel width} = 3500 \text{ km} \\ X_L &= \text{channel length} = 3500 \text{ km} \\ \bar{U} &= \text{mean zonal wind} = 10 \text{ m sec}^{-1} \\ y_m &= \text{mid latitude value of } y = W/2 \\ \phi_0 &= \text{mean free surface geopotential height chosen as} \\ &\quad 4.9 \times 10^4 \text{ m}^2 \text{ sec}^{-2} \\ \alpha_1 &= \pi y/W \\ \alpha_2 &= 2\pi x/X_L\end{aligned}$$

Two values of A were tested; one which gave a maximum perturbation zonal wind of  $5.5 \text{ msec}^{-1}$  and another for  $0.55 \text{ msec}^{-1}$ . A mean zonal flow of  $10 \text{ msec}^{-1}$  was imposed in some experiments with this initial condition.

The initial conditions with and without zonal flow are presented in Figures 7 and 8 respectively. The perturbation amplitude in both cases is for a perturbed zonal wind of  $5.5 \text{ msec}^{-1}$ .

#### B. VORTEX

Analytic initial conditions were used for a small scale perturbation.

A tangential wind,  $V_T$ , was defined in cylindrical coordinates as:

$$V_T = A \frac{r}{r_0} \sin^2(cr) \quad r \leq r_0 \quad (\text{IX-2})$$

$$V_T = 0 \quad r > r_0$$

with  $r$  = radial distance from center of perturbation

$r_0$  = maximum radial extent of perturbation

$$c = \pi/r_0$$

$A$  = arbitrarily chosen amplitude in  $\text{msec}^{-1}$

An analytic value of  $\phi'(r)$ , the disturbance portion of geopotential, can be obtained from the gradient wind equation:

$$\frac{V_T^2}{r} + f_0 V_T = \frac{\partial \phi'}{\partial r} \quad (\text{IX-3})$$

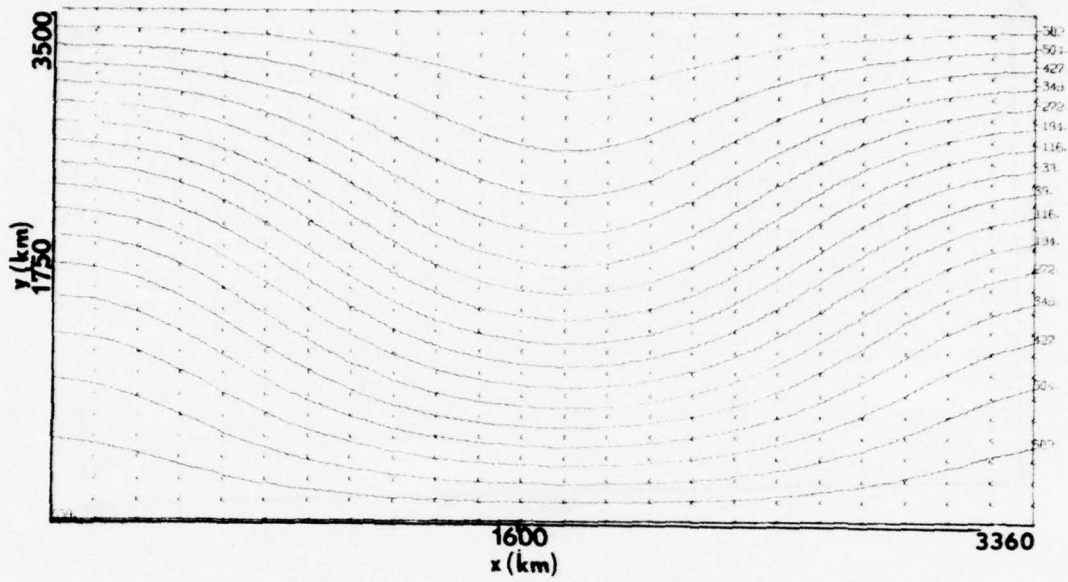
Integrating (IX-3) radially outward from the center of the vortex

( $r=0$ ) one obtains:

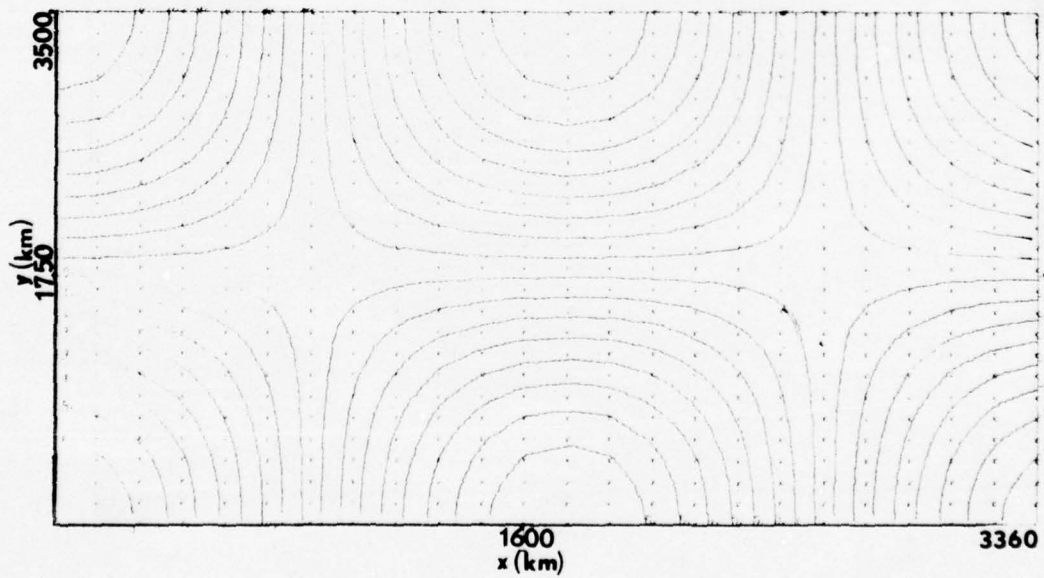
$$\phi'(r) = \frac{A^2}{2r_0} \left\{ \frac{3}{16} r^2 - \frac{r}{4c} [\sin(2cr) - \frac{1}{8} \sin(4cr)] - \frac{1}{8c^2} [\cos(2cr) - \frac{1}{16} \cos(4cr)] \right\} + \quad (\text{IX-4})$$

$$\frac{fA}{r_0} \left\{ \frac{r^2}{4} - \frac{r}{4c} \sin(2cr) - \frac{1}{8c^2} \cos(2cr) \right\}$$

+ constant of integration

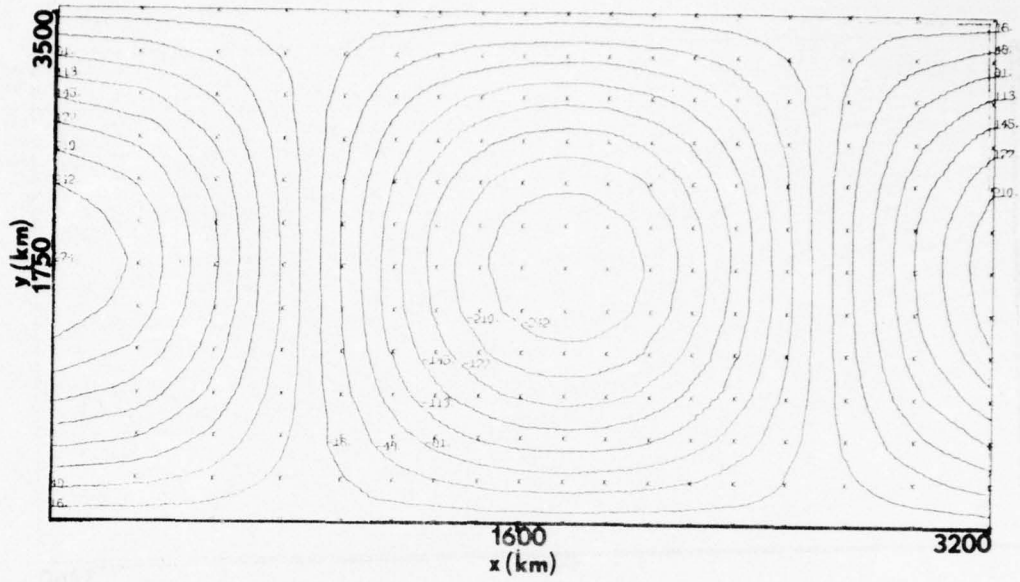


$\phi$  Disturbance (gpm)

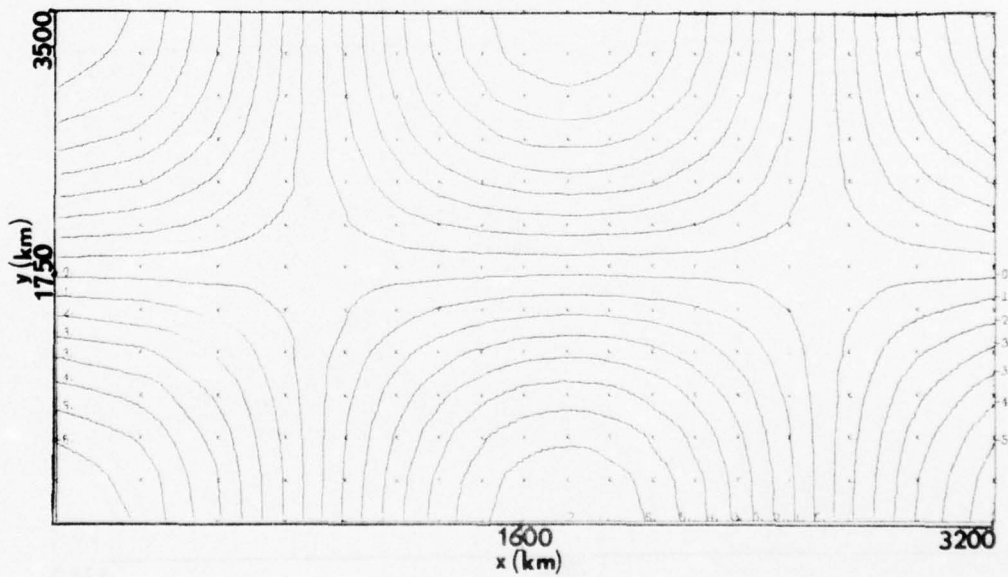


$u$  Disturbance (m/sec)

Figure 7. Initial sinusoidal conditions with  $\bar{U} = 10 \text{ msec}^{-1}$ .



$\Phi$  Disturbance (gpm)

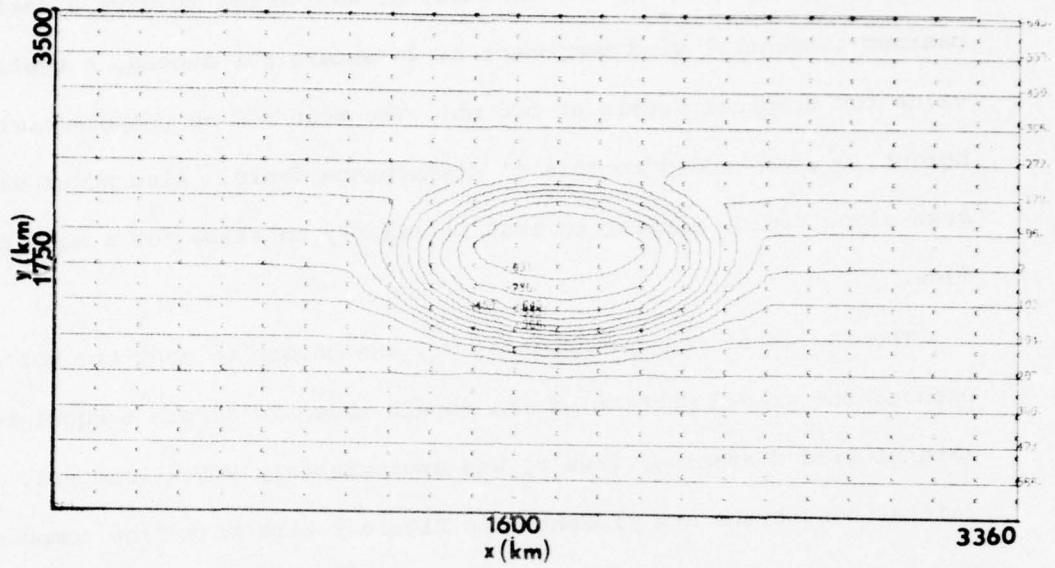


$u$  Disturbance (m/sec)

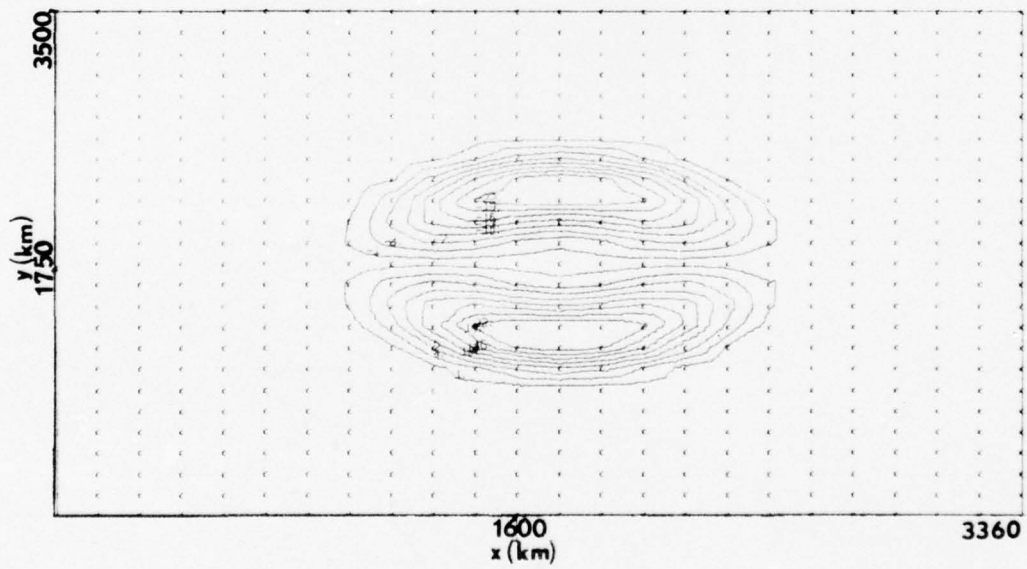
Figure 3. Initial sinusoidal conditions with  $\bar{U} = 0$ .

The amplitude of the disturbance,  $A$ , was chosen to give a desired maximum tangential wind component of 25 meters per second, a realistic value for tropical models at 500 mb. The mean 500 mb geopotential height,  $\phi_0$ , was added to this  $\phi'$  disturbance field. Also added was a mean slope field, similar to that in (IX-1), to allow for a mean zonal flow.

The radius of the disturbance,  $r_0$ , was chosen so that the vortex spanned the graded portion of the domain shown in Figure 6 equal to six largest grid distances; thus  $r_0$  was approximately 875 kilometers. The initial conditions are presented in Figure 9 with mean flow component shown only in the  $\phi'$  field.



$\phi$  Disturbance (gpm)



$u$  Disturbance (m/sec)

Figure 9. Initial vortex conditions with  $\bar{U} = 10 \text{ msec}^{-1}$ .

## X. RESULTS

### A. DISCUSSION

#### 1. Notation

The use of various meshes on the same domain enabled a detailed study of the basic properties of the FEM. Obviously the order of case study proceeded from the coarsest, 6x6 grid mesh to an 18x18 mesh with varying resolution in both directions to the 24x24 mesh which had the best overall resolution. To simplify the task of referencing all cases considered (see Table I).

All the above cases were integrated through 48 hours. A maximum stable time step was roughly found using Cullen's (1973) work as a guide. Cullen states that for simple, two dimensional, linear advection, a stable FEM time step is  $1/\sqrt{3}$  times that of the corresponding finite difference (leapfrog) scheme. For the 12x12 mesh with a mean flow of 10 meters per second, Cullen's criterion gives a stable time step of 8.8 minutes. A nine minute time step was found unstable on the 12x12 while an eight minute time step was stable. This verifies Cullen's analysis since a corresponding stable finite difference time step is slightly in excess of 15 minutes. Time truncation errors were not of primary concern in this study, so close to maximum time steps were always used.

#### 2. Harmonic Analysis

A harmonic analysis routine of the geopotential fields was used at specified times in the integration. This analysis was accomplished along constant latitude circles for wave numbers through three, six and

TABLE I

Experiment Abbreviations  
(all valid at 48 hours)

6x6 [SD]	12x12 [SD]	18x12 [SD]	12x18 [SD]
6x6 [S1D]	12x12 [SND]	18x12 [S**D]	12x18G[SD]
6x6 [S2D]	12x12 [S1D]	18x12G[SD]	12x18 [VD]
	12x12 [S2D]	18x12 [VD]	12x18G[V**D]
	12x12 [S*D]	18x12G[VD]	12x18G[VD]
	12x12 [S*ND]	18x12G[V**D]	
	12x12 [VD]		
	18x18 [SD]	24x24 [SD]	
	18x18 [SND]	24x24 [VD]	
	18x18G[SD]		
	18x18G[SND]		
	18x18 [VD]		
	18x18 [VND]		
	18x18G[VD]		

where

6x6	}	number of rectangular subdomains in X-Y directions
12x12		
⋮		
12x18		
⋮		
24x24		

G	smoothly graded (as opposed to abruptly varying)
S	sinusoidal initial conditions with maximum u perturbation of $5.5 \text{ msec}^{-1}$ and $\bar{U}=10 \text{ msec}^{-1}$
S*	same as S but one-fifth of the perturbation amplitude
S**	same as S but $\bar{U}=0$
V	vortex initial conditions with maximum tangential wind, $V_T = 25 \text{ msec}^{-1}$ and $\bar{U}=10$
V**	same as V but $\bar{U}=0$
1	diagonal slant from upper left to lower right
2	diagonal slant from lower left to upper right (no number implies alternating slant)
D	diffusion included
ND	no diffusion

12 depending on the mesh. Longitudinally averaged wave amplitude information was obtained and used in data reduction. These amplitude data were used to measure generated noise and damping effects. Phase information was used to obtain wave speed by computing phase changes at two hour increments.

The spectral analysis scheme required equally spaced data along a latitude circle. Since some grids tested had unevenly spaced nodal points, the interpolation property of FEM was used in these cases. If a value of a field variable,  $z$ , is known at an element's vertices located at points  $P_i(x_i, y_i)$  ( $i=1,2,3$ ); then the following is true:

$$z_1 = a + bx_1 + cy_1$$

$$z_2 = a + bx_2 + cy_2$$

$$z_3 = a + bx_3 + cy_3$$

Solving this 3x3 system for  $a, b$ , and  $c$ ; one can obtain  $z$  at any point  $P$  interior to the element.

### 3. Matrix Inversion Technique

A straightforward, but time consuming, Gauss-Seidel technique was used for linear system solution for vectors of the three variables in each time step. It was noted that 10 to 15 passes were necessary for system convergence with no explicit boundary conditions. Eighteen to 23 passes were required when boundary conditions were imposed. The conditions were explicitly imposed in the continuity and meridional momentum equations. Also of interest is the fact that convergence was only possible, when applying boundary conditions, if the direction of G-S iteration was reversed every pass.

Convergence was considered to be achieved when the following criterion was met:

$$\frac{|x_i^n - x_i^{n-1}| \max \text{ over } i}{|x_i^n| \max \text{ over } i} \leq 1 \times 10^{-6}$$

with: n being a G-S iteration

i being a nodal point number

$x_i$  being an element of the solution vector, {x}

A more efficient scheme such as sequential over-relaxation is desirable to save time. Actual project completion required the use of many meshes all of which probably possess different optimum over-relaxation factors, so G-S was used for expediency.

#### 4. Diffusion Coefficients

A working maximum stable diffusive coefficient,  $K_{hm}$ , which is equal to a comparable finite difference value was defined as:

$$K_{hm} = \Delta x^2 / 4\Delta t$$

Using this as a maximum, various values of  $K_h$  were tried on the 12x12 grid. Values ranging from .0005 to .05 of  $K_{hm}$  were tried and the spectral and visual results compared. The ideal was to use as little possible diffusion but enough to control generation of noise in higher wave numbers. A subjective value was obtained of .005  $K_{hm}$  which was used in all tests including diffusion. The size of  $K_{hm}$  was limited by the minimum grid separation of each mesh. Values used are shown below:

GRID	TIME STEP (minutes)	MINIMUM GRID SPACING (km)	$K_h$ ( $m^2 sec^{-1}$ )
6x6	16	580	$4.44 \times 10^5$
12x12	8	290	$2.22 \times 10^5$
18x12 & 18x12G	4	145	$1.11 \times 10^5$
12x18 & 12x18G			
18x18 & 18x18G			
24x24			
Final graded	0.5	8.26	(see text)

### 5. Data Reduction and Presentation

The following noise or roughness measure was defined:

$$\text{Roughness} = \frac{\sum_{i=2}^N a_i}{a_1}$$

with  $a$  = zonally averaged amplitude from spectral analysis

$i$  = wave number index

$N$  = maximum Fourier wave number (3, 6, or 12)

A measure of damping was used which was the ratio of amplitude of any Fourier component geopotential perturbation to its amplitude at  $t=0$ . This was used to determine the detrimental effects of diffusion on the solutions.

An analytic wave speed was derived from an average propagation speed determined by phase angle changes. The quasi-geostrophic value of the phase speed,  $c$ , is given by

$$c = \bar{U} \frac{(k_x^2 + k_y^2 - \lambda^2)}{(k_x^2 + k_y^2 + \lambda^2)}$$

with

$k_x$  = wave number in x direction

$k_y$  = wave number in y direction

$\lambda^2 = f_o^2 / \phi_o$

$\phi_o$  = mean free surface height

$\bar{U} = 10 \text{ msec}^{-1}$

This formula gives phase speeds of 9.857, 9.958, 9.981, and 9.989 meters per second for wave numbers 1, 2, 3, and 4 respectively.

Graphical plots were produced for all tests. Those not discussed as part of the results are presented in Figures 35 through 54 inclusive. The results for the entire length of the cyclically connected channel were not plotted. Each plot extends to within one regular grid increment of the boundary where the mesh is connected. The maps of  $\phi$  and  $u$  have the domain mean removed. The nodal points are marked with small crosses.

#### B. SINUSOIDAL RESULTS

The effects of diagonal slant can be seen in Figures 10 and 11. The most noticeable difference exists in Figure 10 where the mirror image effect of diagonal bias shows itself in the latitudinal direction. The cases shown possessing an alternating slant form a rough average between the opposite slant cases. Figure 11, which shows the  $\phi$  amplitude, gives a slight hint of bias effects, but the tendencies are less pronounced. Wave speed data for similar cases on the 24x24 grid were not obtained, but one would expect less bias as the element size approaches zero. A plot of wave number one's amplitude versus latitude for the 12x12 mesh showed no significant variation for the three different diagonalization methods, so apparently the effect does diminish with finer resolution.

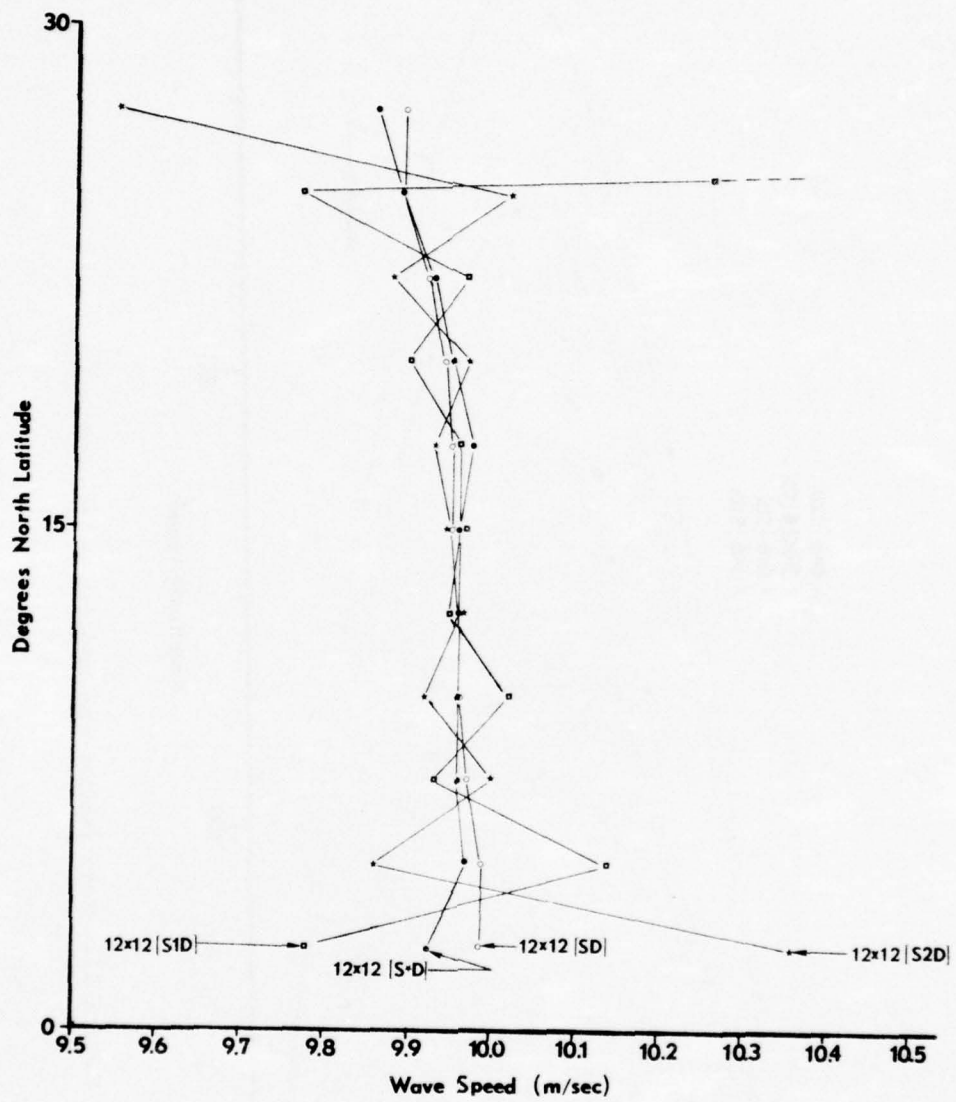


Figure 10. Latitudinal variation of wave speed (48 hour time averaged) for four grids.

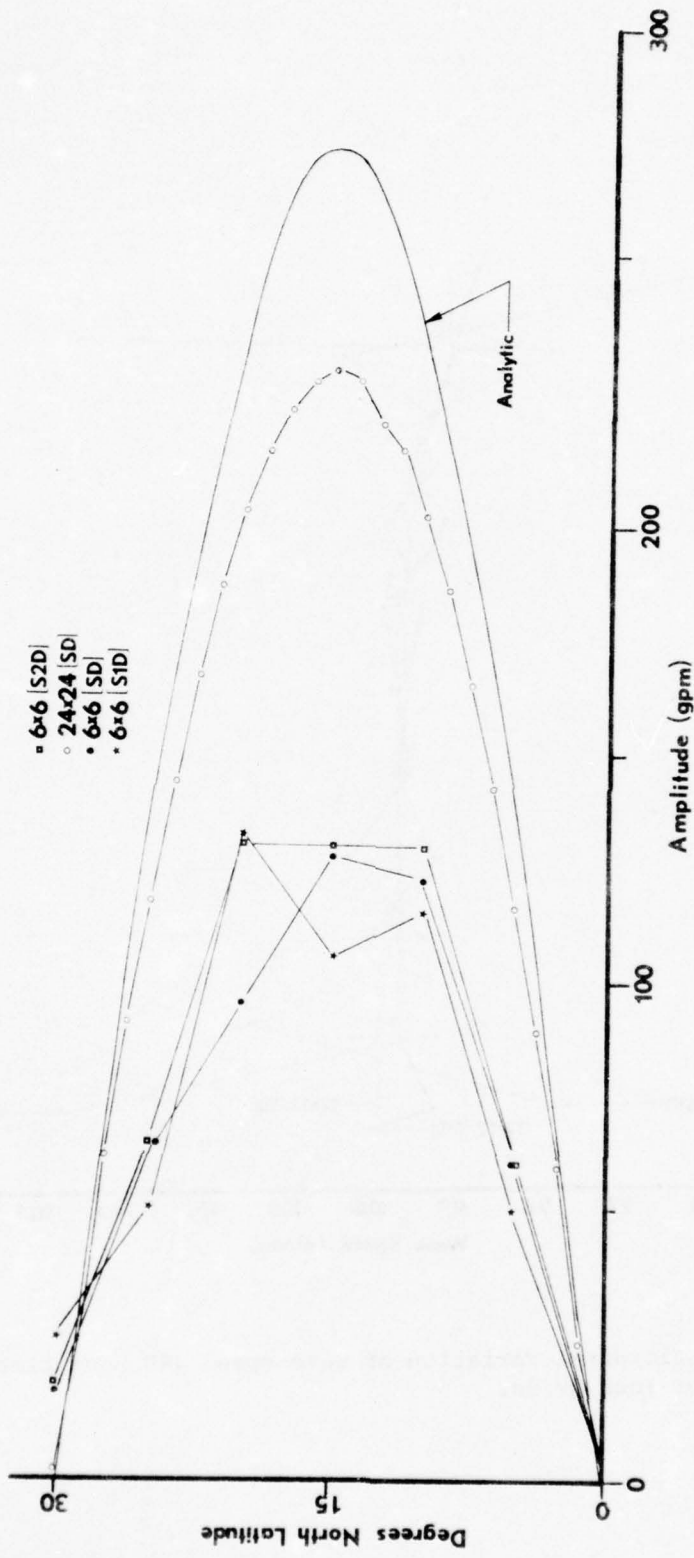


Figure 11. Wave number one amplitude at t=48 hours.

The latitudinal variation of phase propagation of various grids is shown in Figure 12. In general all phase speeds are greater than analytic, but not significantly so. It should be noted that the scale of the abscissa in Figure 12 covers a very narrow range of phase speeds; even the coarsest grid is within four per cent of the true phase speed. The phase velocities depart most from analytic near the boundaries, where the amplitude is small. A somewhat anomalous result is the better treatment of propagation by the 12x12 as opposed to the 24x24 mesh. This is most apparent below the mid-channel latitude. No explanation is offered for this condition.

The necessity of some spatial smoothing is apparent when one compares Figures 13 and 14; Figures 15 and 16; Figures 17 and 18; and Figures 19 and 20. Even if it were not for this unwanted noise, large phase errors result without smoothing, as Figure 21 suggests. Even by decreasing the initial disturbance amplitude by a factor of five, the phase errors are almost identical with unsmoothed tests.

The fine, course, and intermediate resolution grid results are shown for their roughness properties in Figure 22. Even with four times the damping, the 6x6 mesh cannot compete with the 24x24 mesh in this comparison. The 6x6 results become even less desirable when one sees that the wave amplitude is cut more than in half (Figure 23). An enlarged view of Figure 22 is presented in Figure 24. This diagram should show if any significant improvement can be gained by using a grid which is intermediate between the 12x12 and 24x24 mesh, thus increasing accuracy with less computational sacrifices. It should be noted that all these intermediate grids possess one half the diffusion of the 12x12 mesh. Apparently two of the grids tried do offer the desired quality, the 12x18

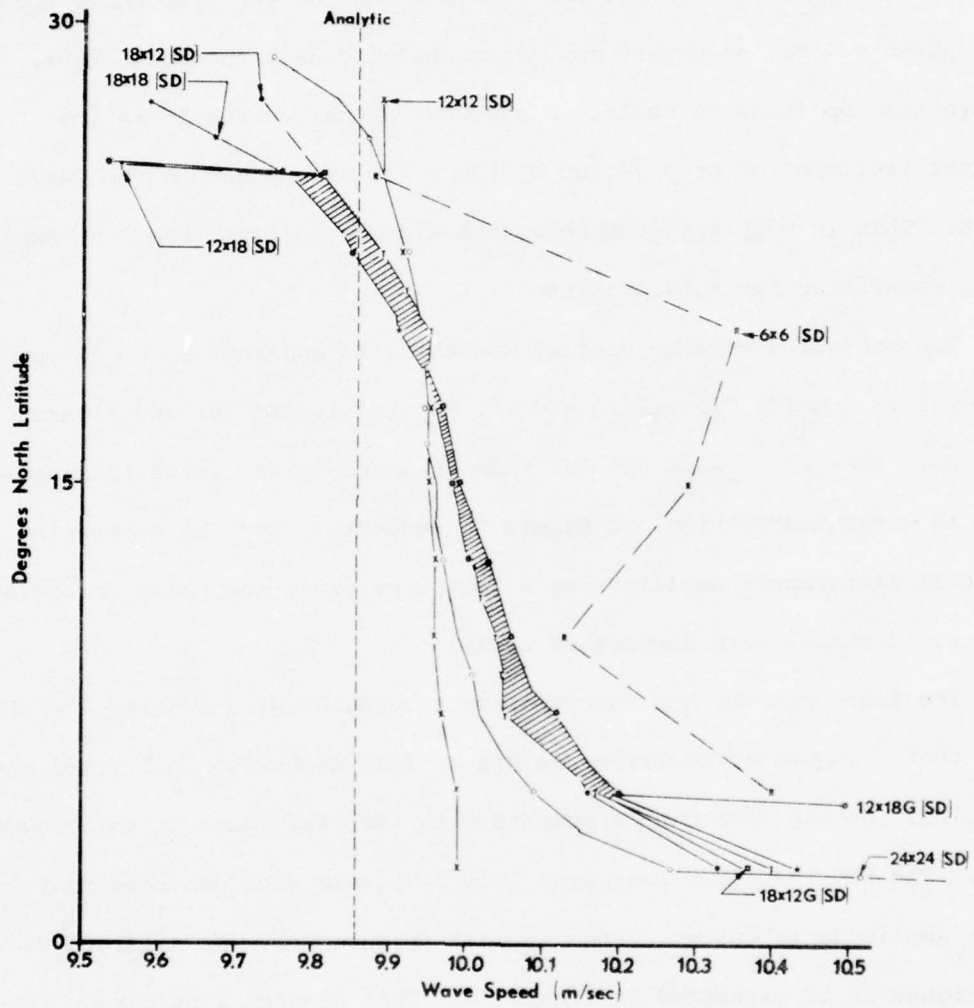
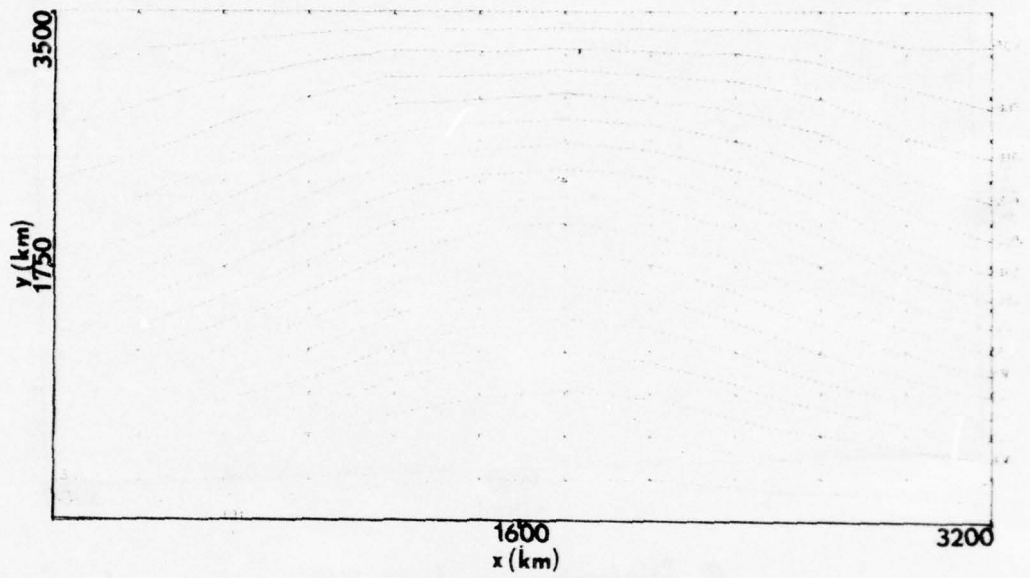
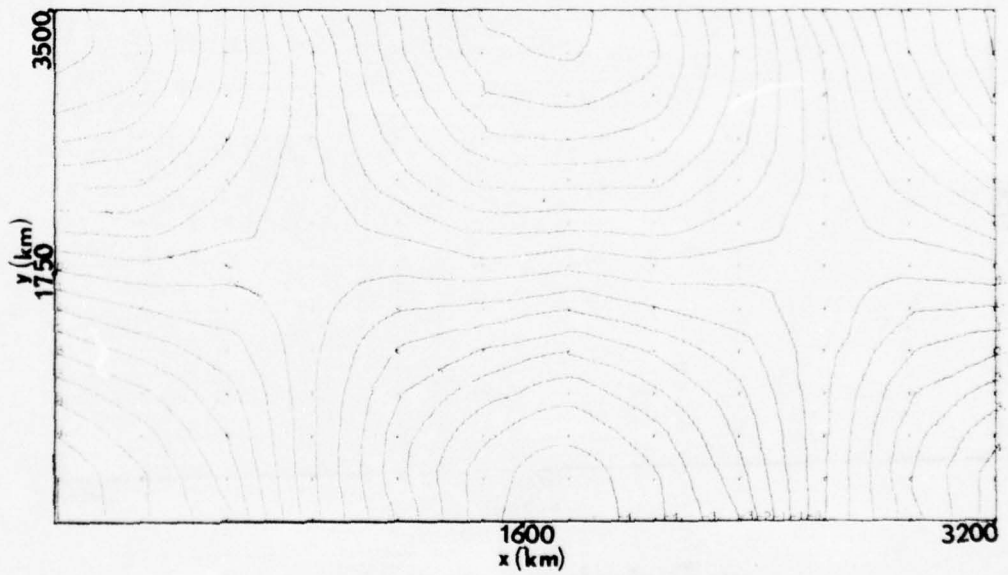


Figure 12. Latitudinal variation of wave speed (48 hour time averaged).

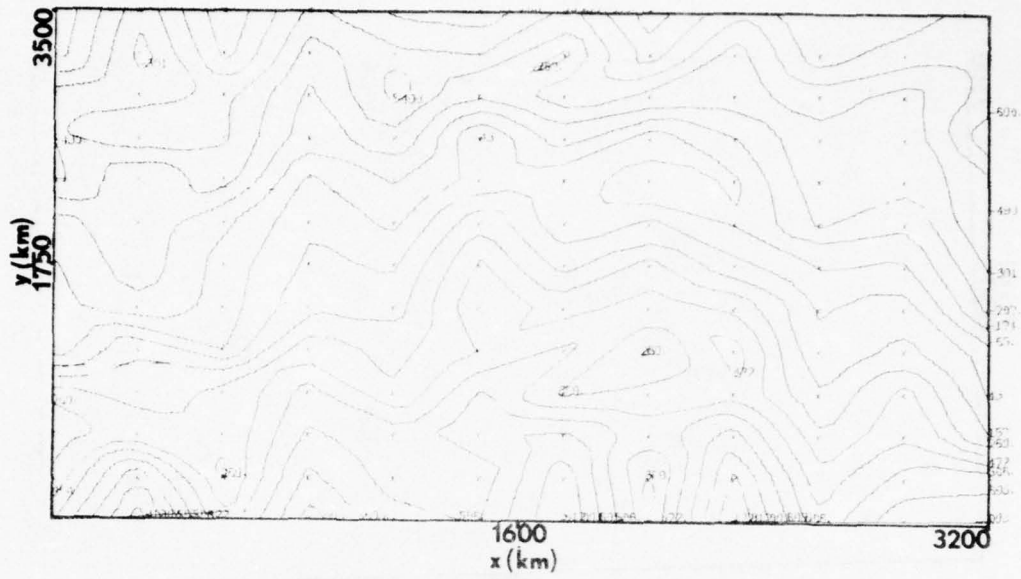


$\Phi$  Disturbance (gpm)

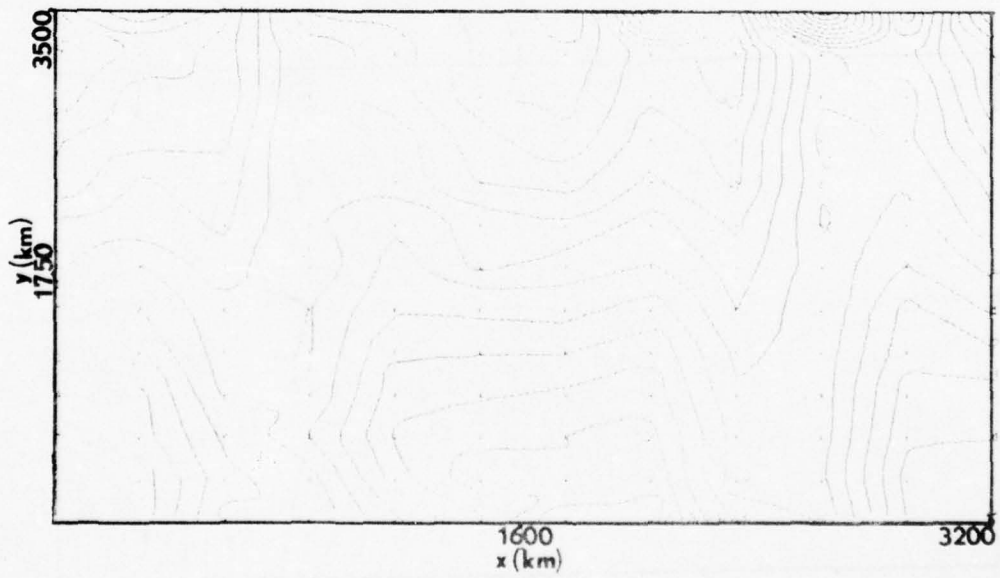


$u$  Disturbance (m/sec)

Figure 13. 12x12 [SD] at  $t=48$  hours.

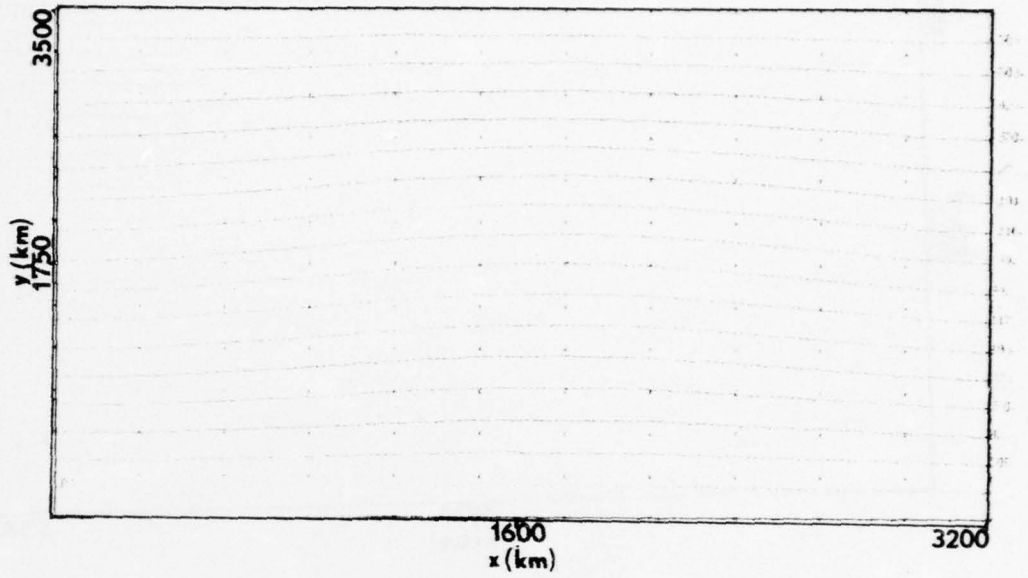


$\Phi$  Disturbance (gpm)

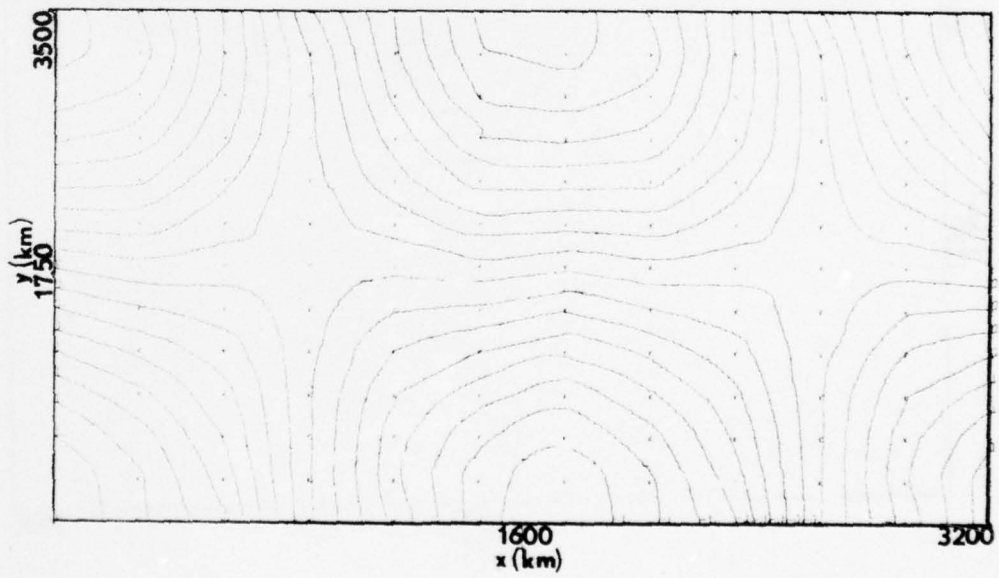


$u$  Disturbance (m/sec)

Figure 14. 12x12 [SND] at t=48 hours.

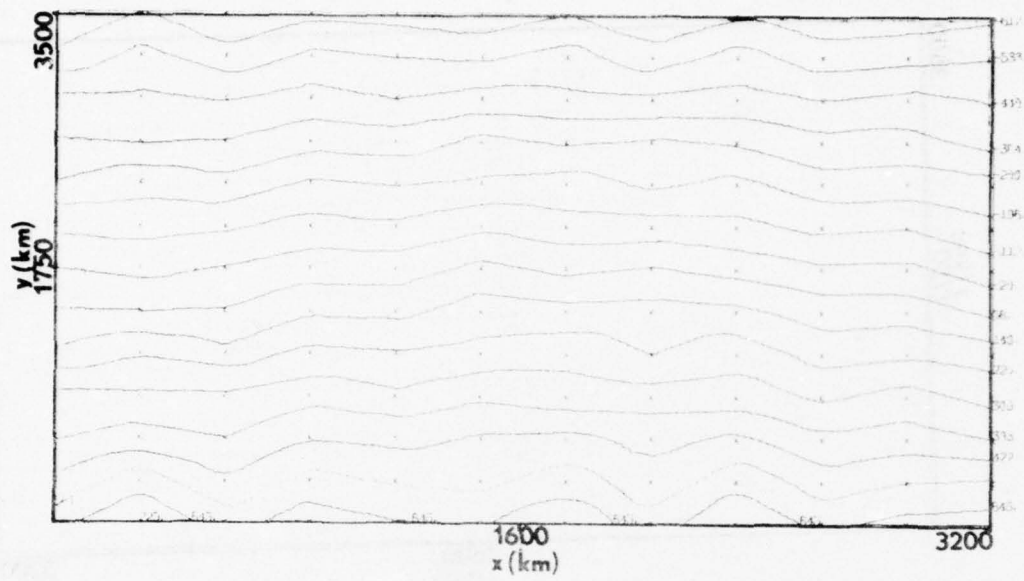


$\phi$  Disturbance (gpm)

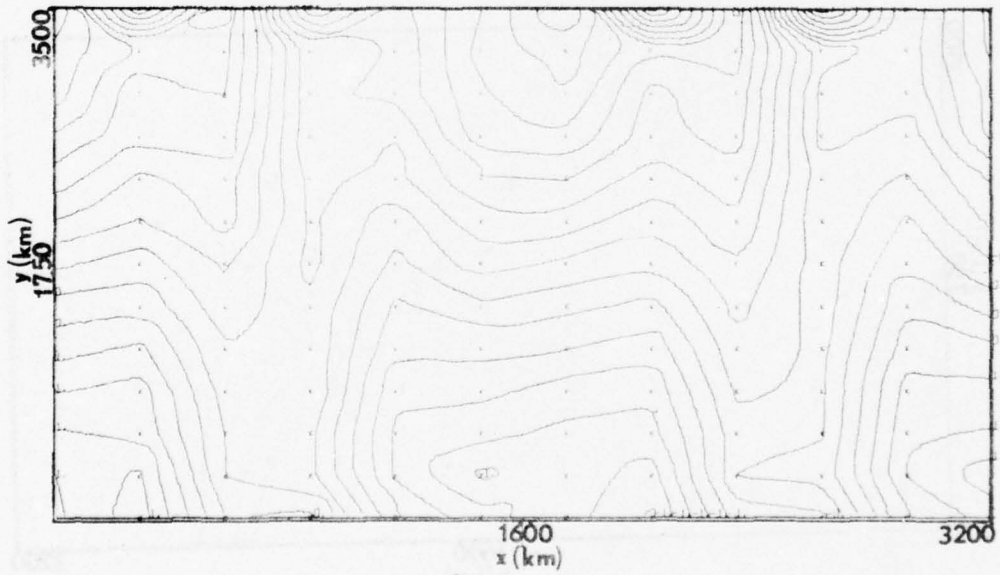


$u$  Disturbance (m/sec)

Figure 15.  $12 \times 12$  [S\*D] at  $t=48$  hours.

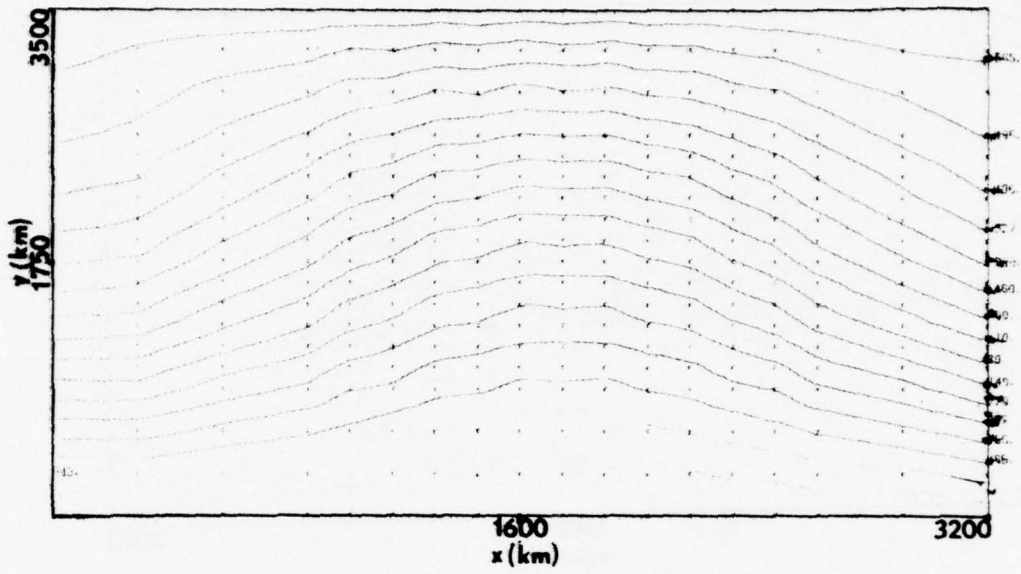


$\Phi$  Disturbance (gpm)

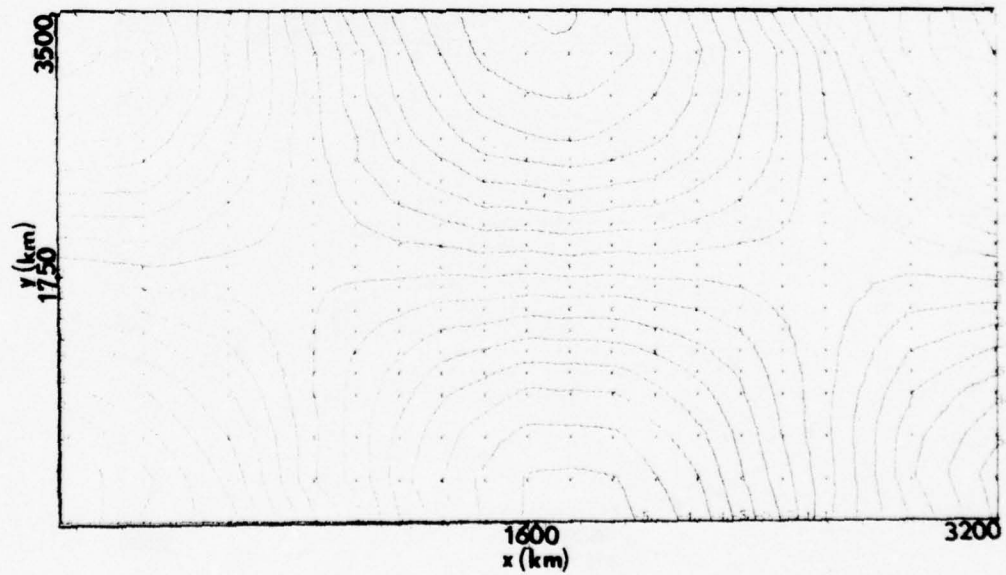


$u$  Disturbance (m/sec)

Figure 16. 12x12 [S\*ND] at  $t=48$  hours.

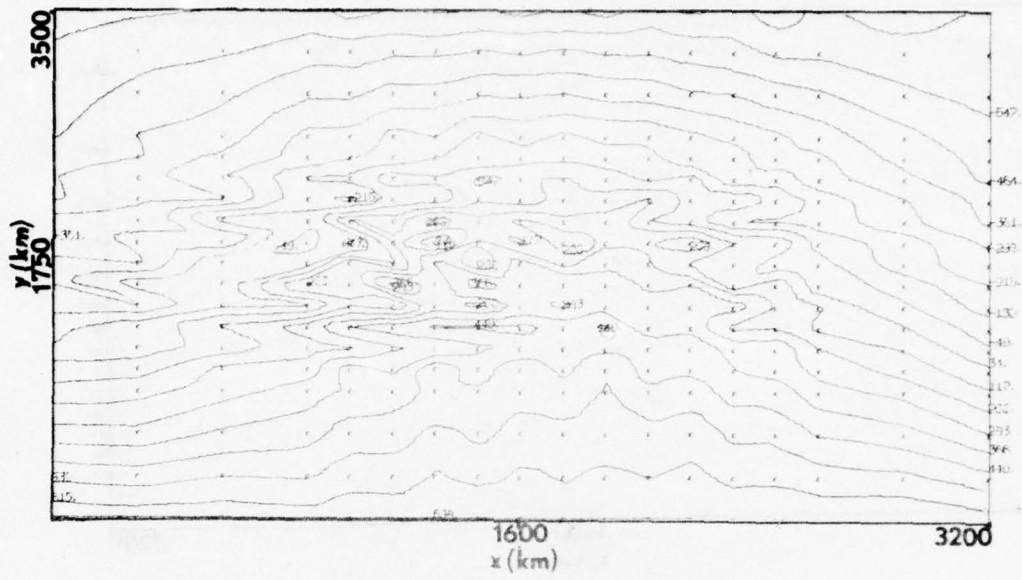


$\phi$  Disturbance (gpm)

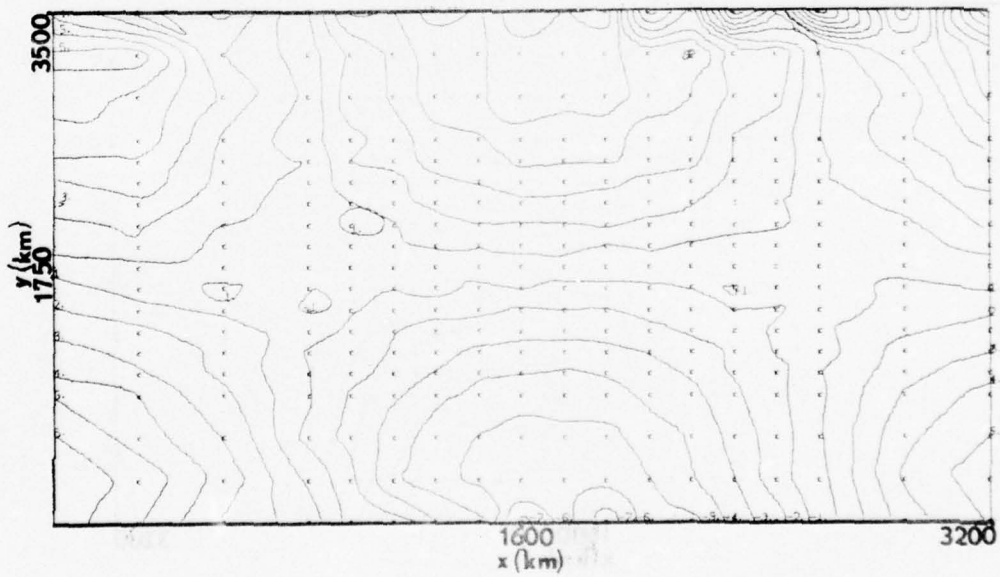


$u$  Disturbance (m/sec)

Figure 17. 18x18 [SD] at  $t=48$  hours.

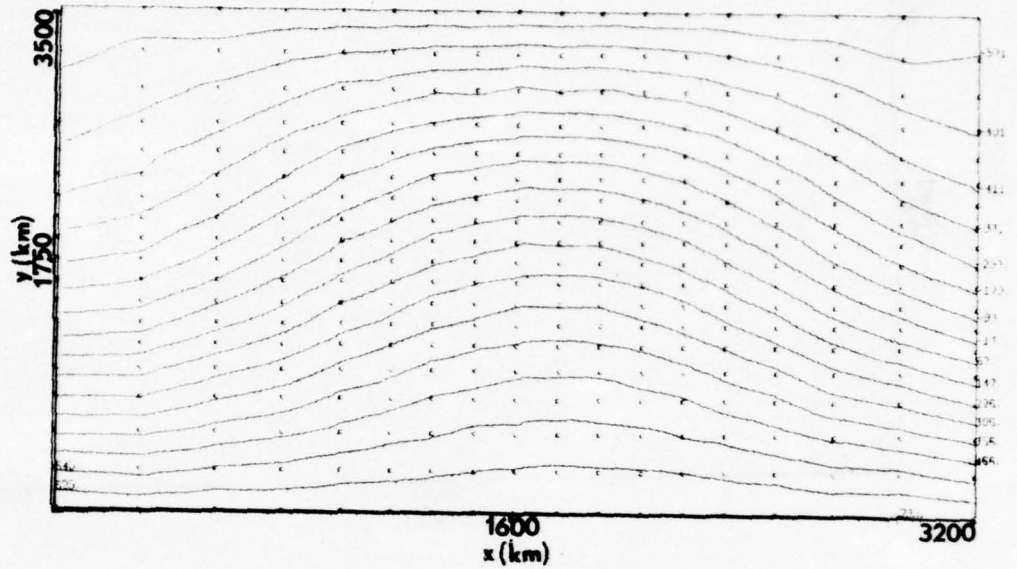


$\Phi$  Disturbance (gpm)

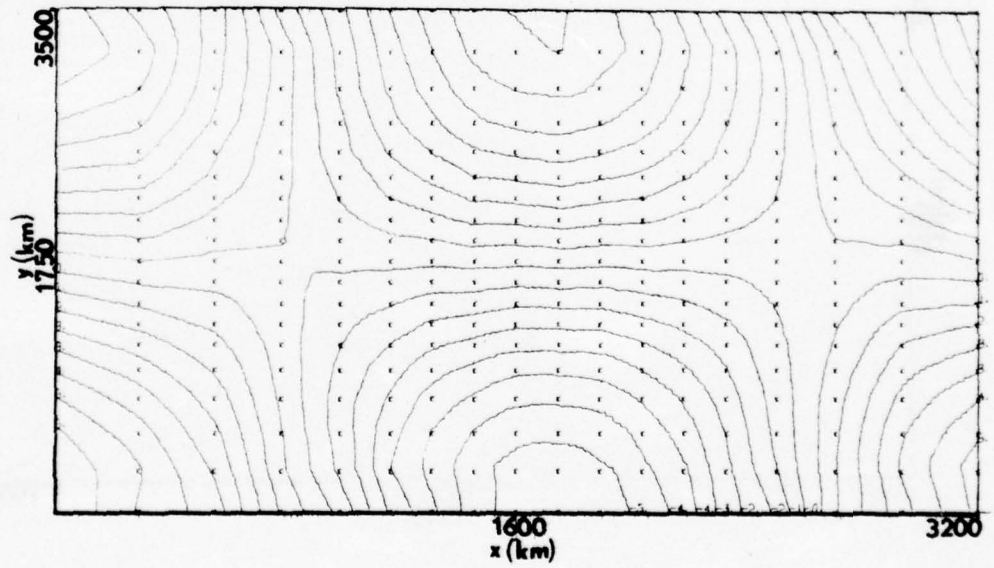


u Disturbance (m/sec)

Figure 18. 18x18 [SND] at t=48 hours.

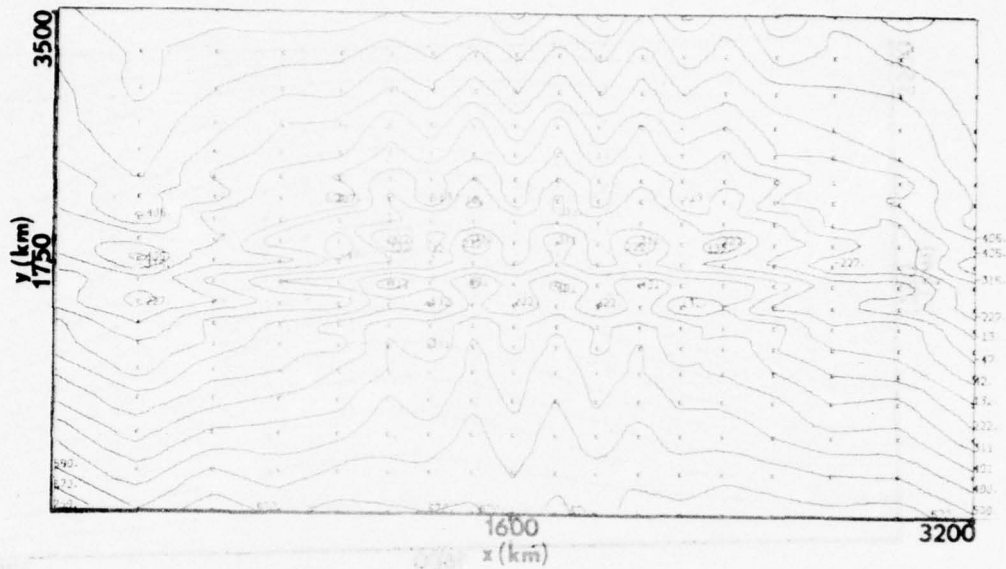


$\Phi$  Disturbance (gpm)

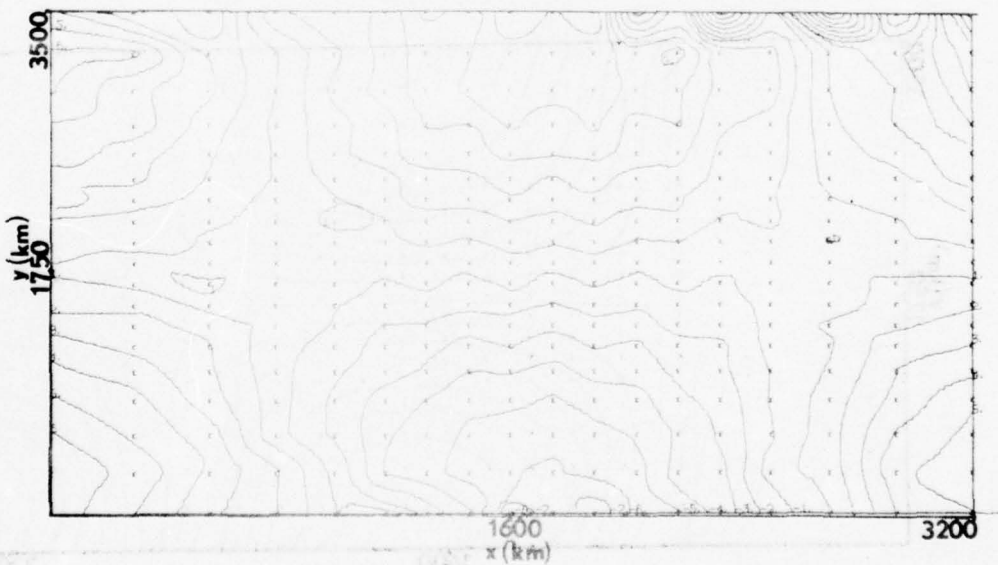


$u$  Disturbance (m/sec)

Figure 19. 18x18G [SD] at  $t=48$  hours.



$\Phi$  Disturbance (gpm)



$u$  Disturbance (m/sec)

Figure 20. 18x18G [SND] at t=48 hours.

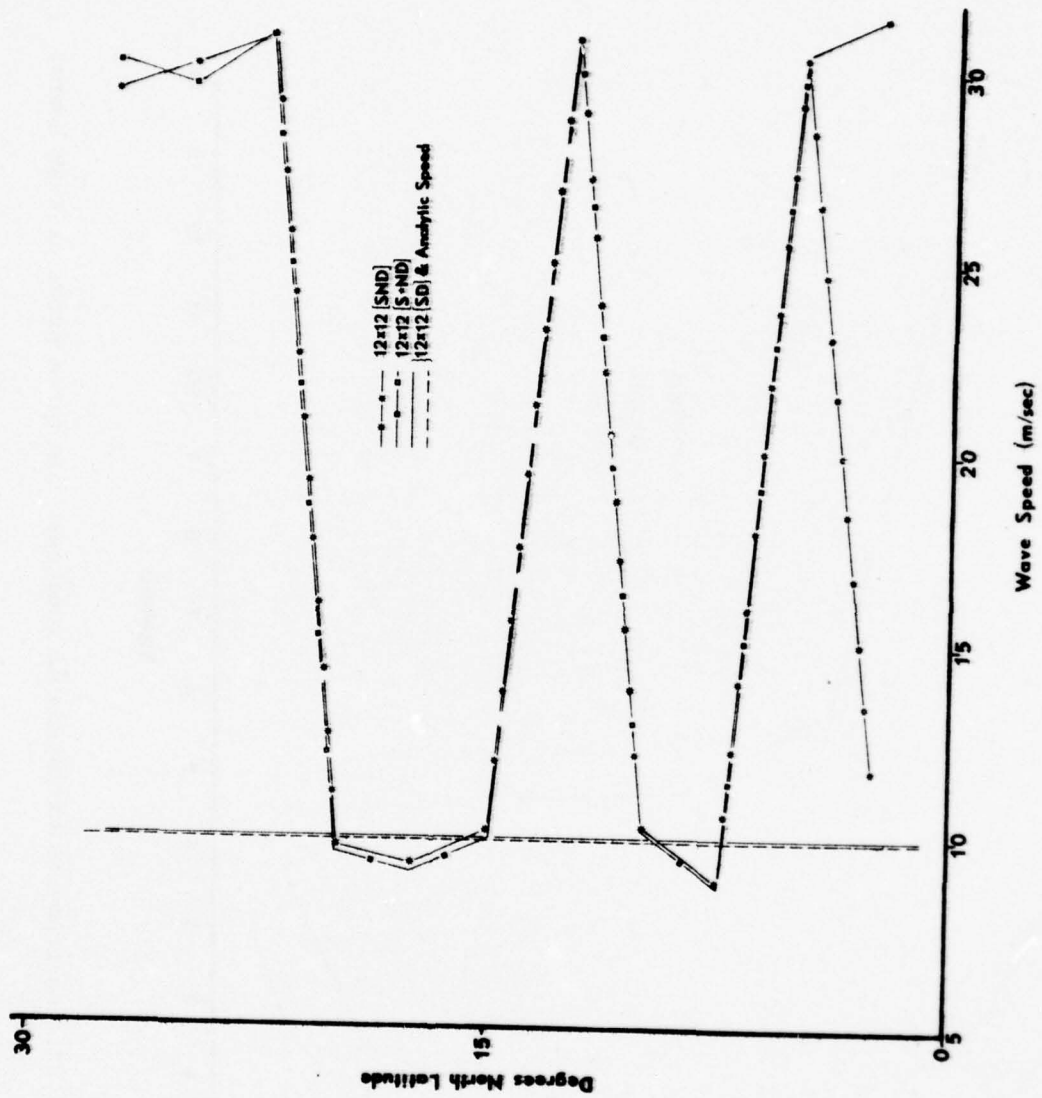


Figure 21. Latitudinal variation of wave speed (48 hour time averaged) with no diffusion.

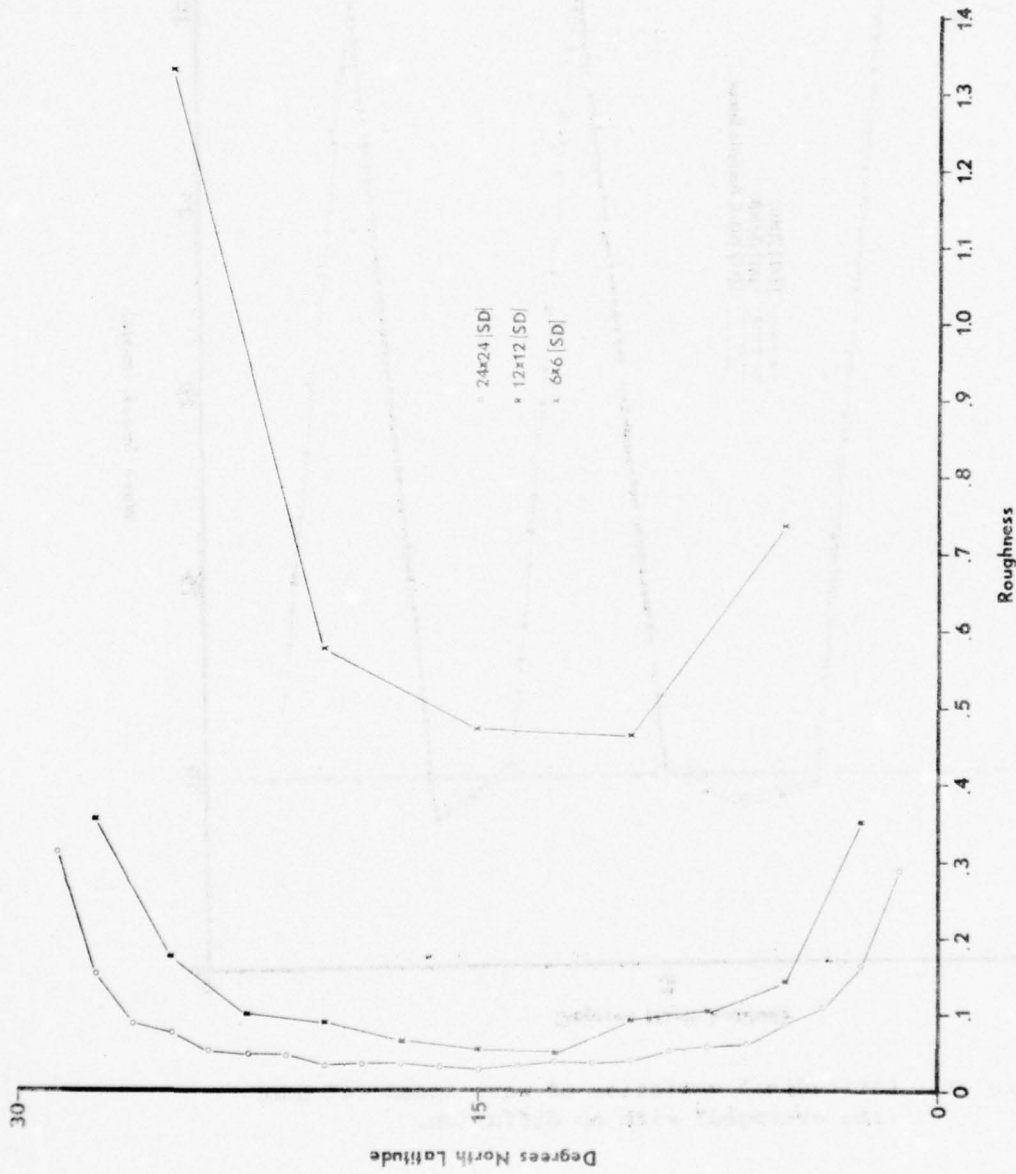


Figure 22. Latitudinal variation of roughness for three grids at t=48 hours.

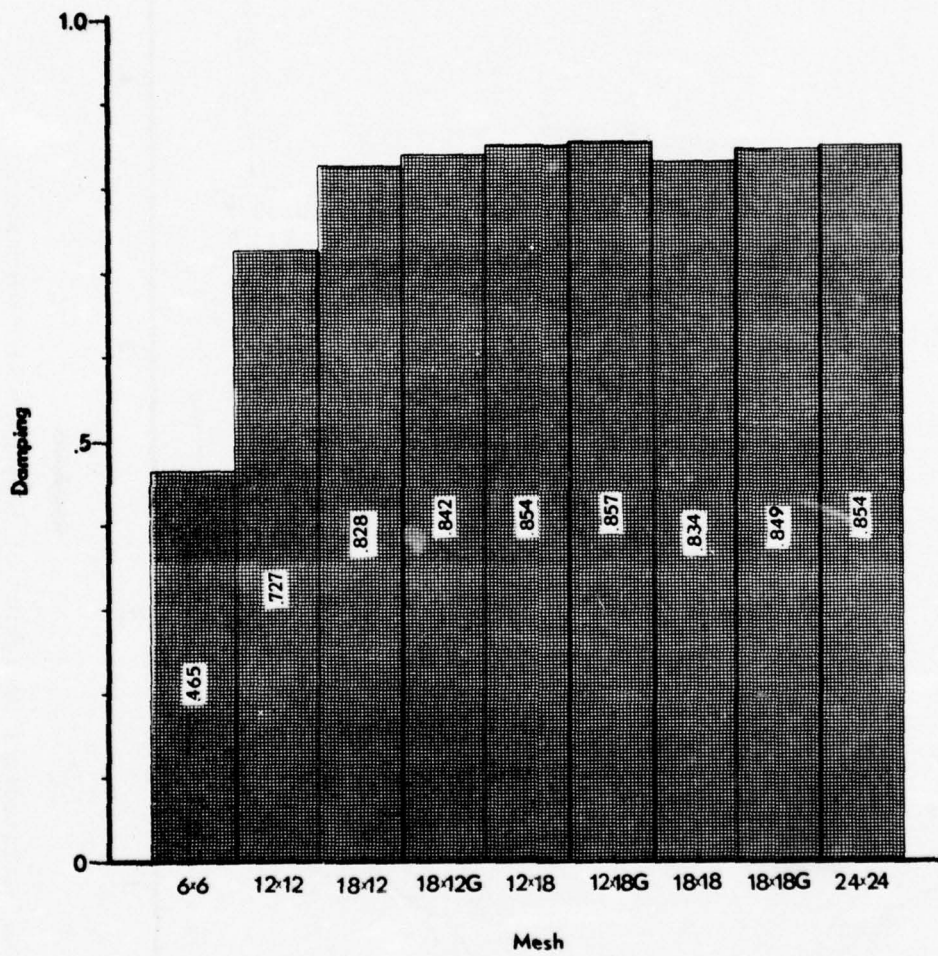


Figure 23. Damping characteristics of various grids at t=48 hours.

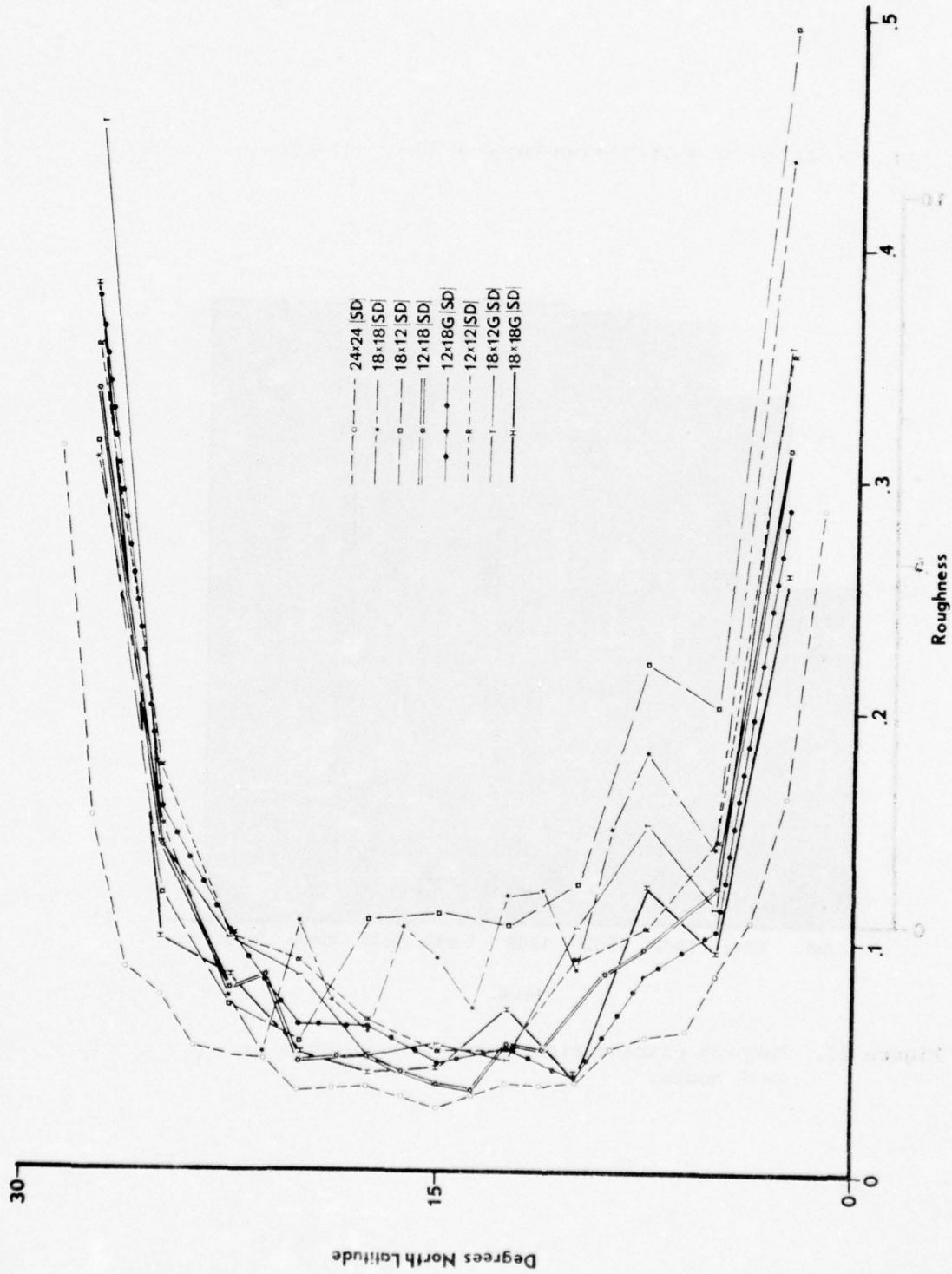


Figure 24. Latitudinal variation of roughness at t=48 hours.

and 12x18G meshes. Both of these meshes have better resolution over the region where the disturbance is strongest. It was hoped that the grid with a graded rather than abrupt change in the  $y$  direction would be better. However, it appears the graded version (12x18G) is only better at latitudes south of 15 North. The 18x12 and 18x12G meshes are generally worse than the 12x12 counterpart although the 18x12G is the better of the two. This perhaps is the result of the disturbance being advected across this graded or abruptly changing region of the two grids. One would, however, hope that the 18x12G would show better noise properties than the 12x12. It is plausible that the element size change is still too abrupt to describe the scale of motion used with an advecting velocity. The remaining two cases to be identified are the 18x18 and 18x18G. The 18x18 case shows an oscillating effect proceeding northward. This could be explained as some pseudo-boundary influence induced by the abrupt element size change. The 18x18G handles the situation somewhat more effectively. The oscillation is still present, slightly reduced, but the roughness is significantly less than the 18x18 case and is better than the 12x12 case at most latitudes.

The spectral distribution of wave energy at 48 hours is shown in Figure 25. Some grids had disturbance amplitudes of less than  $1 \text{ m}^2 \text{ sec}^{-2}$  (gpm) and therefore don't appear on this logarithmic plot. As expected, the 24x24 has the least tendency for energy transferral to higher wave numbers. Of interest is the large amount of energy exchanged by the 18x12 grid. It has the largest energy levels in all higher wave numbers save wave number four, where its smoothly graded companion (12x18G) is slightly higher. Relating the two 18x18 grids, one can see an expected improvement when a graded version of the same grid is used; a useful feature which is not as evident at latitudes different from 15.

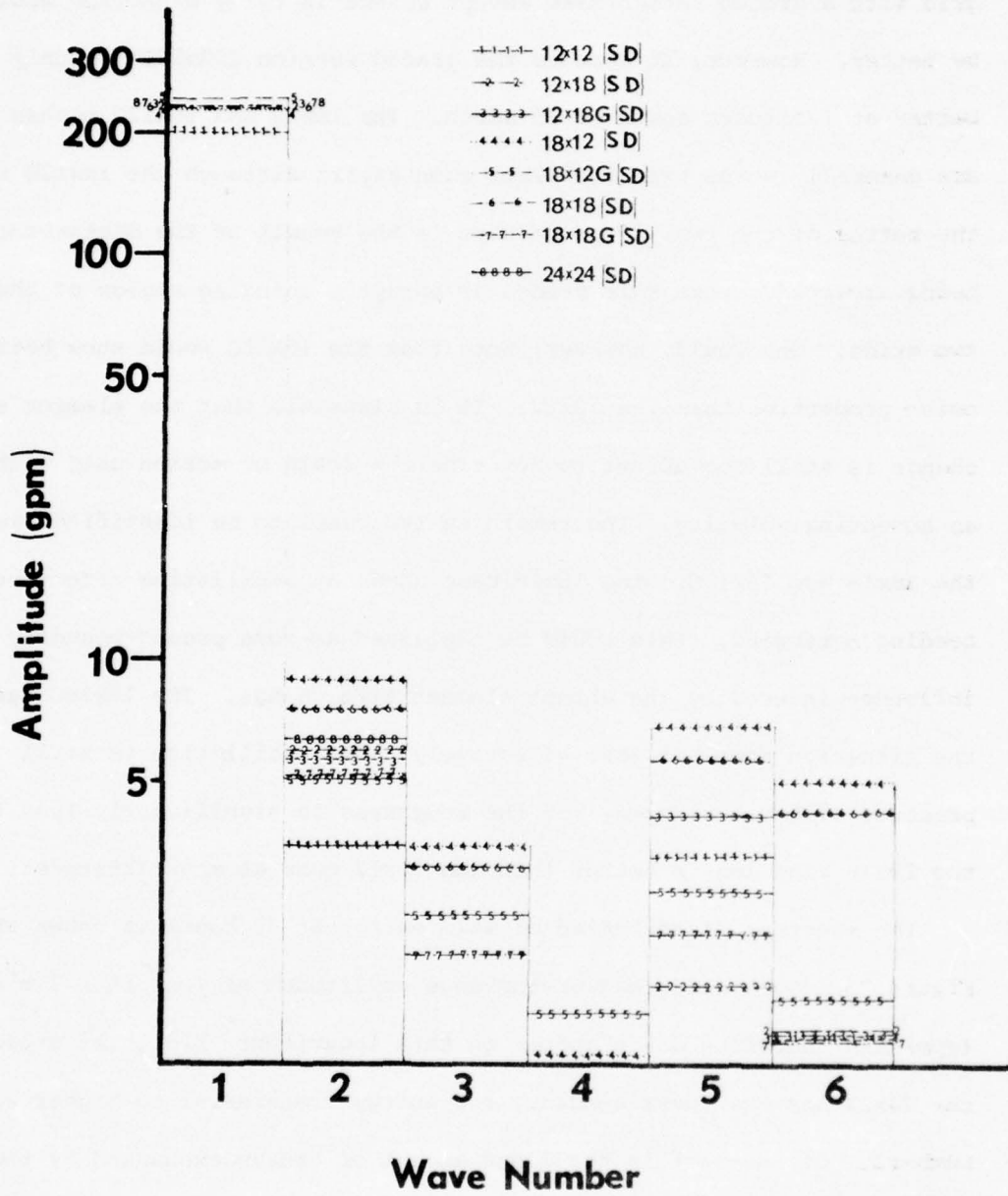


Figure 25. Spectral characteristics with sinusoidal conditions at t=48 hours.

As an interesting sidelight, consider Figure 26. The gravity wave fluctuations due to slight imbalances are indicated on this diagram. The free surface gravity waves allowed in this case have an analytic period of 4.4 hours calculated for a wave length equal to that of the channel. This agrees well with the short period fluctuations shown in wave speed.

#### C. VORTEX RESULTS

The gravity wave influence on geopotential height variations is also implied in Figure 27. The diffusion is also evident as the stationary vortex fills through 48 hours. The gravity wave amplitude in this case is larger initially than with the sinusoidal case because of the larger truncation errors in representing the initial state. Rapid filling occurs in the first 18 hours due to diffusion.

Again diffusion is necessary. To verify this compare Figures 28 and 29. The undesirable requirement of significant diffusion at 500 mb is obvious, but in the vortex cases the diffusion imposed significantly damps the disturbance. Further experiments should verify if the scheme could survive with less diffusion of the type used.

Figure 30 shows a view of damping for grids other than the 6x6 and 24x24. Eighty eight per cent of the original mid-latitude perturbation is contained in waves one through three, so these should be of primary concern. All grids in this figure except the 12x12 have identical damping coefficients and therefore should treat up to wave number three similarly. This is the case except both 12x18 grids don't damp wave number three as much. Since this Laplace type filter is not very wave number selective, one would expect higher diffusion of longer waves.

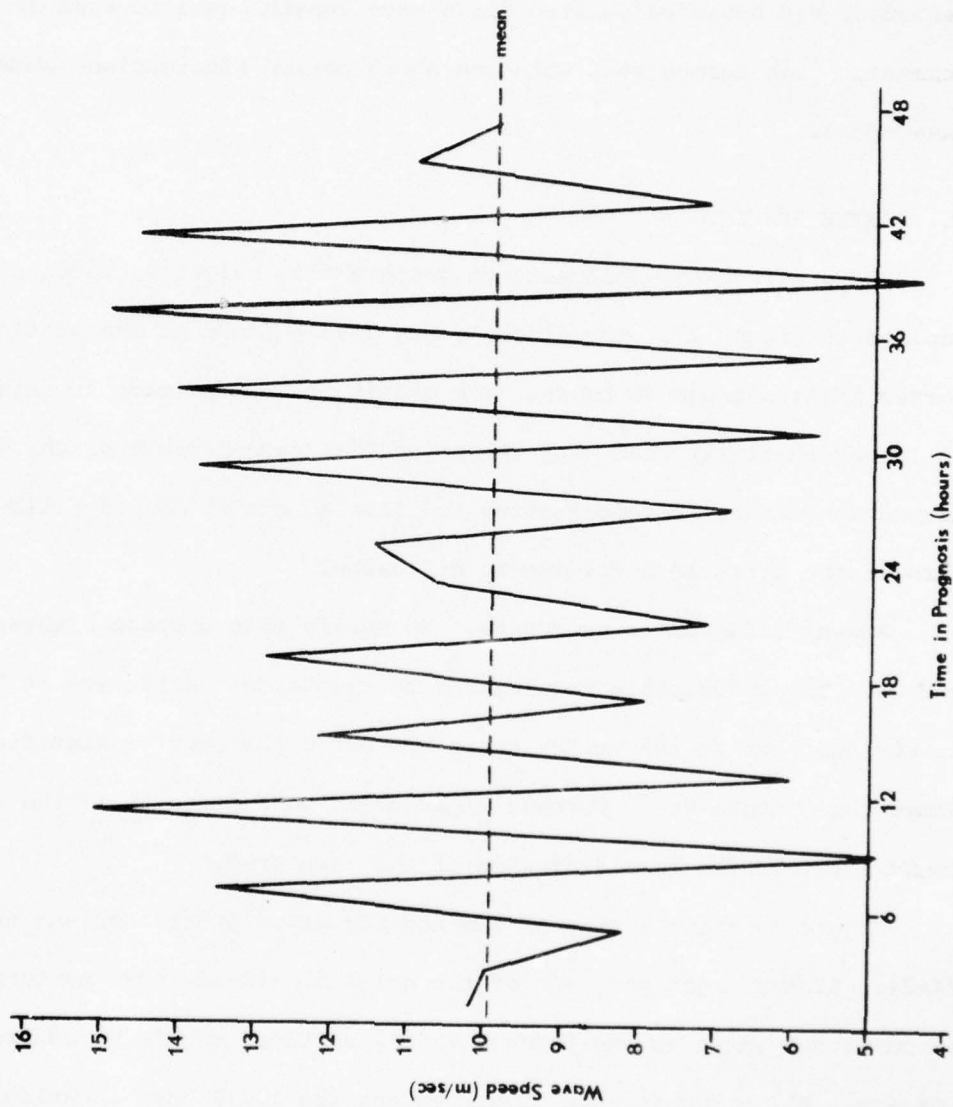


Figure 26. Temporal wave speed fluctuations.

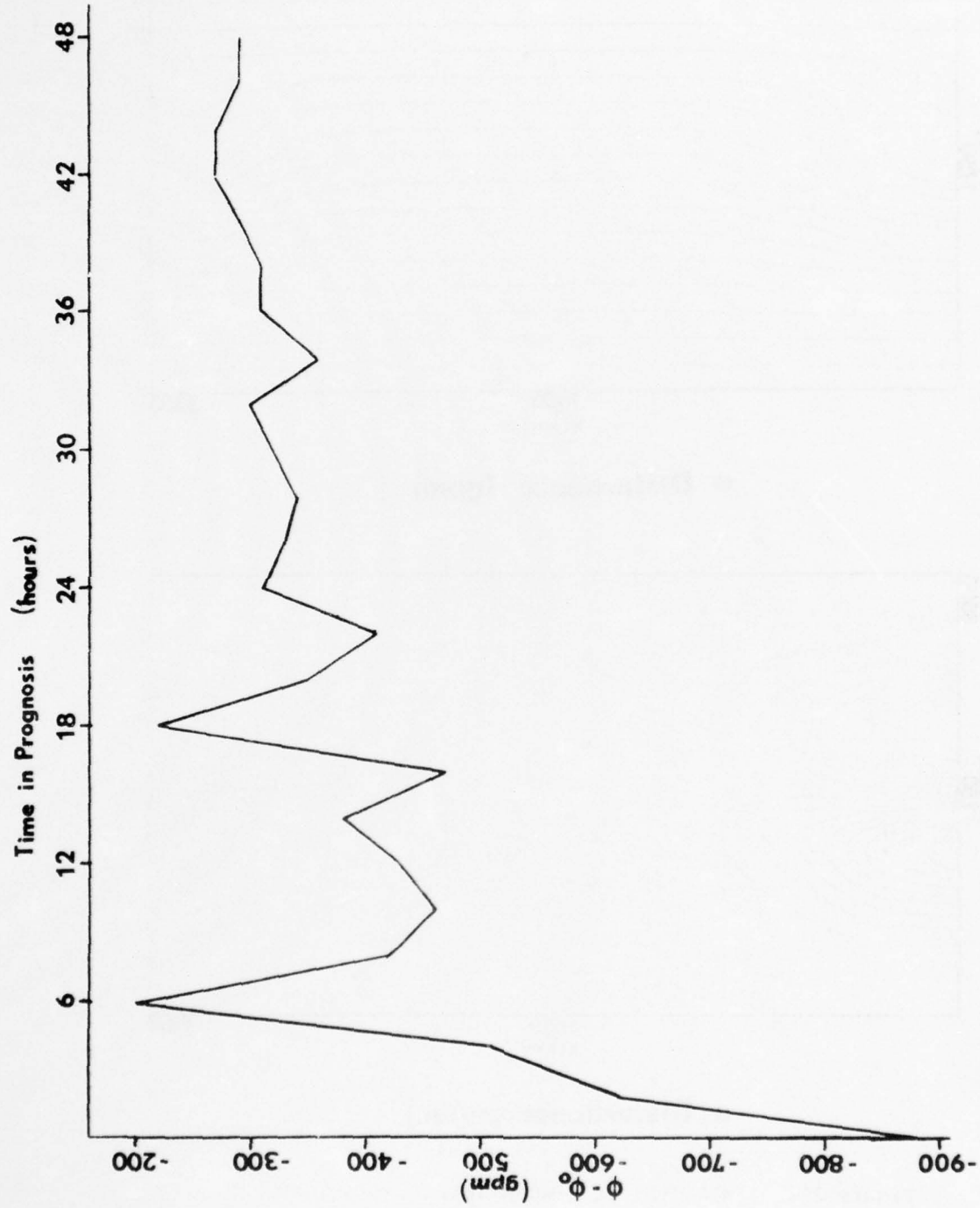
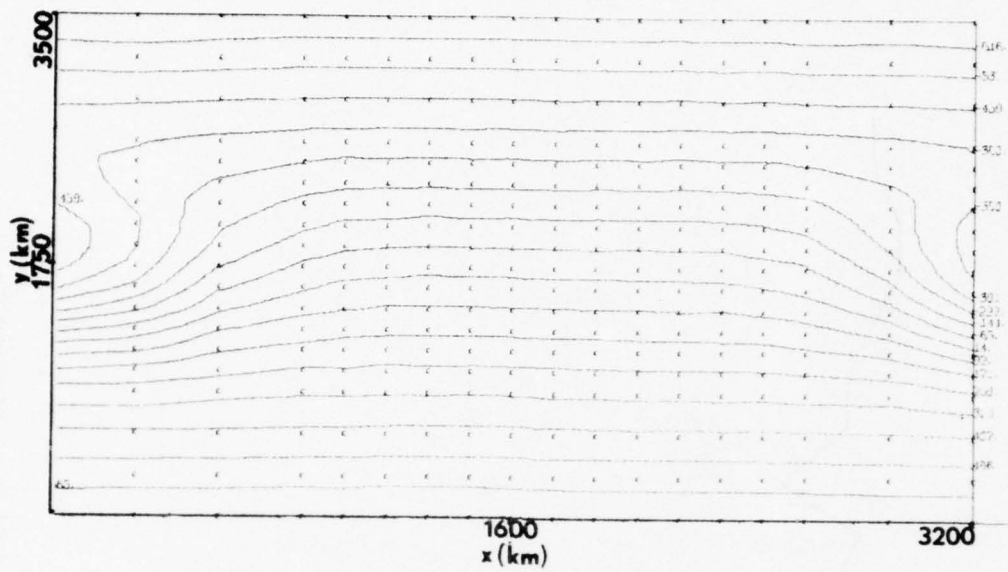
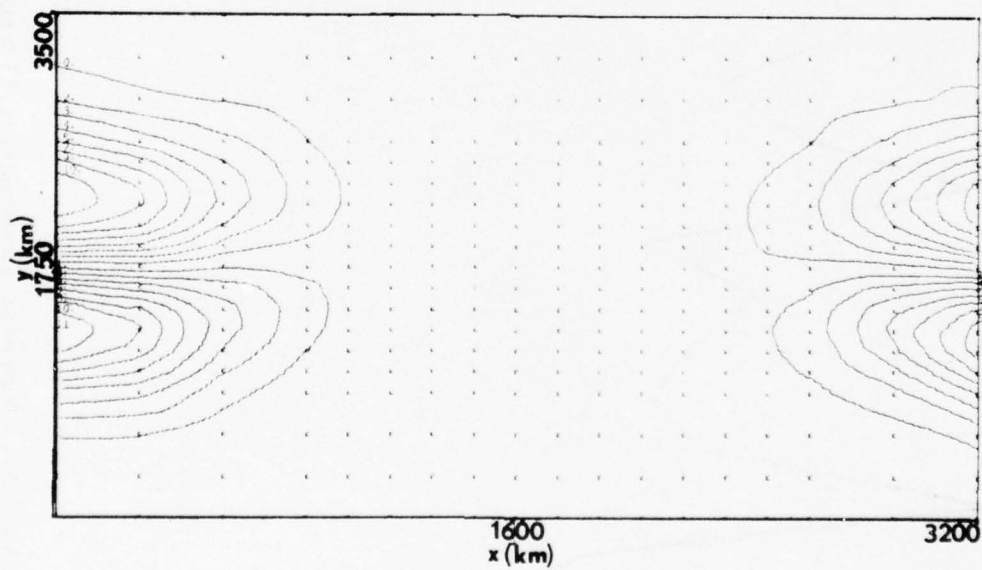


Figure 27. Temporal geopotential fluctuations at center of stationary vortex.

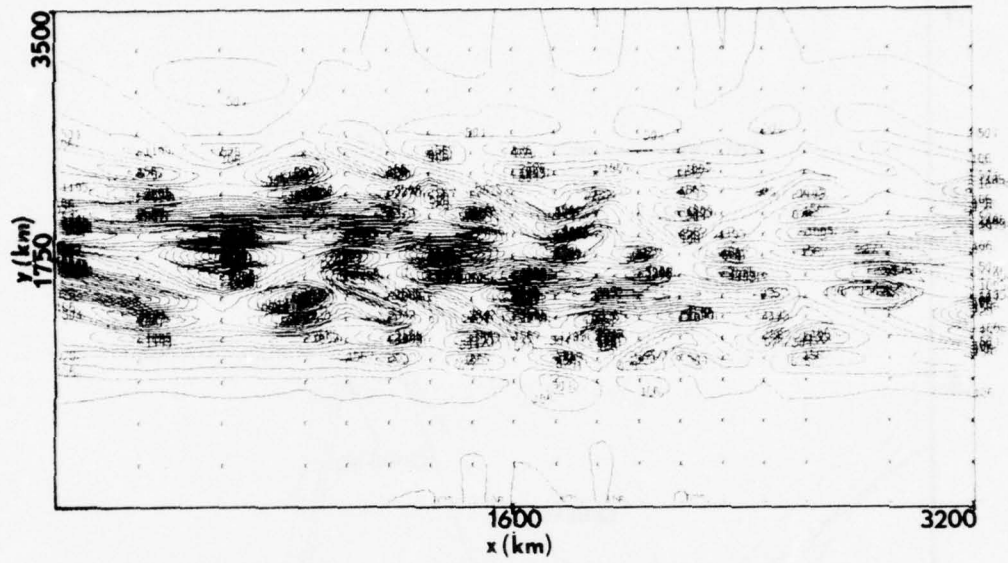


$\Phi$  Disturbance (gpm)

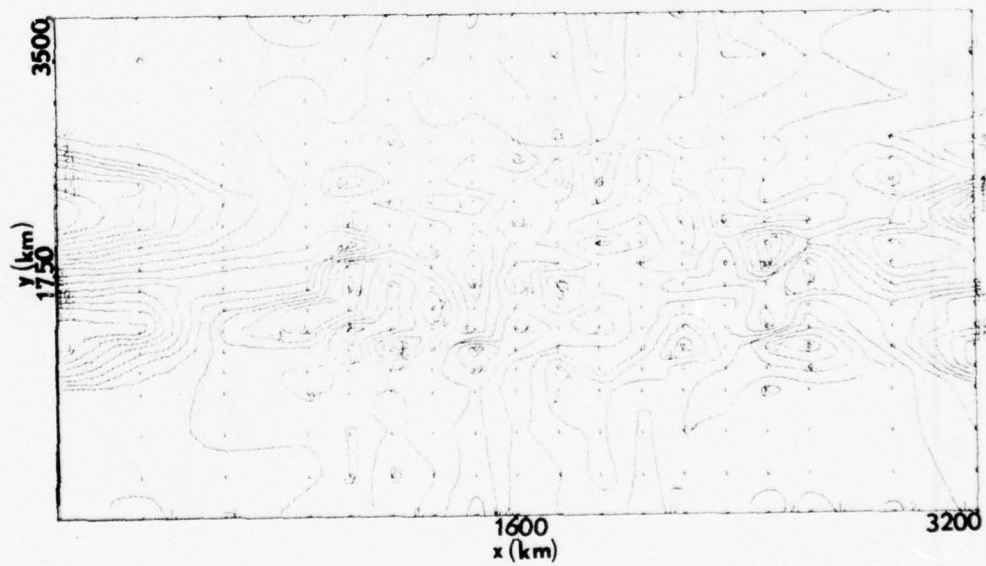


$u$  Disturbance (m/sec)

Figure 28. 18x18 [VD] at  $t=48$  hours.



$\phi$  Disturbance (gpm)



$u$  Disturbance (m/sec)

Figure 29. 18x18 [VND] at t=48 hours.

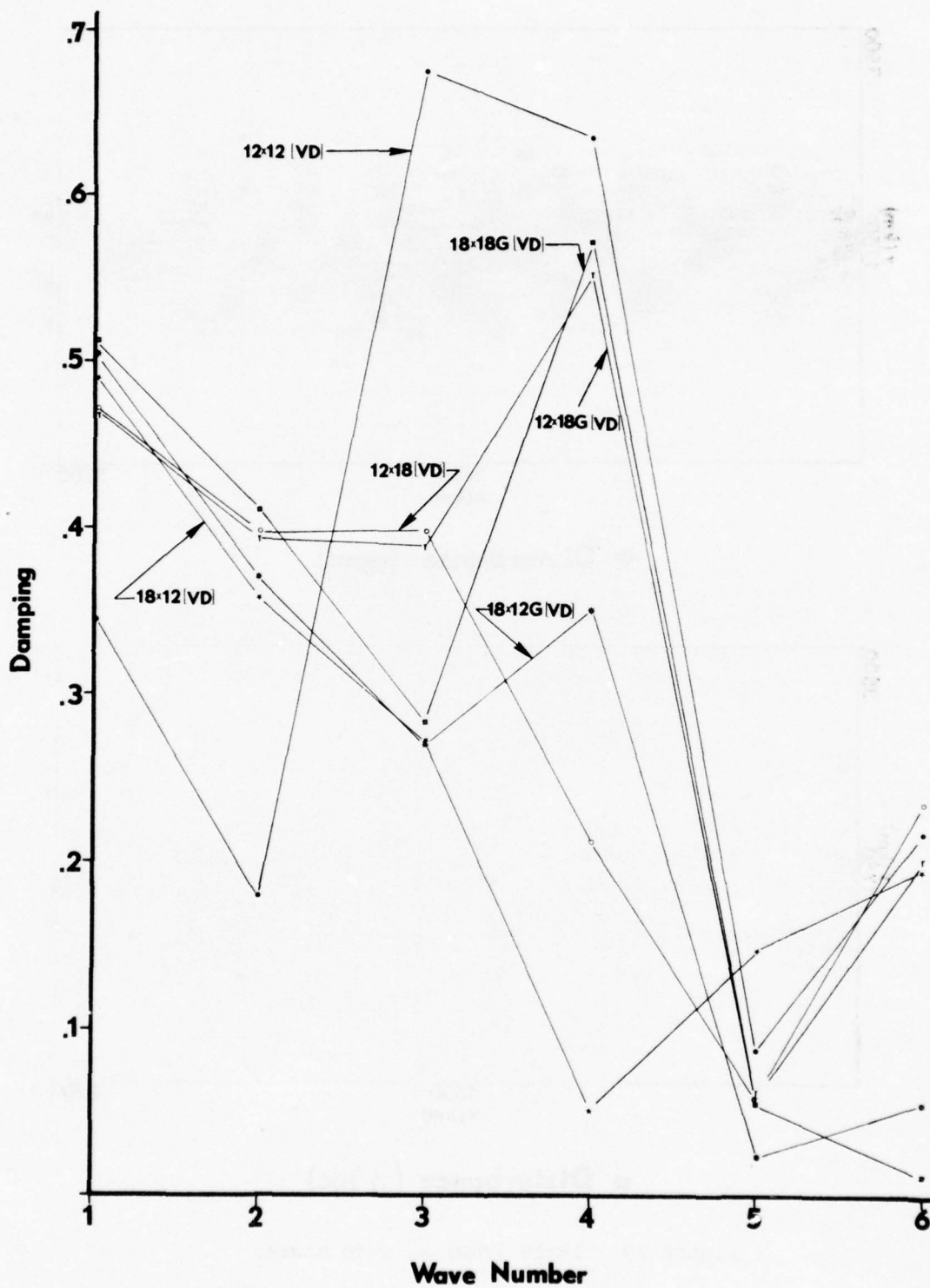


Figure 30. Damping characteristics with vortex at t=48 hours.

It appears that both 12x18 meshes are not consistent with this assumption. Both damp wave number three about the same as two but treat wave numbers four and five in opposite senses. The 12x18G grid also shows the same tendency as the 12x18 though it damps wave number three more. The 18x12 and 18x12G grids also show similar treatment of waves four and five. The large damping of wave five relative to four can be explained in part by the fact five's initial amplitude is about two and one half times that of four. The large damping of wave two by the 12x12 mesh is a serious defect of the required amount of coarse grid diffusion. The actual spectral results of these grids are shown in Figure 31.

Figures 32 and 33 show the final distributions of amplitude for waves one and two, respectively. The large damping may make it hard to distinguish between results for grids with greater resolution than the 12x12. If this is but a secondary effect then one could say that extending the entire domain resolution to that of the 24x24 is not necessary.

A comparison of mid channel wave speeds shows all grids studied give very accurate results for wave numbers one and two. Phase propagation of wave number three is handled poorly by the 12x12 grid and is 270% in error for the 12x12 case and 70% in error for the 18x12 cases. All grids but the 24x24 are grossly in error for wave number four; at best 175% error (18x18 grids) and at worst 240% error for the 18x12G case. The 24x24 case is 25% in error for wave number four. All per cent errors mentioned are over estimates by the grids in wave speed. Phase prediction accuracy rapidly deteriorates for higher wave numbers. Propagation errors for large time integrations are contaminated by artificial noise being filtered to higher wave numbers.

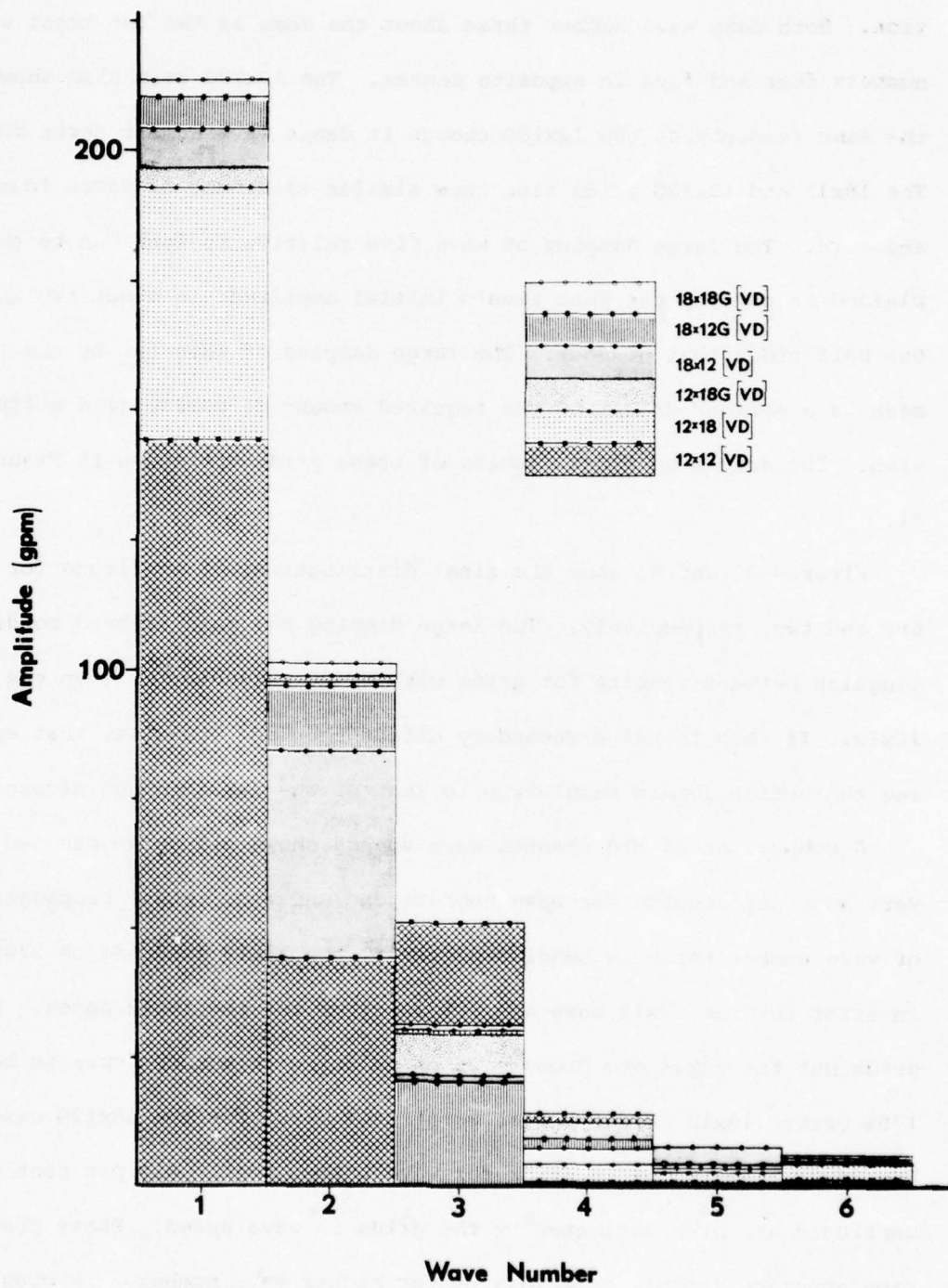


Figure 31. Spectral characteristics with vortex conditions at t=48 hours.

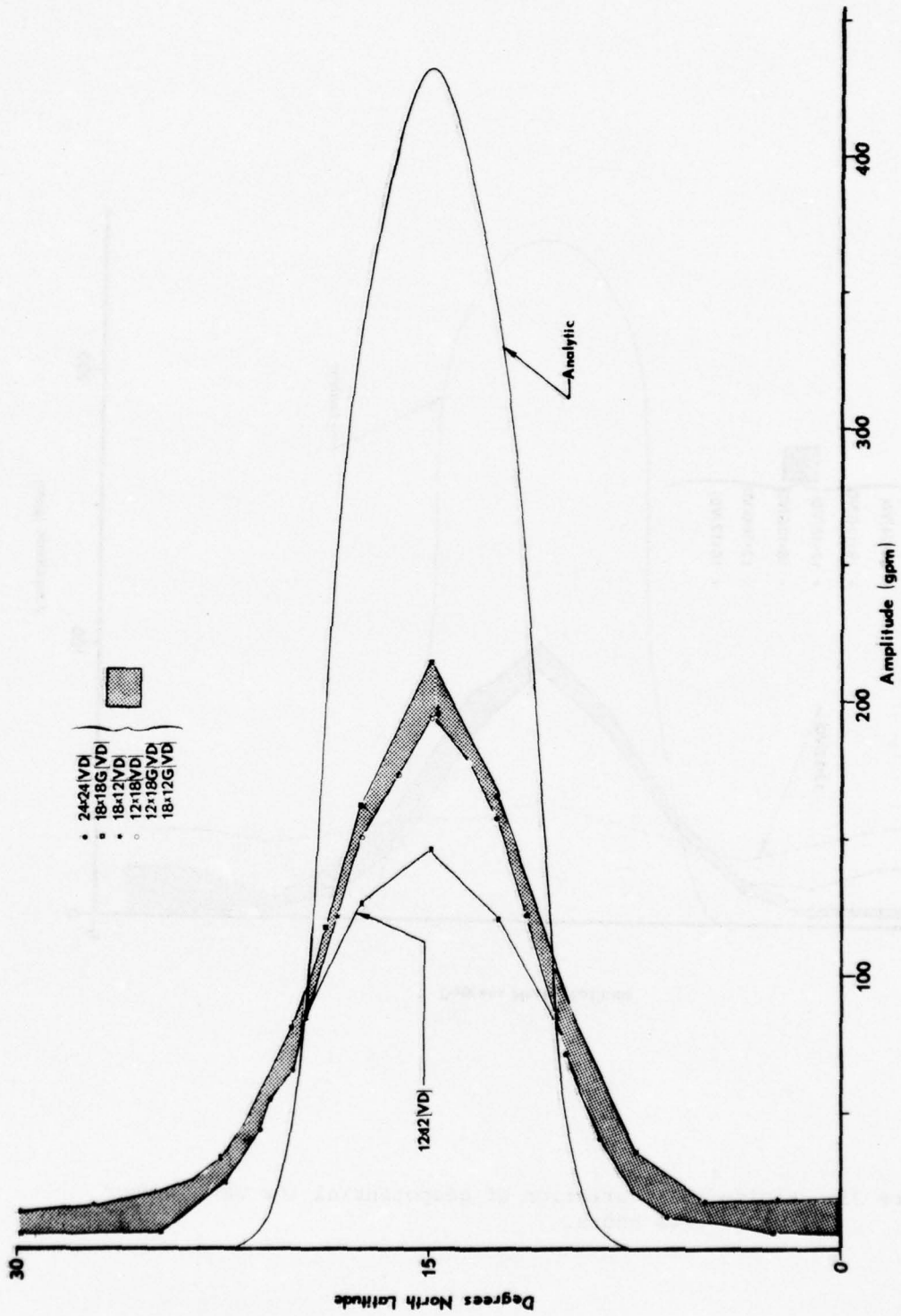


Figure 32. Latitudinal variation of geopotential for wave number one at  $t=48$  hours.

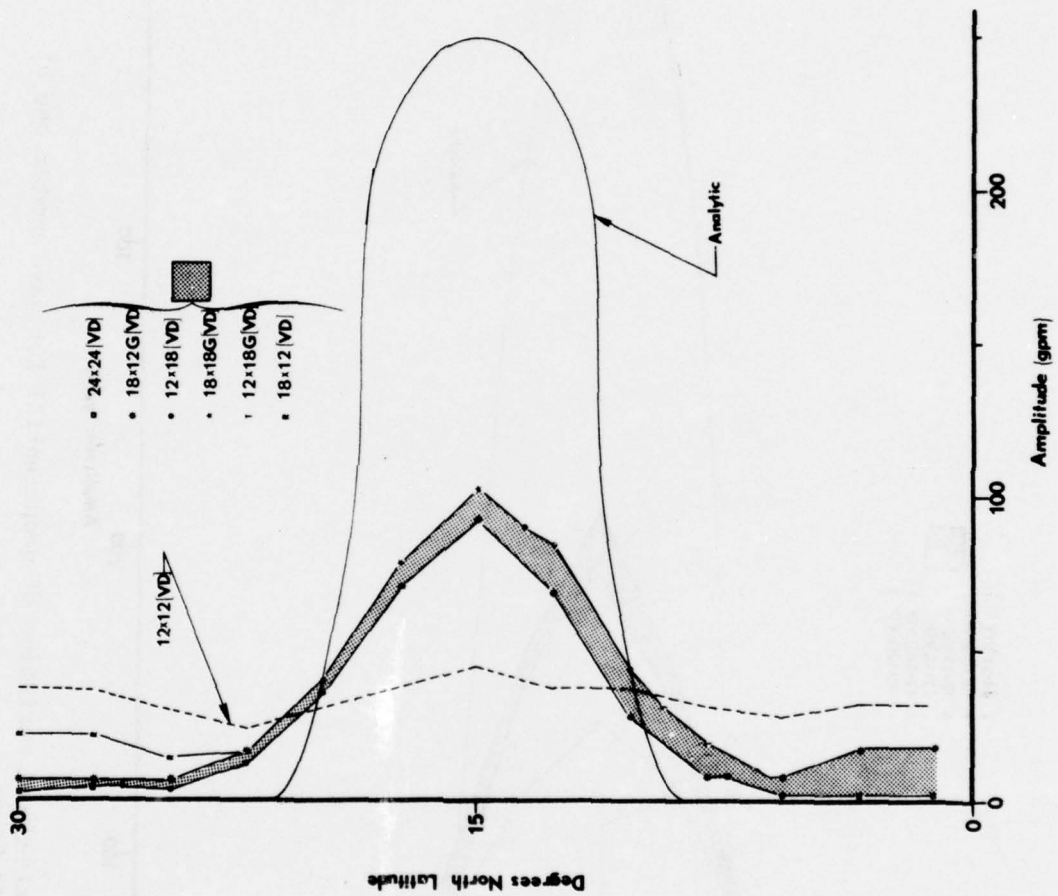


Figure 33. Latitudinal variation of geopotential for wave number two at  $t=48$  hours.

Studies with the highly variable grid shown in Figure 6 were curtailed. It was therefore not possible to fully investigate the movement of the grid with the vortex. A few experiments were carried out using both the vortex and single harmonic wave. The experiments with simpler initial conditions are not presented. A study was made of the vortex with no mean flow. The results of this investigation are shown in Figure 34.

Basic tests were done with a constant  $K_h$  over the domain. The value for this coefficient was again selected based on the smallest grid increment. On this grid, this value was very small, so small in fact that another formulation of diffusion was required.

A more involved diffusion formulation was tried which assumed a diffusion coefficient constant over each element. A vector type diffusion was then applied. Simply stated, the diffusion over an element was derived using:

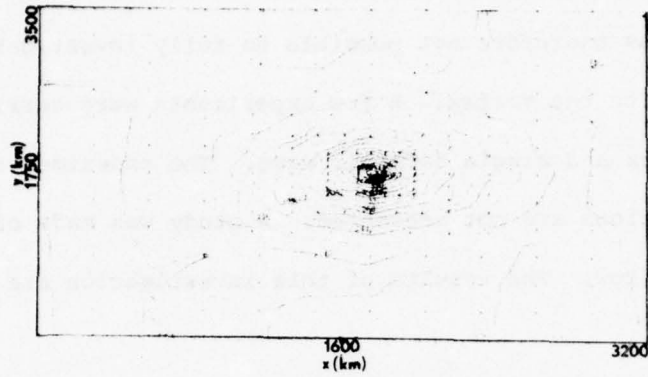
$$K_{he} = .01 \frac{A_e}{A_l} K_{hm}$$

with:  $K_{he}$  = diffusion on an element, e

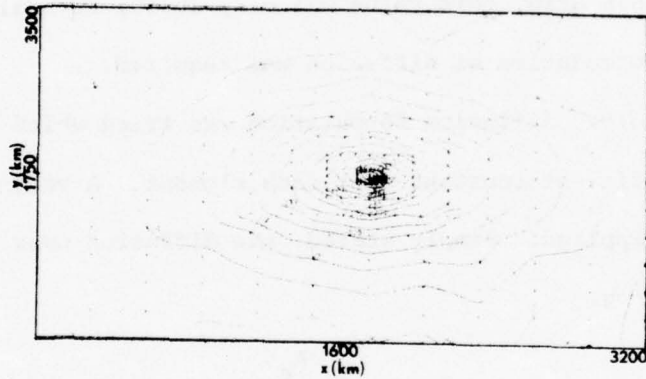
A = area of element e or element l

$K_{hm}$  = diffusion coefficient based on minimum grid spacing, associated with elements 1 through 24 (elements surrounding the nodal point in the center of diagram Figure 6).

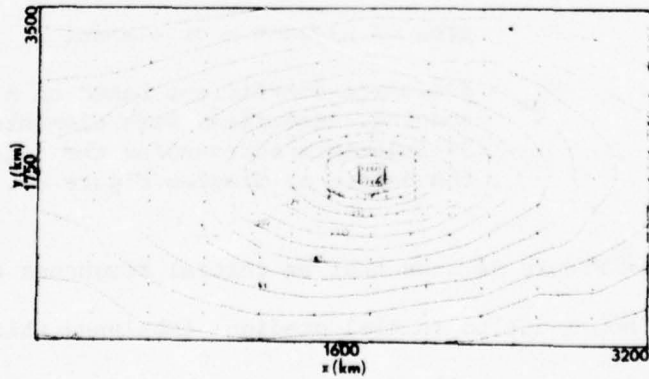
The plots in Figure 34 show that an initial roughness developed evident at six hours due to initial gradient imbalance which at later times was minimized as smoothing and geostrophic adjustment effects dominate.



$\Phi$  Disturbance (gpm)  
6 hours



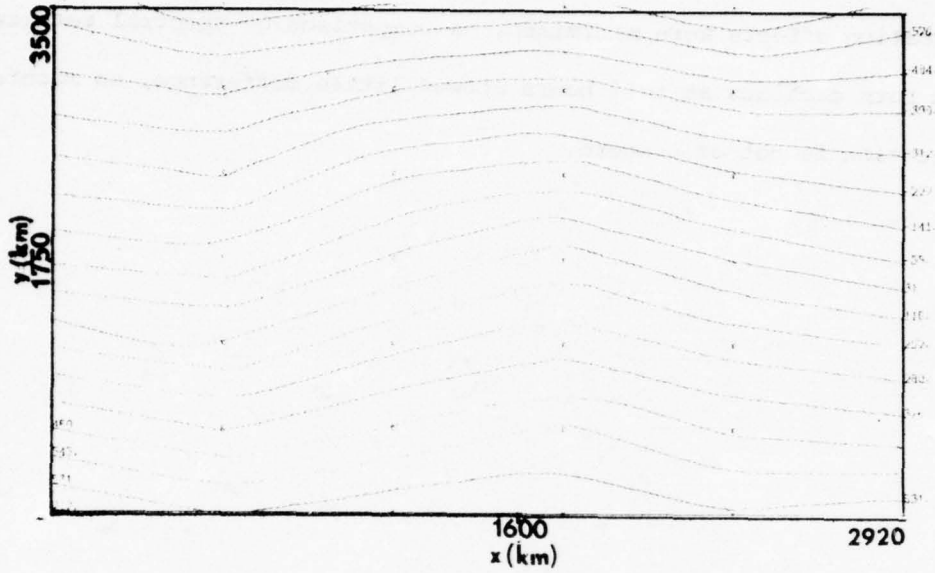
$\Phi$  Disturbance (gpm)  
24 hours



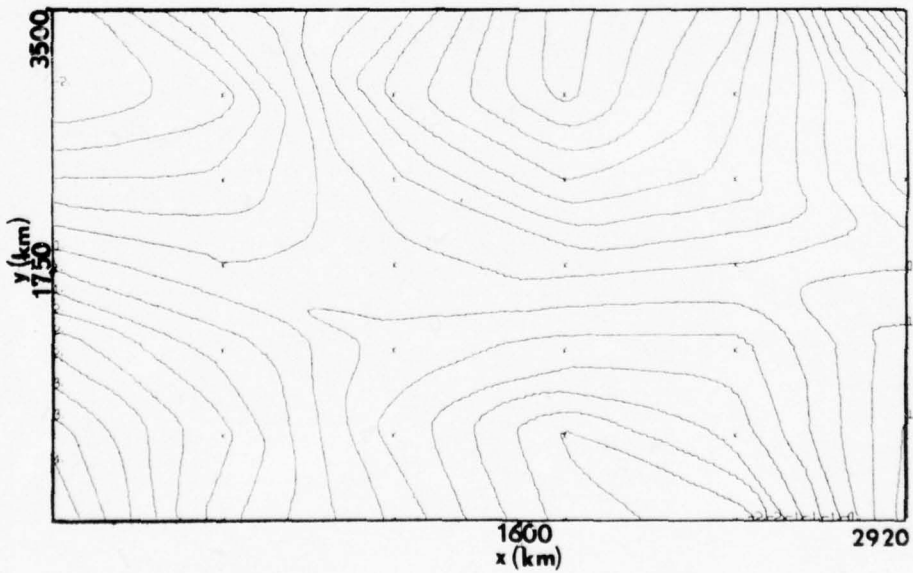
$\Phi$  Disturbance (gpm)  
48 hours

Figure 34. Geopotential field for stationary vortex on final mesh.

This final case was integrated on both an IBM 360/67 machine and a CYBER 175 machine. The CYBER machine is twice as accurate so machine truncation effects were minimized. A comparison of spectral results from both machines at  $t=12$  hours showed little difference, so machine truncation is not of concern.

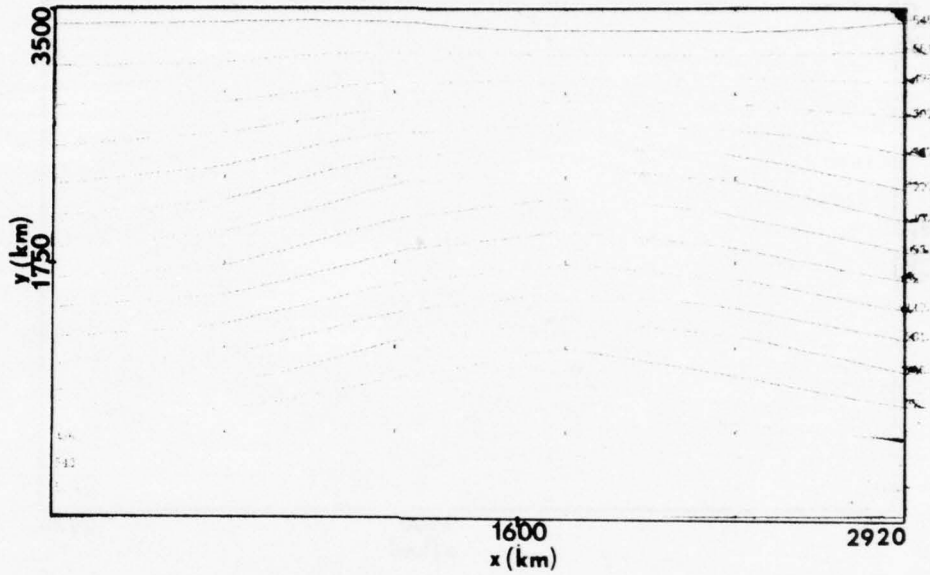


$\Phi$  Disturbance (gpm)

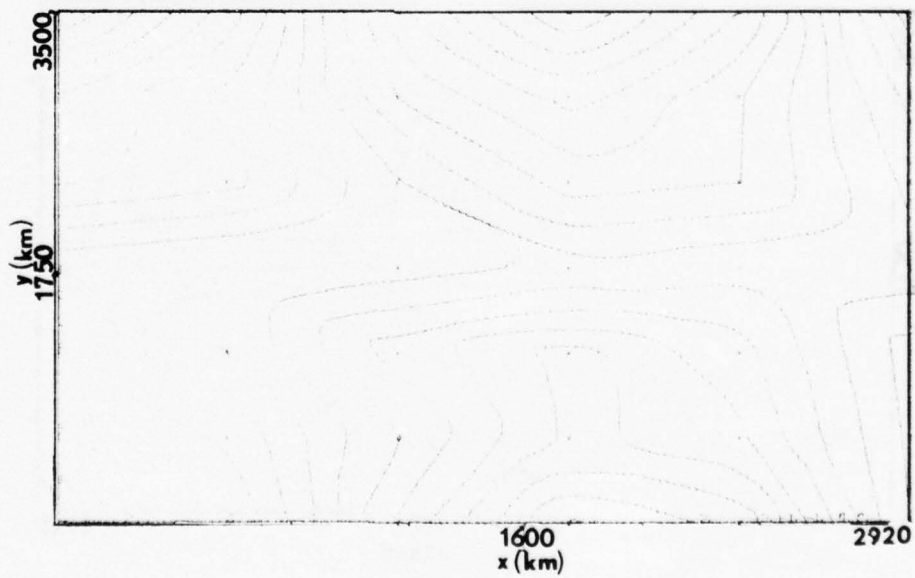


$u$  Disturbance (m/sec)

Figure 35. 6x6 [SD] at  $t=48$  hours.

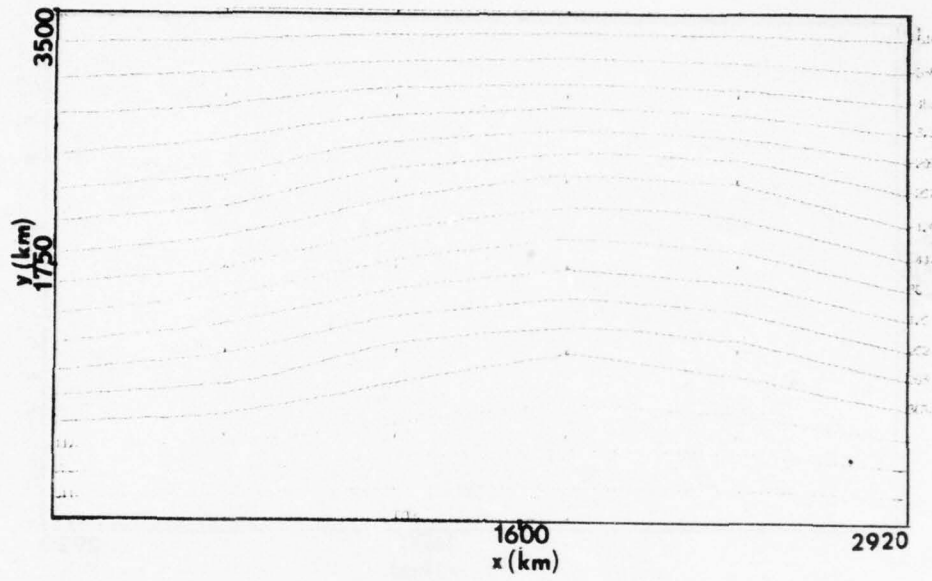


$\Phi$  Disturbance (gpm)

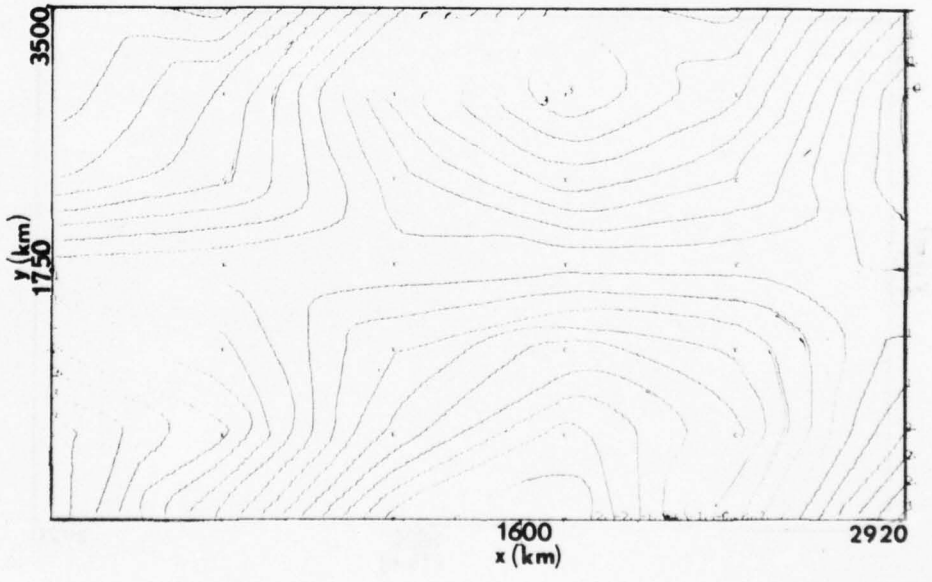


$u$  Disturbance (m/sec)

Figure 36. 6x6 [S1D] at  $t=48$  hours.

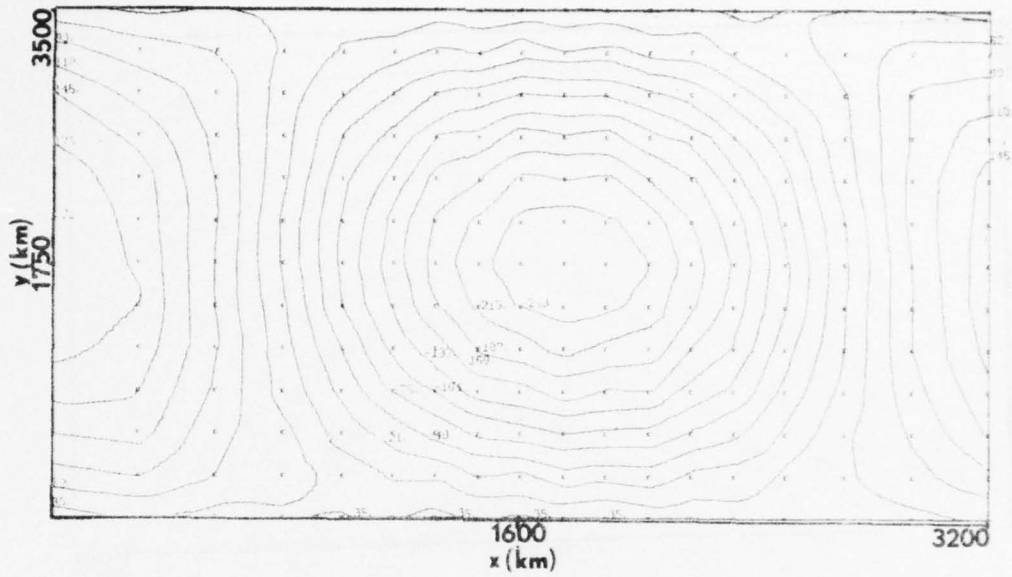


$\Phi$  Disturbance (gpm)

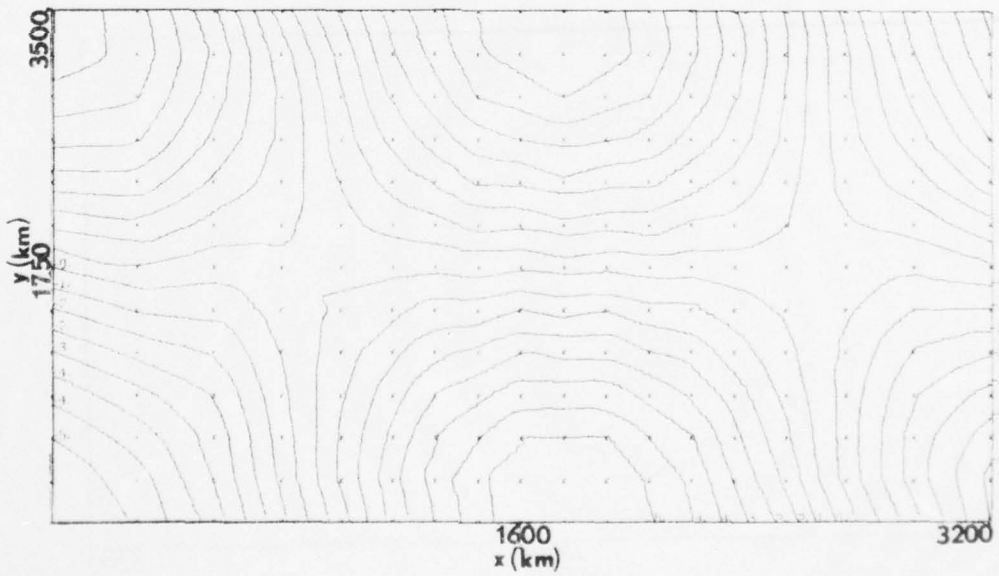


$u$  Disturbance (m/sec)

Figure 37. 6x6 [S2D] at  $t=48$  hours.

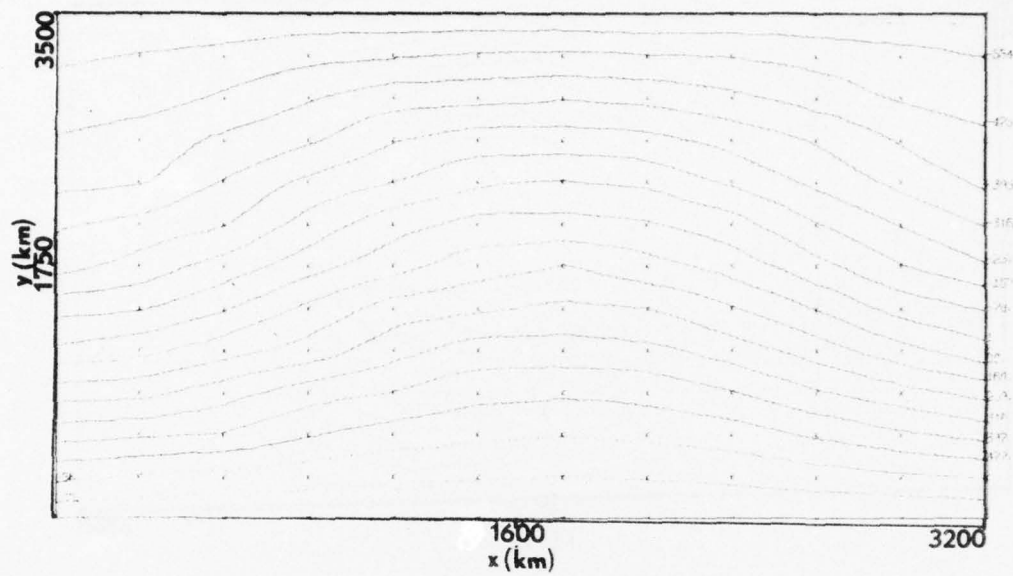


$\Phi$  Disturbance (gpm)

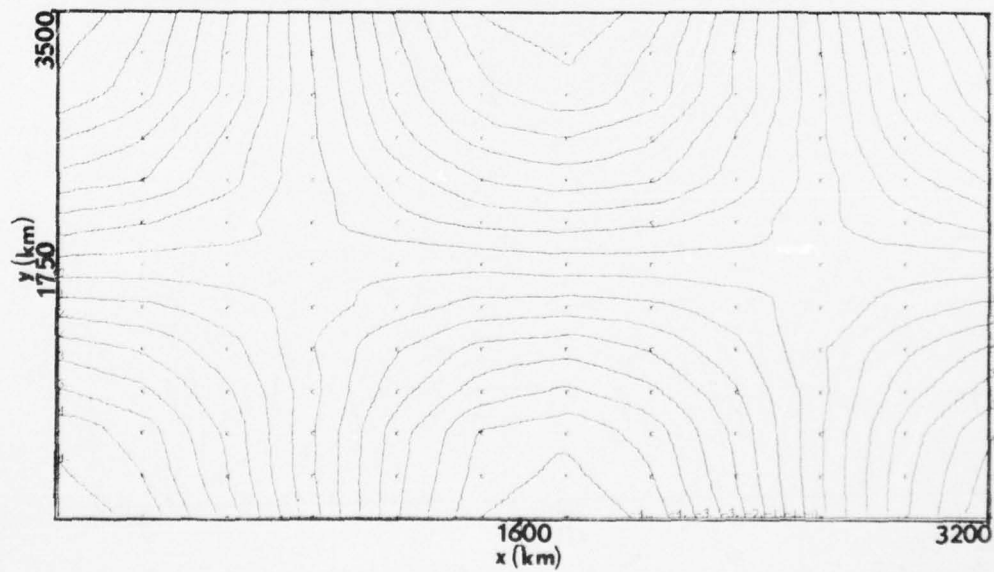


$u$  Disturbance (m/sec)

Figure 38. 18x12 [S\*\*D] at  $t=48$  hours.

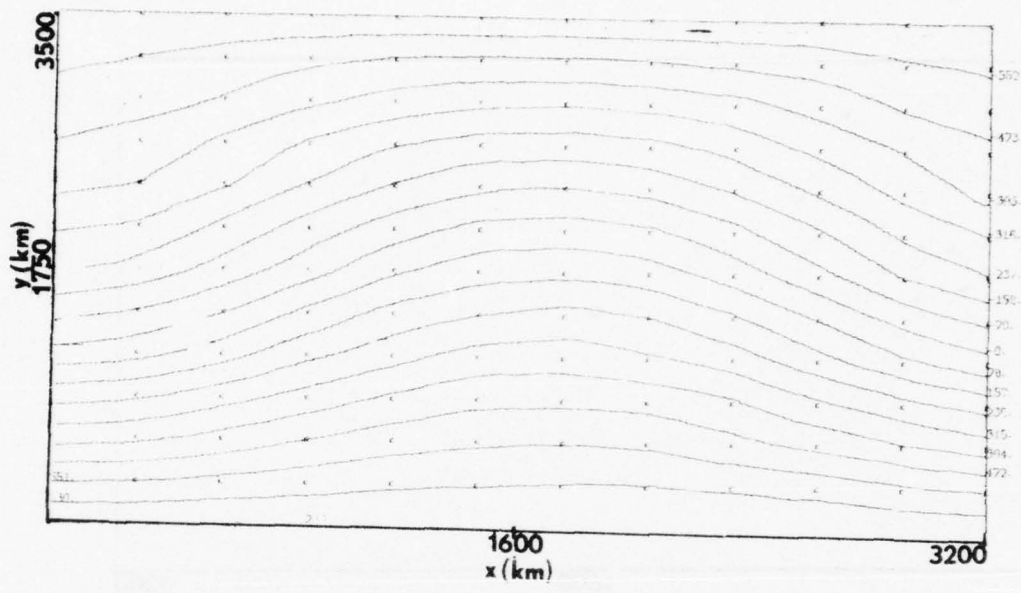


$\Phi$  Disturbance (gpm)

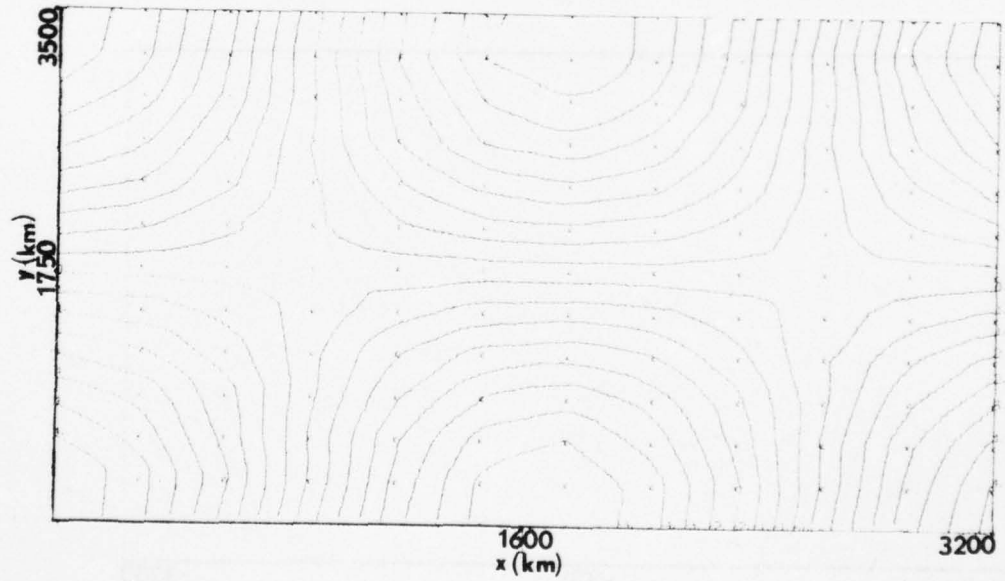


$u$  Disturbance (m/sec)

Figure 39. 12x12 [S1D] at  $t=48$  hours.

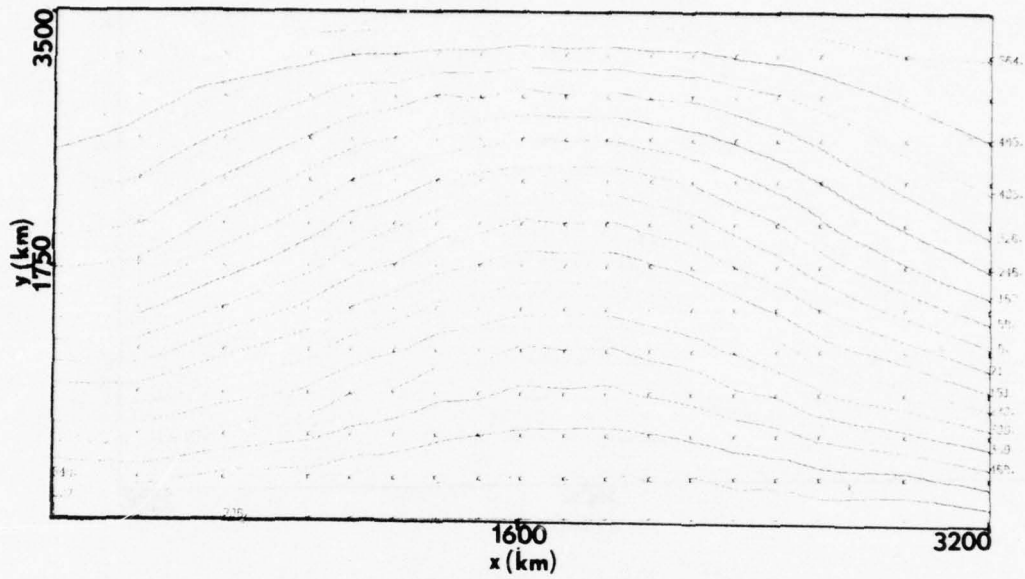


$\Phi$  Disturbance (gpm)

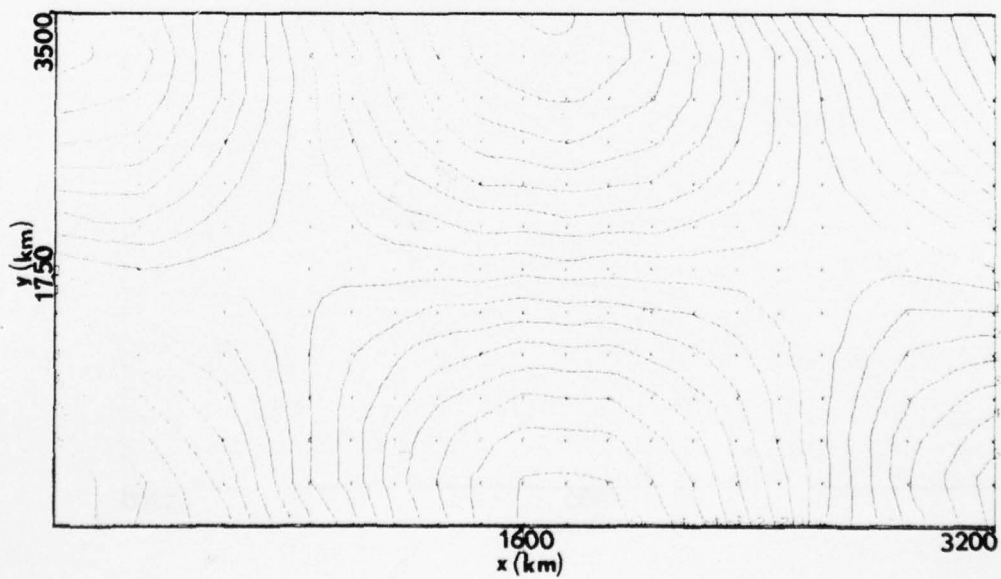


$u$  Disturbance (m/sec)

Figure 40. 12x12 [S2D] at  $t=48$  hours.

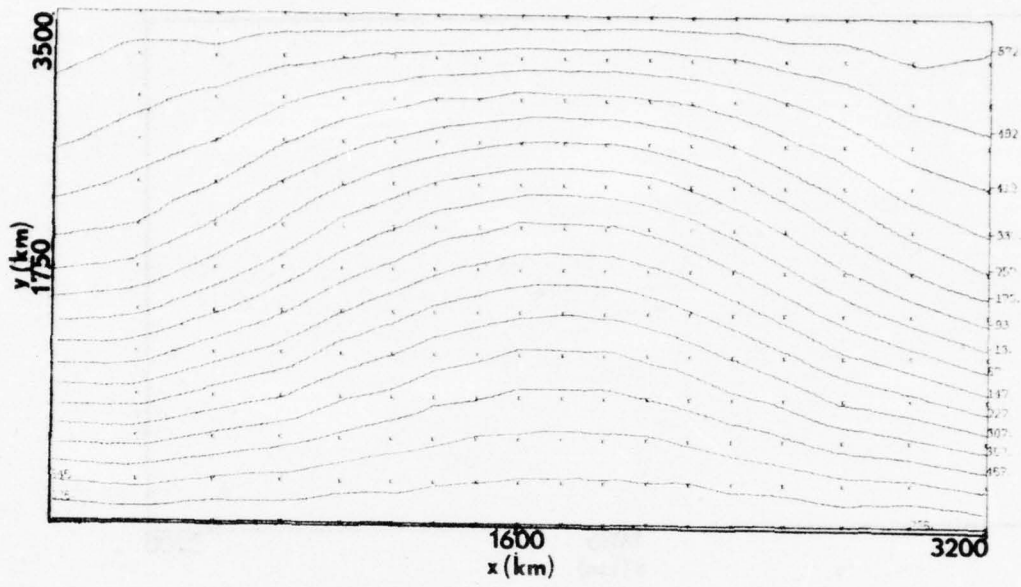


$\phi$  Disturbance (gpm)

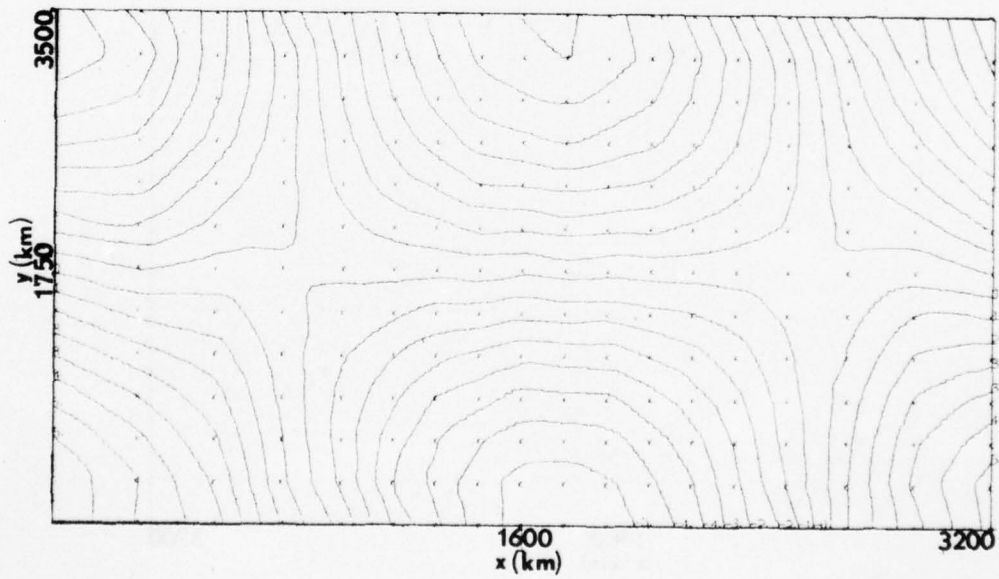


$u$  Disturbance (m/sec)

Figure 41. 18x12 [SD] at  $t=48$  hours.

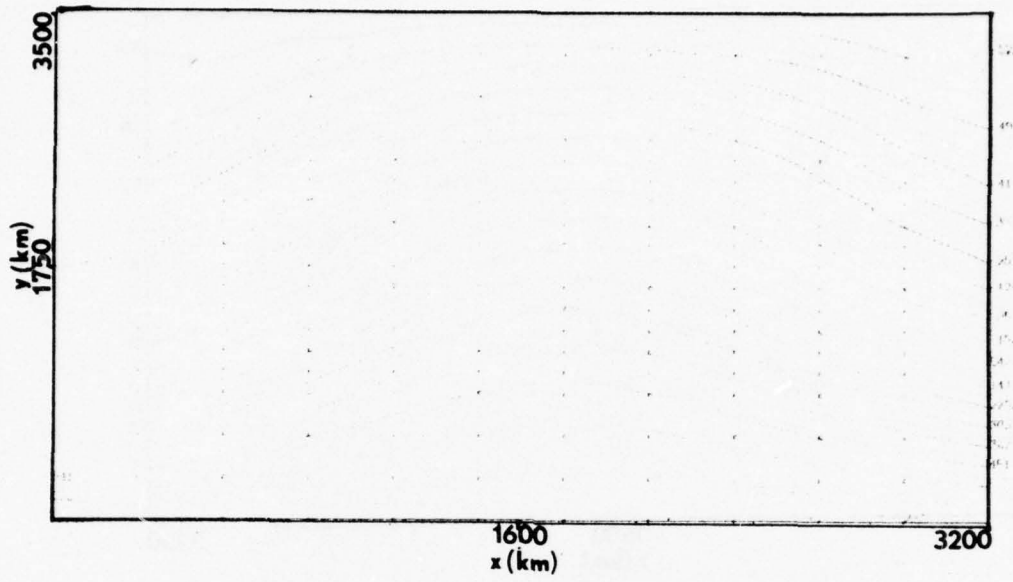


$\Phi$  Disturbance (gpm)

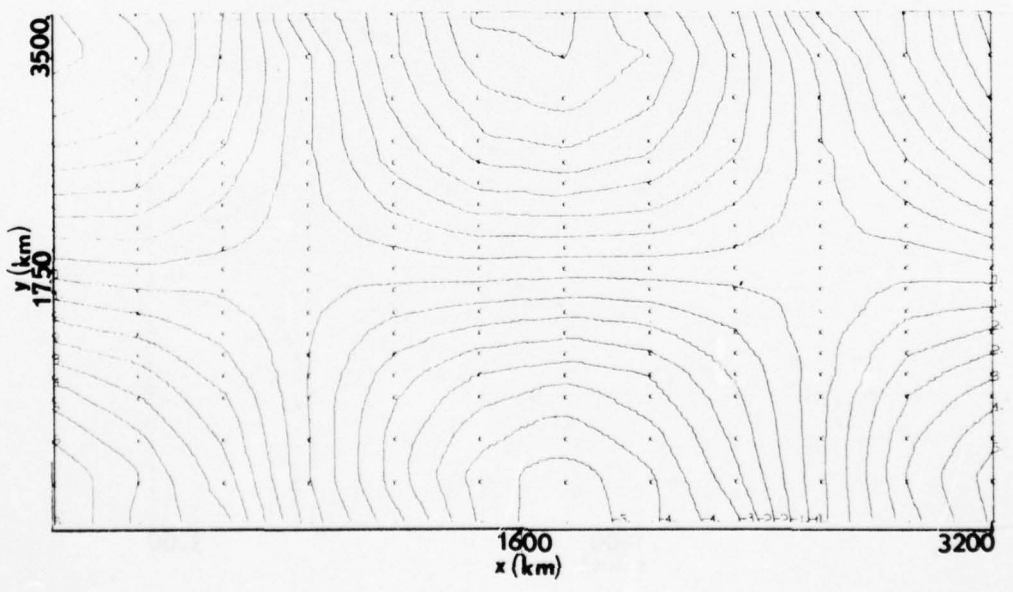


$u$  Disturbance (m/sec)

Figure 42. 18x12G [SD] at  $t=48$  hours.

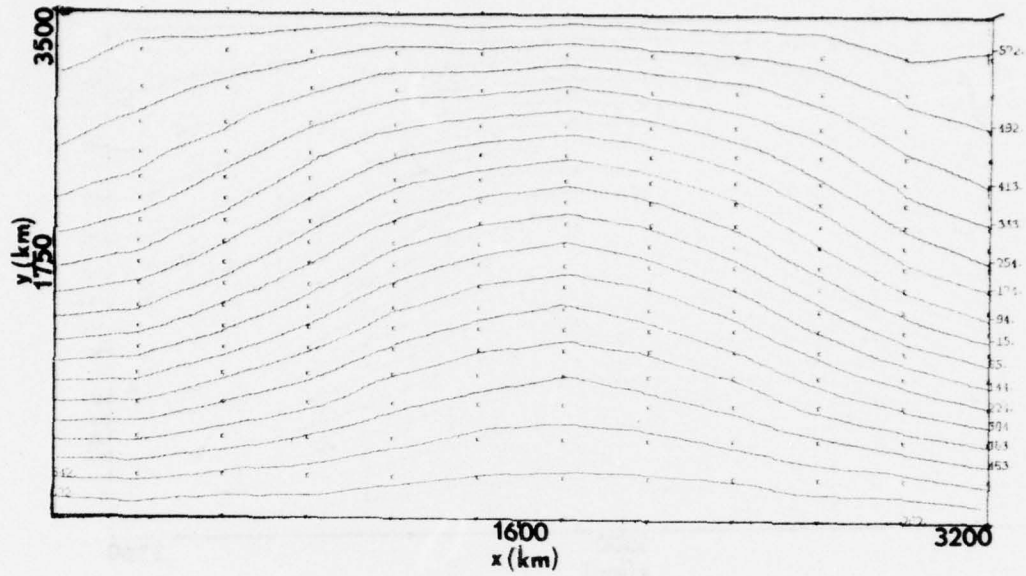


$\Phi$  Disturbance (gpm)

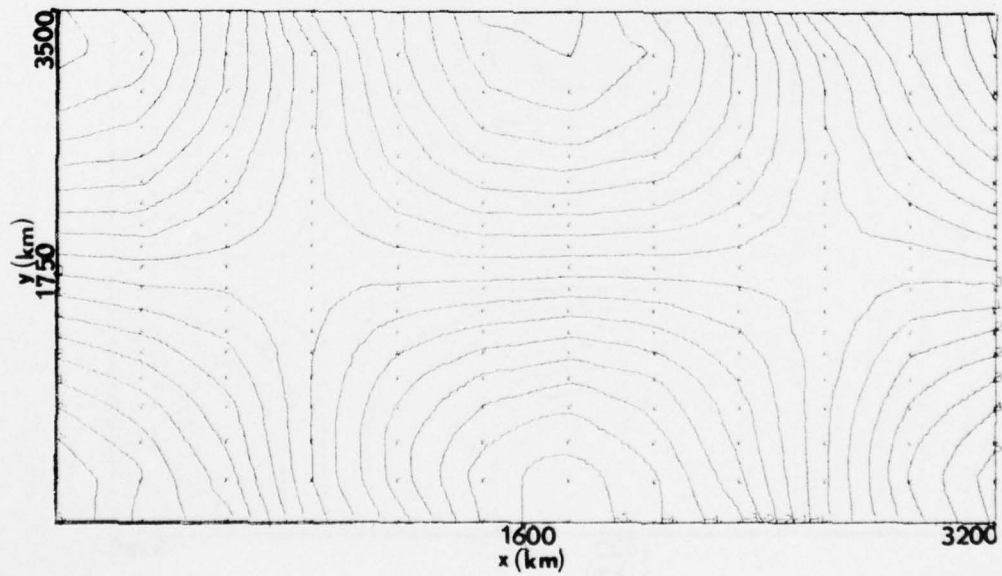


$u$  Disturbance (m/sec)

Figure 43. 12x18 [SD] at t=48 hours.

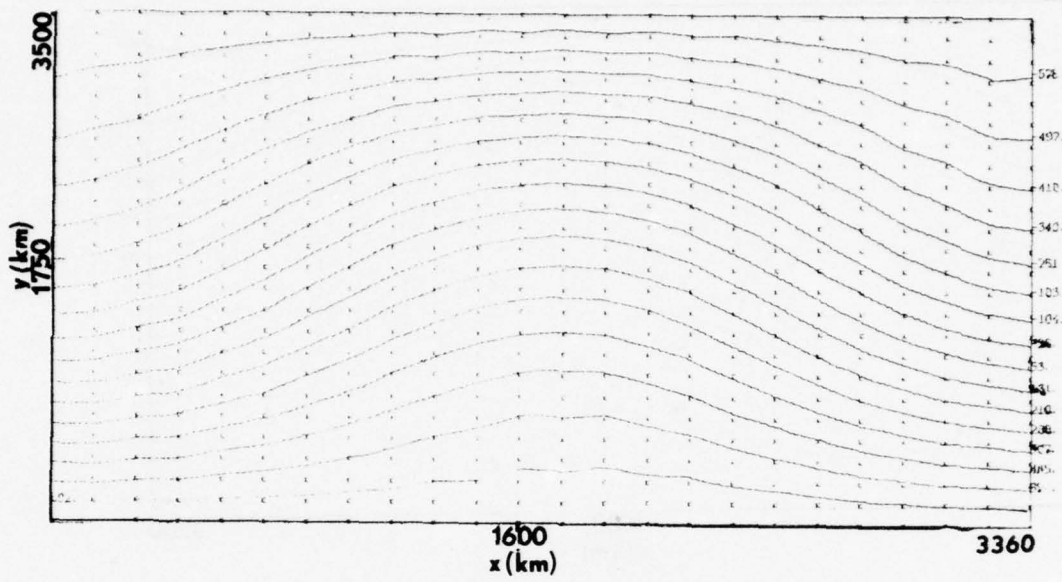


$\Phi$  Disturbance (gpm)

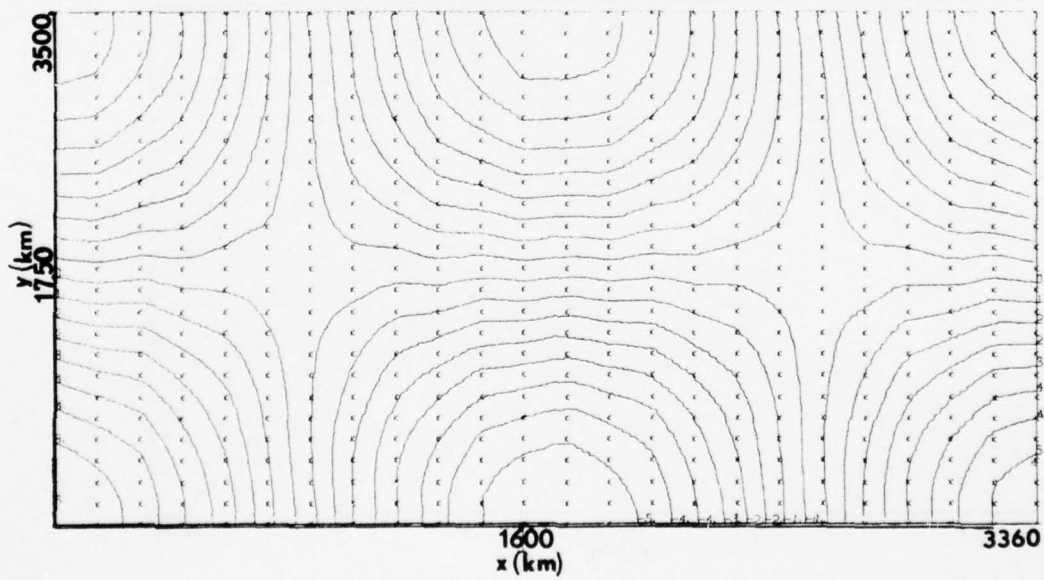


$u$  Disturbance (m/sec)

Figure 44. 12x18G [SD] at  $t=48$  hours.

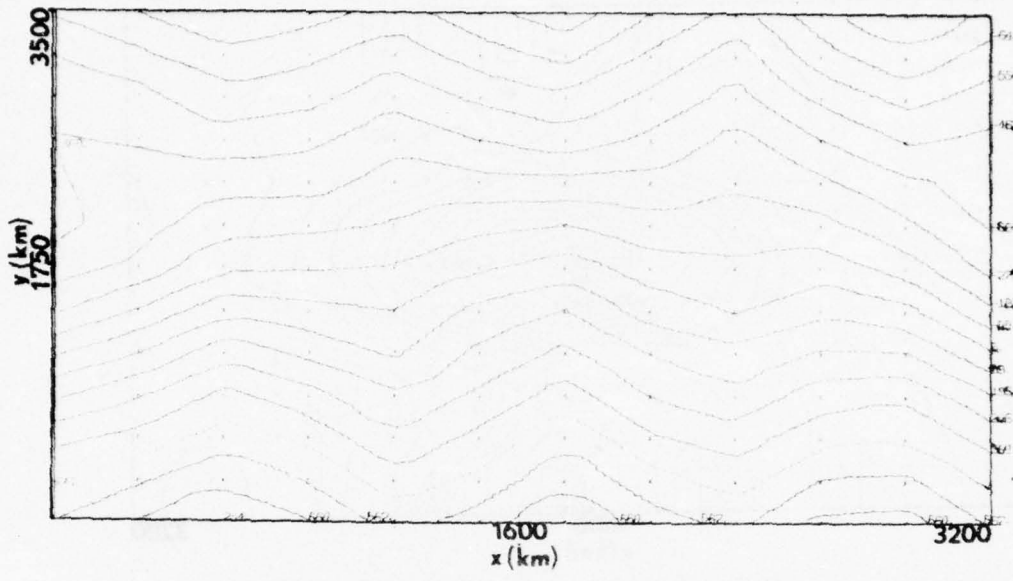


$\Phi$  Disturbance (gpm)

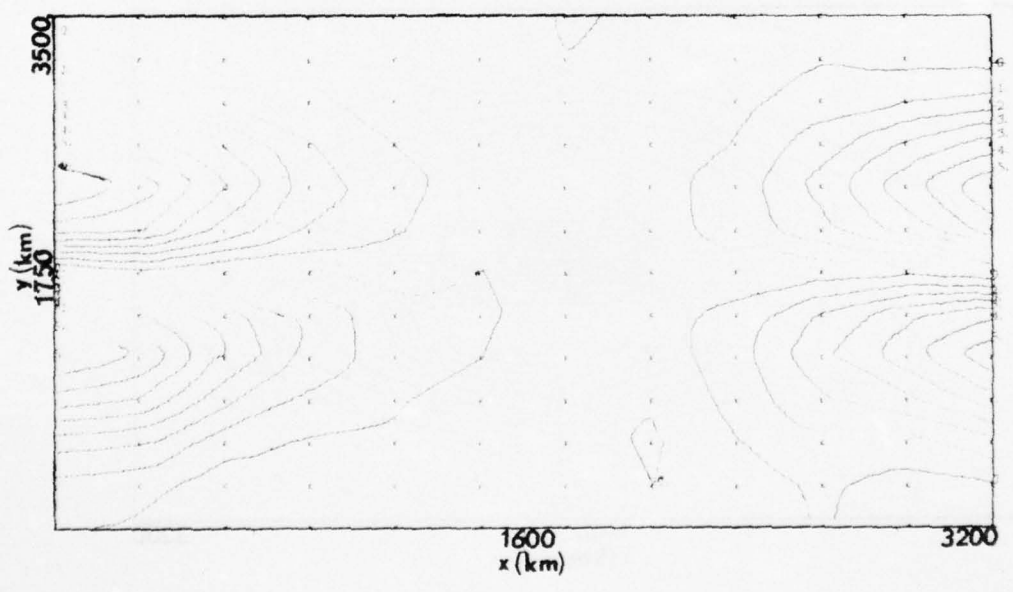


$u$  Disturbance (m/sec)

Figure 45. 24x24 [SD] at  $t=48$  hours.

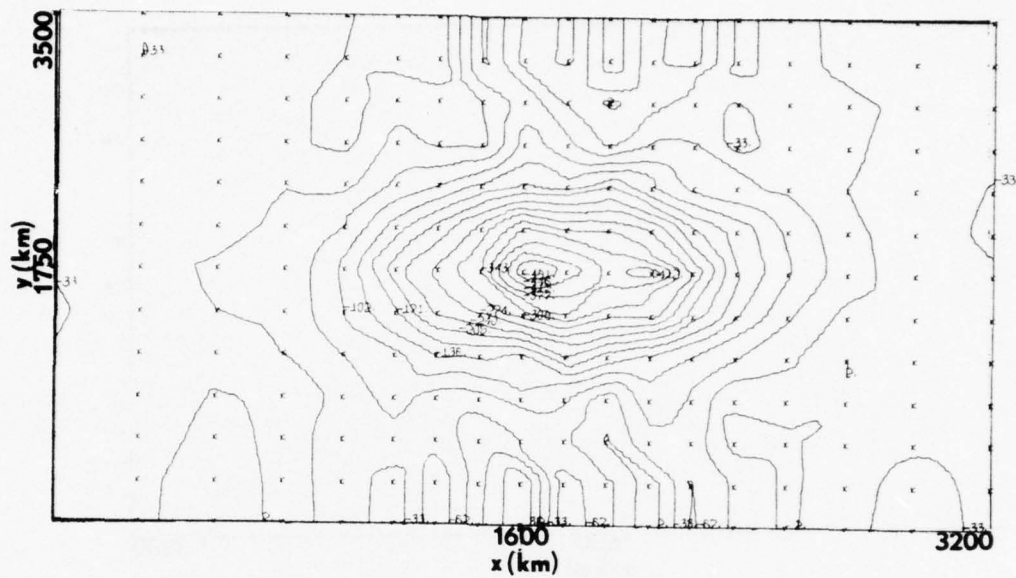


$\Phi$  Disturbance (gpm)

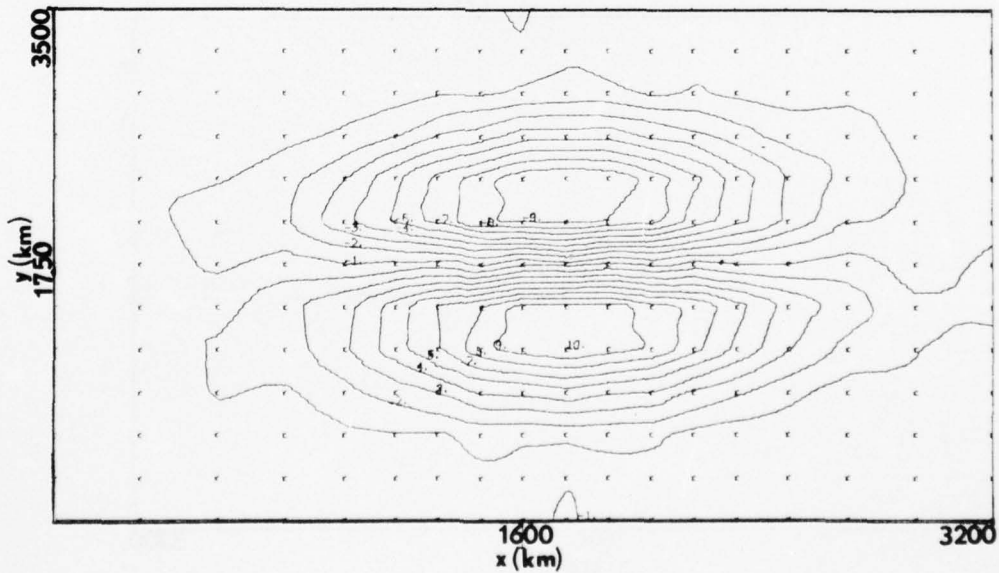


$u$  Disturbance (m/sec)

Figure 46. 12x12 [VD] at  $t=48$  hours.

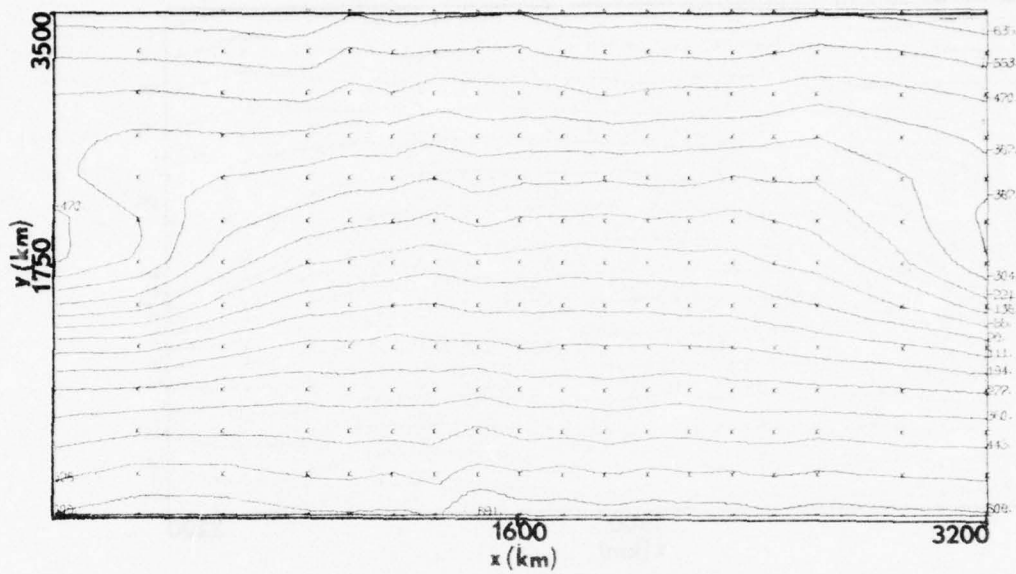


$\Phi$  Disturbance (gpm)

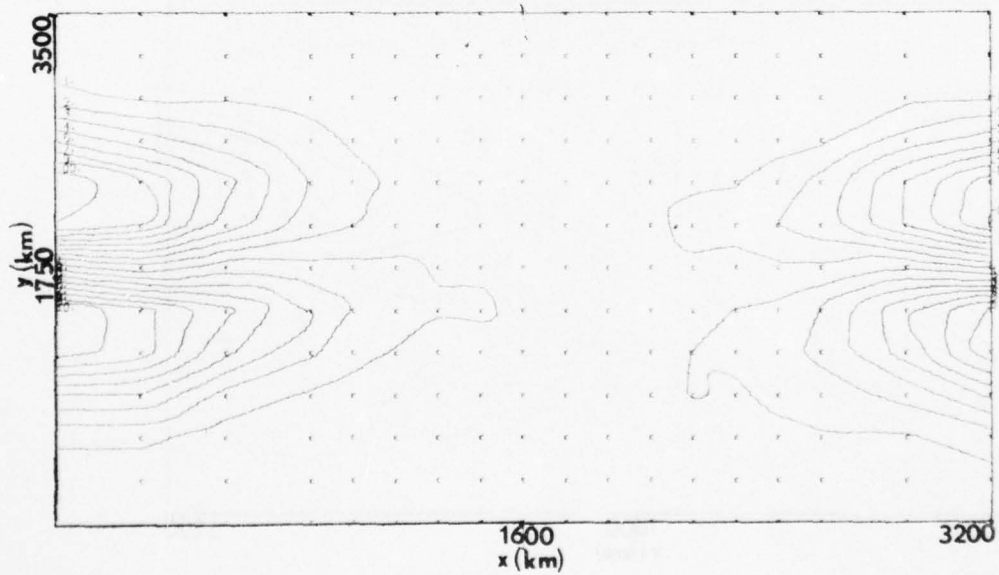


$u$  Disturbance (m/sec)

Figure 47. 18x12G [V\*\*D] at  $t=48$  hours.



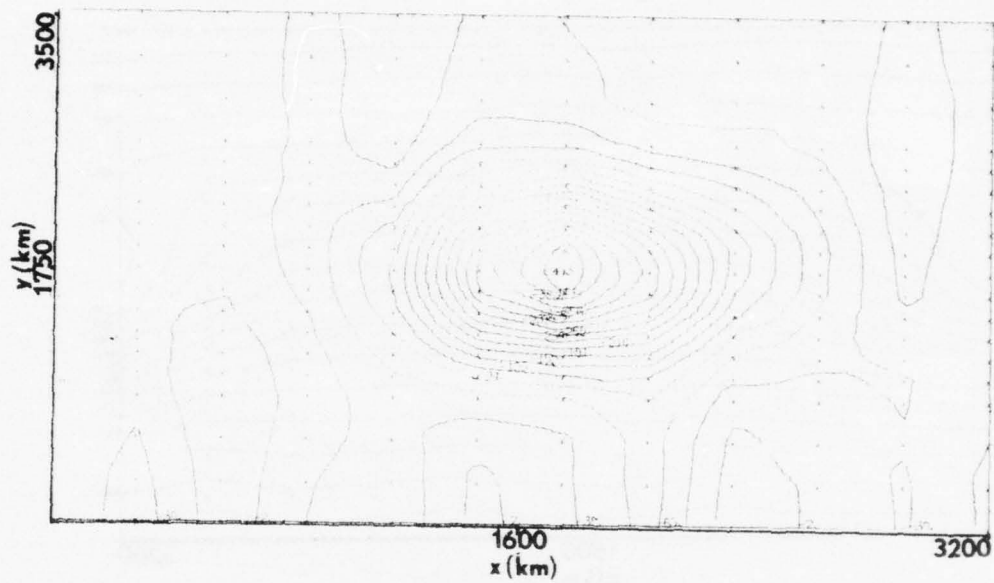
$\Phi$  Disturbance (gpm)



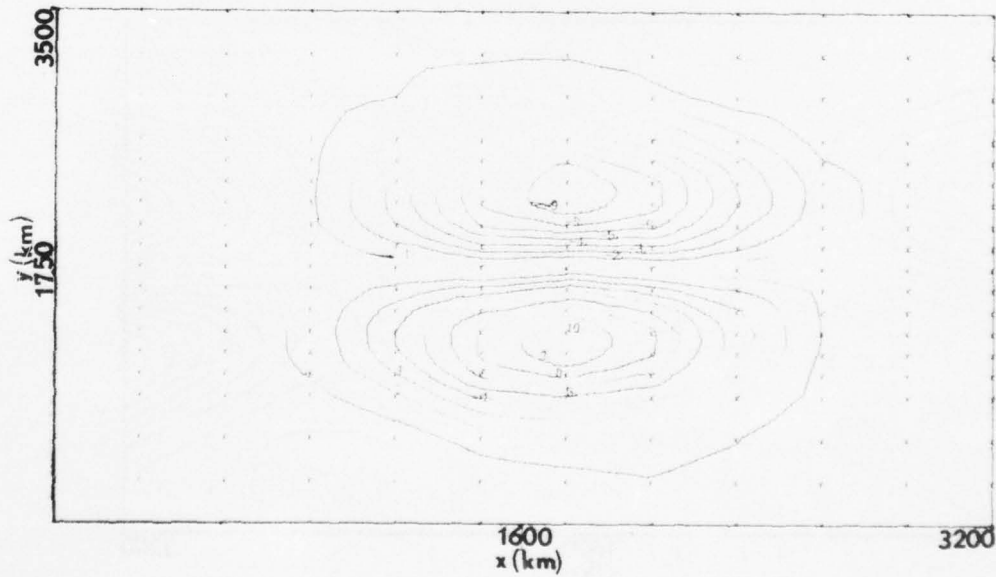
$u$  Disturbance (m/sec)

Figure 48. 18x12 [VD] at  $t=48$  hours.



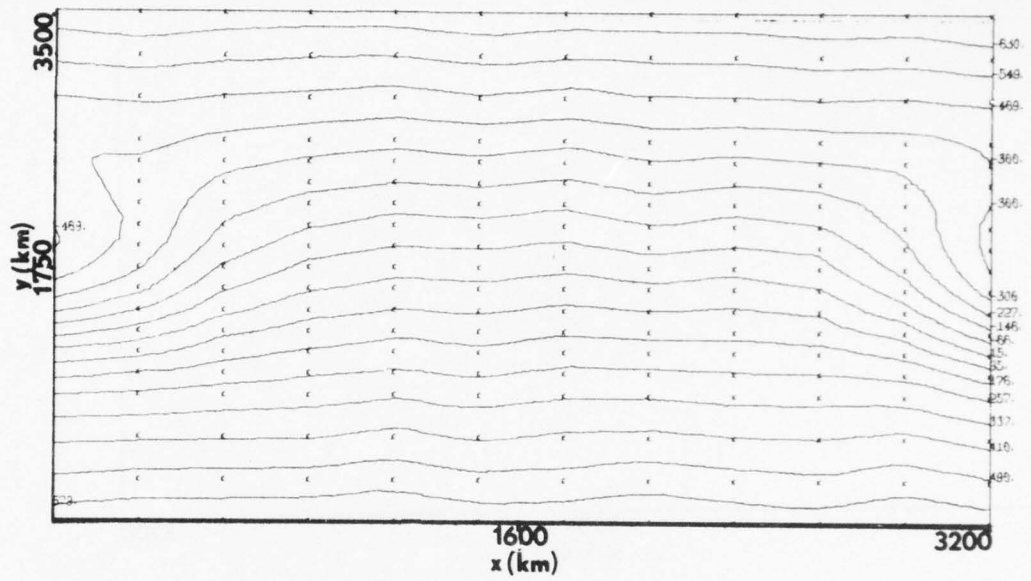


$\Phi$  Disturbance (gpm)

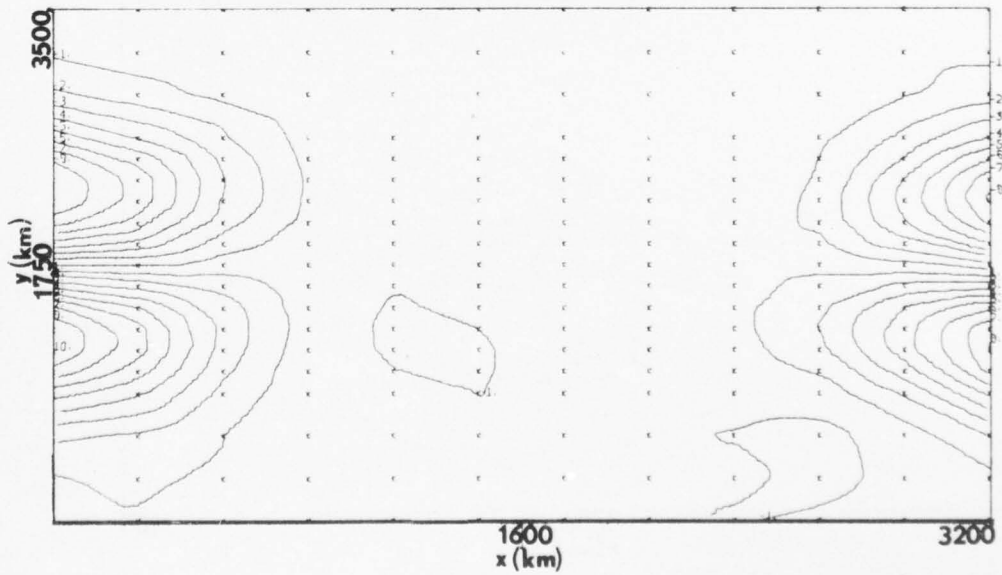


$u$  Disturbance (m/sec)

Figure 50.  $12 \times 18 [V^{**}D]$  at  $t=48$  hours.



$\Phi$  Disturbance (gpm)



$u$  Disturbance (m/sec)

Figure 51. 12x18 [VD] at  $t=48$  hours.

AD-A033 229

NAVAL POSTGRADUATE SCHOOL MONTEREY CALIF  
A FINITE ELEMENT PREDICTION MODEL WITH VARIABLE ELEMENT SIZES.(U)  
OCT 76 R G KELLEY, R T WILLIAMS

F/G 4/2

UNCLASSIFIED

NPS-63WU76101

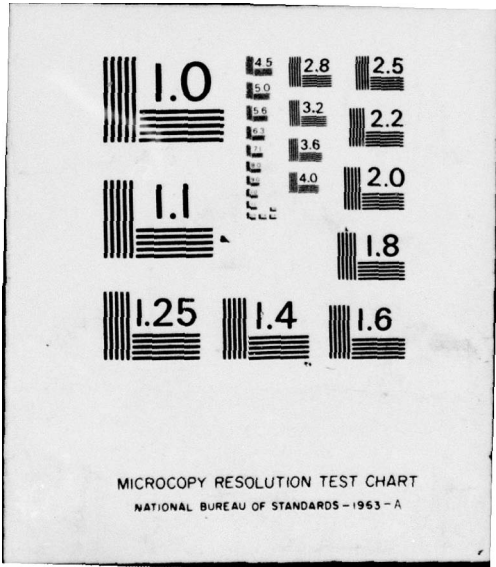
NL

2 OF 2  
AD  
A033229

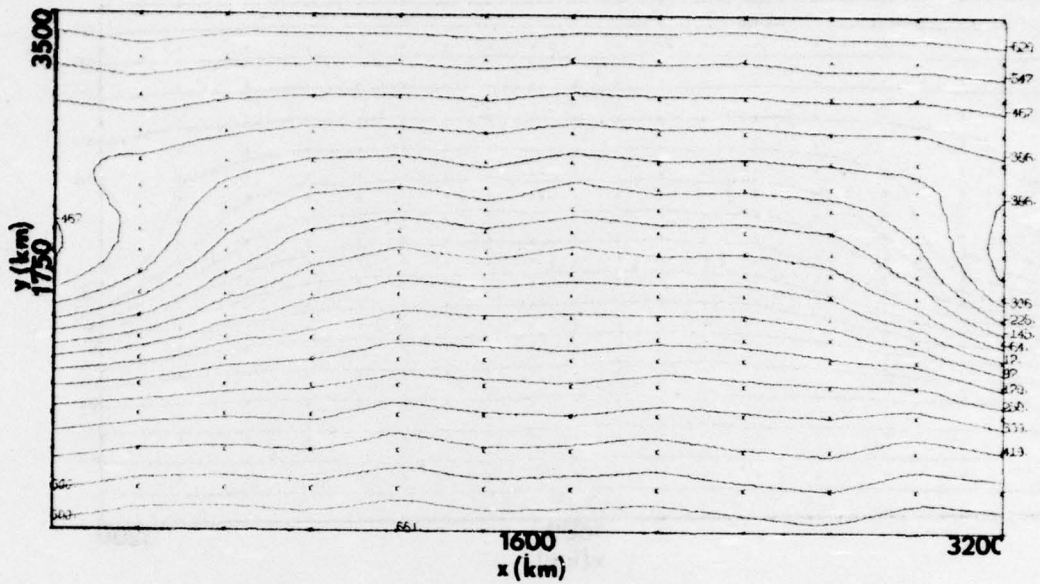


END

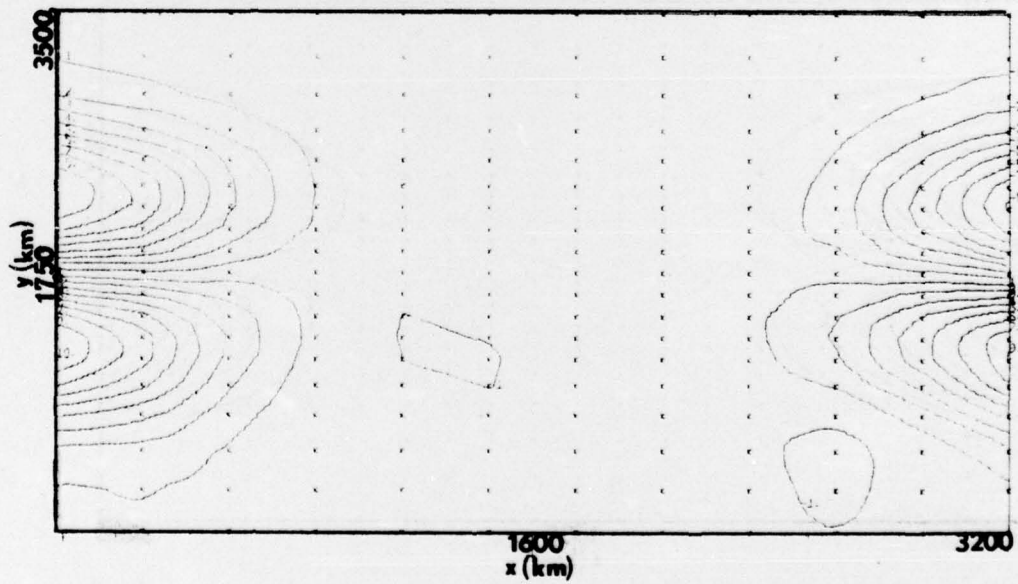
DATE  
FILMED  
2-77



MICROCOPY RESOLUTION TEST CHART  
NATIONAL BUREAU OF STANDARDS-1963-A

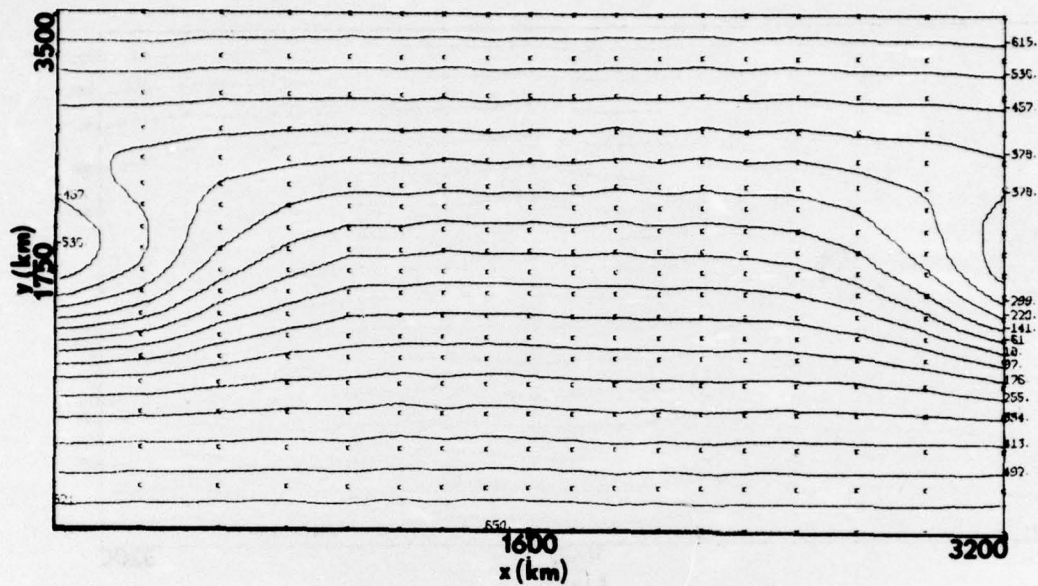


$\Phi$  Disturbance (gpm)

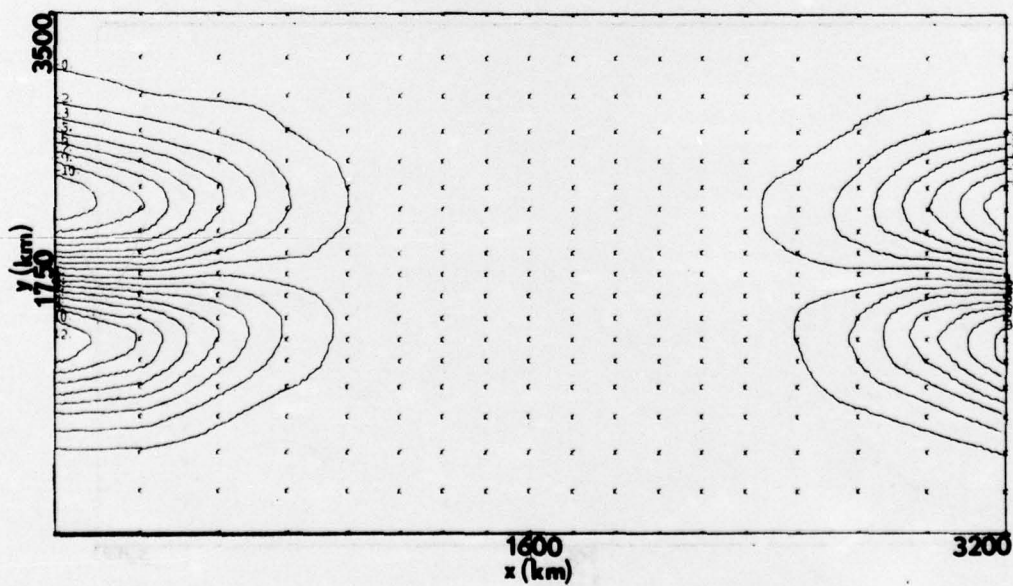


$u$  Disturbance (m/sec)

Figure 52. 12x18G [VD] at  $t=48$  hours.

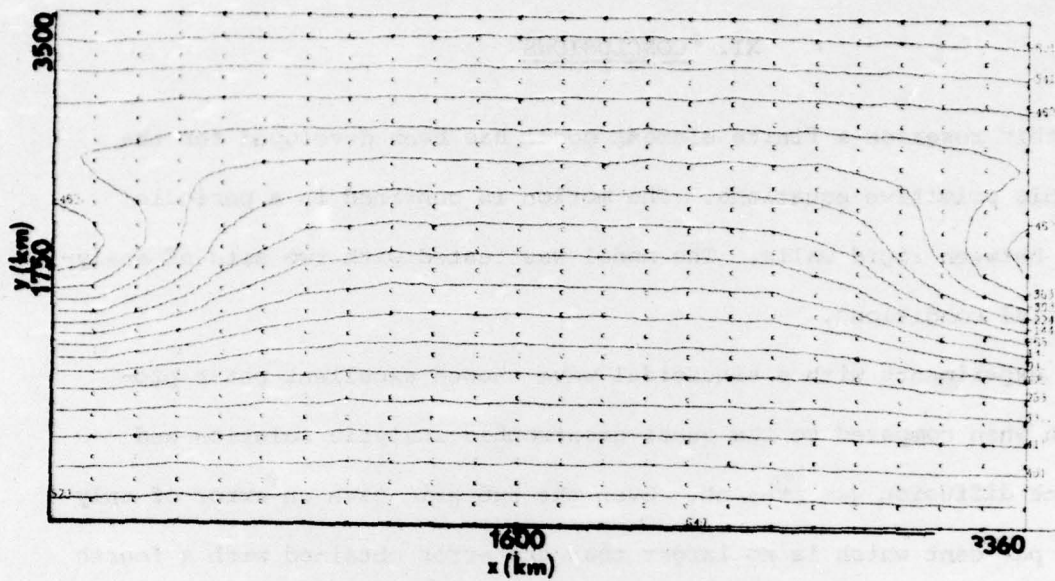


$\Phi$  Disturbance (gpm)

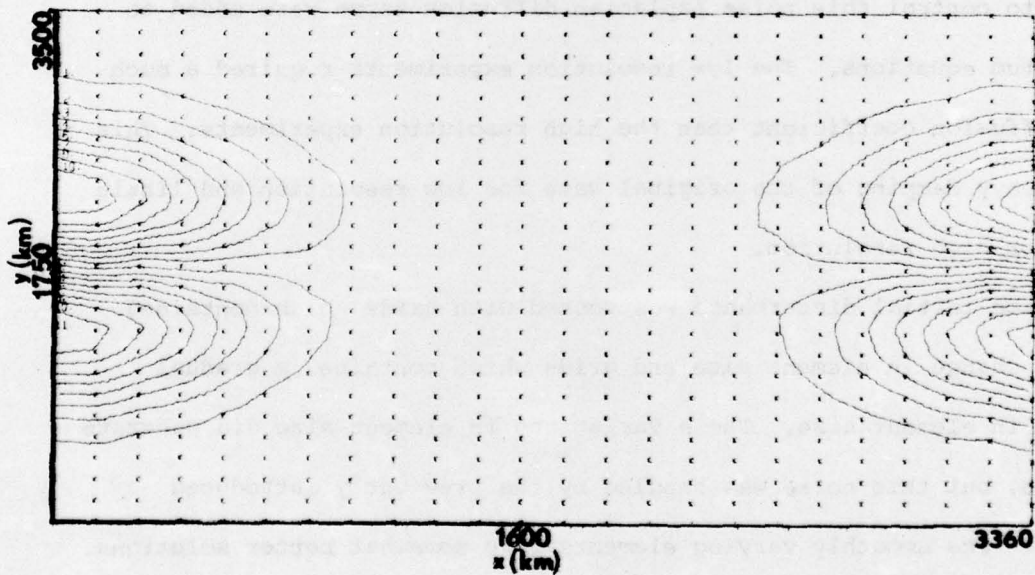


$u$  Disturbance (m/sec)

Figure 53. 18x18G [VD] at  $t=48$  hours.



$\Phi$  Disturbance (gpm)



$u$  Disturbance (m/sec)

Figure 54. 24x24 [VD] at  $t=48$  hours.

## XI. CONCLUSIONS

In this research a finite element model has been developed for the barotropic primitive equations. The motion is confined in a periodic channel between rigid walls. The model was tested with two sets of analytic initial conditions.

The experiments with a sinusoidal wave showed excellent phase propagation when compared to the quasi-geostrophic analytic solution and when some diffusion was present. Even the 6x6 grid gave an error of only about 4 per cent which is no larger than the error obtained with a fourth order finite difference model. All grids produced computational noise without diffusion which made the forecasts unrealistic at  $t=48$  hours. In order to control this noise Laplacian diffusion terms were added to the momentum equations. The low resolution experiments required a much higher diffusion coefficient than the high resolution experiments. This lead to heavy damping of the original wave for low resolution and little damping for high resolution.

The same initial disturbance was tested with grids which contained an abrupt change in element size and grids which contained a gradual variation in element size. These variations in element size did generate some noise, but this noise was handled by the previously introduced diffusion. The smoothly varying elements gave somewhat better solutions.

The model was also tested with an isolated vortex with the initial pressure determined analytically from the gradient wind equation. The experiments with a uniform element size displayed gravity waves which were excited by the finite element imbalance in the initial conditions.

The required diffusion damped and enlarged the initial vortex. The vortex experiments with a variable element size showed much better results. This was a result of the higher resolution around the vortex and the lower diffusion. Some experiments were performed with a continuously varying element formulation which had very small central elements. This procedure was very uneconomical because a very small time step had to be used throughout the domain (see Table II).

This study has verified the previously discussed phase accuracy of the finite element method. However, the noise generation was larger than expected. It is not known whether or not some of the noise arises from imperfect boundary conditions at the walls. Cullen (1974, 1976) has discussed the necessity of high order smoothing with finite element models. In any case the model developed in this study would be benefited by a high-order spatial filter which would control the noise while not affecting the larger scale features.

The main problem with the use of variable element size is the requirement that the same time step be used everywhere. Finite difference models need use small time step only in the high resolution regions. Until this problem is solved it would appear that the element size should not be varied by a large amount. But since the FEM is more accurate perhaps tropical storm forecasts can be made without excessively small element sizes. The model developed in this paper requires testing with a moving element system. Further work is also required to make the model more efficient.

TABLE II

48 Hour PROGNOSIS  
IBM 360/67 TIME AND STORAGE REQUIREMENTS  
(Fortran H compiler)

GRID	AVERAGE EXECUTION TIME	STORAGE REQUIREMENTS (IN BYTES, 1 BYTE = 4 WORDS)
6x6	3 minutes	49K
12x12	22 minutes	129K
12x18	1 hour 20 minutes	188K
18x12		
18x18	1 hour 50 minutes	261K
24x24	3 hours 40 minutes	442K
Final	10 hours (IBM)	
Graded	1 hour 20 minutes (CYBER 175)	168K (IBM)
Grid		

#### LIST OF REFERENCES

1. Cullen, M. J. P., "A Simple Finite Element Method for Meteorological Problems," J. Inst. Maths Applics., v. 11, p. 15-31, 1973.
2. \_\_\_\_\_, "A Finite Element Method for a Non-Linear Initial Value Problem," J. Inst. Maths Applics., v. 13, p. 234-237, 1974.
3. \_\_\_\_\_, "Integrations of the Primitive Equations on a Sphere Using the Finite Element Method," Quart. J. R. Met. Soc., v. 100, p. 555-562, 1974.
4. \_\_\_\_\_, "On the Use of Artificial Smoothing in Galerkin and Finite Difference Solutions of the Primitive Equations," Quart. J. R. Met. Soc., v. 102, p. 77-93, 1976.
5. Desai, C. S., Introduction to the Finite Element Method A Numerical Method for Engineering Analysis, Van Nostrand Reinhold Company, 1972.
6. Galerkin, B. G., Vestnik Inzhenerov, 1, p. 897-908, 1915.
7. Hinsman, D. E., Application of a Finite Element Method to the Barotropic Primitive Equations, M. S. Thesis, Naval Postgraduate School, 1975.
8. Houghton, D. D. and W. S. Irvine, Jr., A Case Study Comparison of the Performance of Operational Prediction Models Used in the United States, paper presented at Conference on Weather Forecasting and Analysis, 6th, Albany, New York, 10 May through 14 May 1976.
9. Phillips, N. A., "Numerical Integration of the Primitive Equations on the Hemisphere," Monthly Weather Review, p. 333-345, September 1959.
10. Zienkiewicz, O. C., The Finite Element Method in Engineering Science, McGraw Hill, 1971.

DISTRIBUTION LIST

	No. Copies
1. Defense Documentation Center Cameron Station Alexandria, Virginia 22314	12
2. Library, Code 0142 Naval Postgraduate School Monterey, California 93940	2
3. Dr. R. T. Williams, Code 63Wu Department of Meteorology Naval Postgraduate School Monterey, California 93940	20
4. Director Naval Oceanography and Meteorology National Space Technology Laboratories Bay St. Louis, Mississippi 39520	1
5. Officer in Charge Navy Environmental Prediction Research Facility Monterey, California 93940	10
6. Dean of Research, Code 012 Naval Postgraduate School Monterey, California 93940	2
7. Commanding Officer Fleet Numerical Weather Central Monterey, California 93940	2
8. Naval Oceanographic Office Library, Code 3330 Washington, D. C. 20373	1
9. AFCRL Research Library ATTN: Nancy Davis/Stop 29 L. G. Hanscom Field Bedford, Massachusetts 01730	1
10. Commander, Air Weather Service Military Airlift Command United States Air Force Scott Air Force Base, Illinois 62226	1
11. Dr. A. Arakawa Department of Meteorology University of California Los Angeles, California 90024	1

12. Dr. David Archer 1  
 Mathematics Department  
 University of North Carolina-Charlotte  
 University of North Carolina Station  
 Charlotte, North Carolina 28223
13. Atmospheric Sciences Library 1  
 National Oceanic and Atmospheric Administration  
 Silver Spring, Maryland 20910
14. Dr. F. P. Bretherton 1  
 National Center for Atmospheric Research  
 P. O. Box 3000  
 Boulder, Colorado 80303
15. Dr. John Brown 1  
 National Meteorological Center/NOAA  
 World Weather Building  
 Washington, D. C. 20233
16. Dr. C.-P. Chang, Code 63Cj 1  
 Department of Meteorology  
 Naval Postgraduate School  
 Monterey, California 93940
17. Prof. J. G. Charney 1  
 54-1424  
 Massachusetts Institute of Technology  
 Cambridge, Massachusetts 02139
18. Dr. C. Comstock, Code 53Zk 1  
 Department of Mathematics  
 Naval Postgraduate School  
 Monterey, California 93940
19. Dr. M. J. P. Cullen 1  
 Meteorological Office  
 London Road  
 Bracknell, Berkshire RG12252  
 United Kingdom
20. Dr. R. L. Elsberry, Code 63Es 1  
 Department of Meteorology  
 Naval Postgraduate School  
 Monterey, California 93940
21. Prof. F. D. Faulkner, Code 53Fa 1  
 Naval Postgraduate School  
 Monterey, California 93940
22. Prof. R. Franke, Code 53Fe 1  
 Naval Postgraduate School  
 Monterey, California 93940

23. Dr. G. A. Galt 1  
 NOAA, Pac. Mar. Env. Lab.  
 University of Washington WB-10  
 Seattle, Washington 98105
24. Dr. W. L. Gates 1  
 Department of Meteorology  
 Oregon State University  
 Corvallis, Oregon 97331
25. Dr. Earl Gossard 1  
 Wave Propagation Laboratory  
 NOAA/ERL  
 Boulder, Colorado 80302
26. Dr. Phillip Gresho 1  
 Environmental Group  
 Lawrence Livermore Laboratories  
 University of California  
 Livermore, California 94550
27. Dr. G. J. Haltiner, Code 63Ha 1  
 Chairman, Department of Meteorology  
 Naval Postgraduate School  
 Monterey, California 93940
28. Dr. R. L. Haney, Code 63Hy 1  
 Department of Meteorology  
 Naval Postgraduate School  
 Monterey, California 93940
29. Lt. D. Hinsman 1  
 Fleet Numerical Weather Central  
 Monterey, California 93940
30. Dr. J. Holton 1  
 Department of Atmospheric Sciences  
 University of Washington  
 Seattle, Washington 98105
31. Dr. B. J. Hoskins 1  
 Department of Geophysics  
 University of Reading  
 Reading, United Kingdom
32. Dr. D. Houghton 1  
 Department of Meteorology  
 University of Wisconsin  
 Madison, Wisconsin 53706
33. Dr. Joseph Huang 1  
 Great Lakes Environmental Res. Lab., NOAA  
 2300 Washtenaw Avenue  
 Ann Arbor, Michigan 48104

34. Professor A. Huss 1  
 Department of Meteorology  
 The Hebrew University  
 Jerusalem, Israel
35. Dr. S. K. Kao 1  
 Department of Meteorology  
 University of Utah  
 Salt Lake City, Utah 84112
36. Dr. A. Kasahara 1  
 National Center for Atmospheric Research  
 P. O. Box 3000  
 Boulder, Colorado 80303
37. Lt. Richard G. Kelley, Jr. 5  
 c/o Mr. John S. Floyd  
 338 East Chapel Street  
 Hazleton, Pennsylvania 18201
38. Cdr. W. R. Lambertson 1  
 Fleet Weather Facility Suitland  
 Navy Department  
 Washington, D. C. 20373
39. Dr. C. E. Leith 1  
 National Center for Atmospheric Research  
 P. O. Box 3000  
 Boulder, Colorado 80303
40. Dr. J. M. Lewis 1  
 Laboratory for Atmospheric Research  
 University of Illinois  
 Urbana, Illinois 61801
41. Dr. E. N. Lorenz 1  
 Department of Meteorology  
 Massachusetts Institute of Technology  
 Cambridge, Massachusetts 02139
42. Lt. Olaf M. Lubeck 1  
 Department of Meteorology  
 Naval Postgraduate School  
 Monterey, California 93940
43. Dr. R. Madala 1  
 Code 7750  
 Naval Research Laboratories  
 Washington, D. C. 20390
44. Dr. J. D. Mahlman 1  
 Geophysical Fluid Dynamics Laboratory  
 Princeton University  
 Princeton, New Jersey 08540

45. Meteorology Library, Code 63 1  
Naval Postgraduate School  
Monterey, California 93940
46. National Center for Atmospheric Research 1  
Box 1470  
Boulder, Colorado 80302
47. Director, Naval Research Laboratory  
ATTN: Technical Services Information Center  
Washington, D. C. 20390
48. Dr. E. C. Nickerson 1  
NOAA, Atmospheric Physics & Chemistry Laboratory  
Boulder, Colorado 80302
49. Department of Oceanography, Code 68 1  
Naval Postgraduate School  
Monterey, California 93940
50. Office of Naval Research 1  
Department of the Navy  
Washington, D.C. 20360
51. Dr. T. Ogura 1  
Laboratory for Atmospheric Research  
University of Illinois  
Urbana, Illinois 61801
52. Prof. K. Ooyama 1  
National Center for Atmospheric Research  
P. O. Box 3000  
Boulder, Colorado 80303
53. Dr. I. Orlanski 1  
Geophysical Fluid Dynamics Laboratory  
Princeton University  
Princeton, New Jersey 08540
54. Prof. N. A. Phillips 1  
National Meteorological Center/NOAA  
World Weather Building  
Washington, D. C. 20233
55. Dr. S. Piacsek 1  
Code 7750  
Naval Research Laboratory  
Washington, D. C. 20390
56. Dr. N. Ramanathan 1  
Department of Meteorology  
University of Oklahoma  
Norman, Oklahoma 73069

57. Dr. T. Rosmond 1  
 Navy Environmental Prediction Research Facility  
 Monterey, California 93940
58. Prof. D. Salinas 1  
 Department of Mechanical Engineering  
 Naval Postgraduate School  
 Monterey, California 93940
59. Dr. Y. Sasaki 1  
 Navy Environmental Prediction Research Facility  
 Monterey, California 93940
60. Prof. A. L. Schoenstadt 1  
 Code 53Zh  
 Naval Postgraduate School  
 Monterey, California 93940
61. Dr. Fred Shuman, Director 1  
 National Meteorological Center  
 World Weather Building  
 Washington, D. C. 20233
62. Dr. Joanne Simpson 1  
 Department of Environmental Sciences  
 2015 Ivy Road  
 Charlottesville, Virginia 22903
63. Dr. J. Smagorinsky, Director 1  
 Geophysical Fluid Dynamics Laboratory  
 Princeton University  
 Princeton, New Jersey 08540
64. Dr. R. Somerville 1  
 National Center for Atmospheric Research  
 P. O. Box 3000  
 Boulder, Colorado 80303
65. Dr. Chung-yi Tseng 1  
 Atmospheric Physics Div.  
 Institute of Physics, Academia Sinica  
 Nankang, Taipei 115  
 Taiwan, Republic of China
66. Dr. J. Wallace 1  
 Department of Atmospheric Sciences  
 University of Washington  
 Seattle, Washington 98105
67. Dr. D. Williamson 1  
 National Center for Atmospheric Research  
 P. O. Box 3000  
 Boulder, Colorado 80303

68. Dr. M. G. Wurtele  
Department of Meteorology  
University of California  
Los Angeles, California 90024

1

69. Dr. J. Young  
Department of Meteorology  
University of Wisconsin  
Madison, Wisconsin 53706

1